



**A University of Sussex PhD thesis**

Available online via Sussex Research Online:

<http://sro.sussex.ac.uk/>

This thesis is protected by copyright which belongs to the author.

This thesis cannot be reproduced or quoted extensively from without first obtaining permission in writing from the Author

The content must not be changed in any way or sold commercially in any format or medium without the formal permission of the Author

When referring to this work, full bibliographic details including the author, title, awarding institution and date of the thesis must be given

Please visit Sussex Research Online for more information and further details



# **Single ion coupled to a high-finesse optical fibre cavity for cQED in the strong coupling regime**

**Ezra M. B. Kassa**

Submitted for the degree of Doctor of Philosophy  
University of Sussex  
September 2016

# Declaration

I hereby declare that this thesis has not been and will not be, submitted in whole or in part to another University for the award of any other degree.

Signature:

Ezra Michael Belayneh Kassa

27th April 2017

## UNIVERSITY OF SUSSEX

EZRA MICHAEL BELAYNEH KASSA, DOCTOR OF PHILOSOPHY

### SINGLE ION COUPLED TO A HIGH-FINESSE OPTICAL FIBRE CAVITY FOR CQED IN THE STRONG COUPLING REGIME

#### SUMMARY

The research undertaken unites two distinct areas of quantum information processing: single ions stored in radio-frequency traps and single photons in optical fibres. Strings of ions are presently the most successful implementation of quantum computing, with elementary quantum algorithm and quantum simulations realised. The principal challenge in the field is to enhance the quantum processing power by scaling up current devices to larger systems. We pursue one of the most promising strategies: distributed quantum computation in which multiple small-scale ion processors are interlinked by exchanging photonic quantum bits via optical fibres. This requires a coherent quantum interface between ions and photons, mapping ionic to photonic quantum states and vice versa. To maximise fidelity and the success rate of the scheme, the interaction of ions and photons must take place in a microscopic optical cavity with high finesse. To this end, single  $^{40}\text{Ca}^+$  were trapped in a radio-frequency ion trap whose trapping electrodes are hollow cylinders. Optical fibres with mirrors machined on the facets are inserted into the electrodes to form a Fabry-Pérot cavity. Because the fibres are shielded by the electrodes the detrimental distortion of the trapping field due to their presence is suppressed and ions can be trapped for several hours.  $^{40}\text{Ca}^+$  has a  $\Lambda$ -type energy level scheme wherein the ion is cooled on the  $4^2P_{1/2} \leftrightarrow 4^2S_{1/2}$  transition and the cavity is tuned to the  $4^2P_{1/2} \leftrightarrow 3^2D_{3/2}$  transition. This thesis reports the successful coupling of single ions to a high finesse optical fibre based cavity, with coupling strength  $g = 2\pi \cdot 4.6$  MHz. The cavity has length  $367 \mu\text{m}$ , finesse of 40,000 and linewidth  $2\kappa = 2\pi \cdot 9.4$  MHz. In this coupling regime, the enhancement of the ion's emission rate through the Purcell effect was observed. Further, anti-correlation was observed in the emission rates between the  $P_{1/2} \leftrightarrow D_{3/2}$  and  $P_{1/2} \leftrightarrow S_{1/2}$  transitions with an effective emission rate suppression of up to 60% in the latter transition. The built system offers greater promises. Once the position in the cavity mode has been optimised we expect to reach the long-sought after strong coupling regime with  $(g, \kappa, \gamma) = 2\pi \cdot (12.2, 4.7, 11.2)$  MHz.

# Acknowledgements

The work presented in this thesis has been carried out over the four year period from September 2012 to September 2016 under the supervision of Dr. Matthias Keller in the ion trap cavity QED and molecular physics (ITCM) group at the University of Sussex. There are many who have contributed to this work in different ways whom I would like to thank for their help, advice and support.

I would first like to thank Matthias for the opportunity to work on this project, his wisdom and guidance during the research. I have carried out the research alongside Hiroki Takahashi. Hiroki and I spent countless nights building the experiment. Assembling the trap to its current form was a gruelling surgical task that has undergone many iterations of development. We opened the vacuum chamber for diagnostics, improvement works and implosions(!) 15 times! We have build the experiment from the ground up and it would not have been possible without Hiroki. In the process, I have learned so much from him. Thanks for your devotion, wisdom, patience and friendship. Remember “we are labourers?” Or do you prefer “Kore kara minna de, Metchétcho! Sawagou, sawagou?” It’s fair to say that most if not all our data came after midnight. Thanks for sticking through all those times.

I acknowledge funding from EPSRC.

I thank my predecessor Andrew Riley-Watson who designed the first version of this trap that we have built upon. Nic Seymour-Smith who built the reference laser and the scanning cavity lock. Hiroki, for the code used in the analyses.

I thank Jack Morphew who took the lead on the fibre-shooting experiment and for sharing a great many laughs throughout our PhDs but especially during the arduous writing period at the end. Reggae Shark!

To all my ITCM colleagues, old and new, thanks for your input in the labs and in our group meetings. A special thanks to Markus who also worked in the cavity lab for all the laughter and generally being an awesome colleague. Your presence has made lab life more fun than it should be. I won’t forget the time you walked in the lab singing “I whip my hair back and front, I whip my hair front...”

The help of our technicians Alan Butler and Dan Bartlett has been invaluable.

Thanks to our summer project students. Camilla Compton for spending summer 2015 with us working on resonators for rf and telling us to scrap our original idea. Tom Walker for setting up the new 850 and 854 lasers. Qiming Wu for the work on control of the ion's axial position using rf voltages.

I wish to thank my former professors Fay Dowker and Terry Rudolph for the inspiration, motivation and encouragement to take up this research. Danny Segal, for his unreserved time and guidance.

Thanks to Pedro Nevado Serrano and Graeme Pleasance who formerly shared offices with ITCM for the light-hearted lunch-time discussions over the years.

Thanks to Costas Marios Christoforou who has joined the team to carry on with the experiment.

Outside of the labs, I've been an avid climber and this has done wonders in clearing my mind and generally balancing lab work. So the first thanks goes to Costas (Dino) Klatsias for introducing me to bouldering and climbing at the beginning of my PhD. To my climbing buddies and to my good friends in general, there's nothing better than your company.

Λ Ληφθ

# Contents

<b>1</b>	<b>Introduction</b>	<b>1</b>
<b>2</b>	<b><math>^{40}\text{Ca}^+</math> ions and ion-cavity interaction</b>	<b>5</b>
2.1	The $^{40}\text{Ca}^+$ ion . . . . .	5
2.2	Ion-cavity interaction . . . . .	7
2.2.1	Two-level atom . . . . .	7
2.2.2	Coupling regimes . . . . .	10
2.2.3	Purcell Effect . . . . .	12
2.3	$\Lambda$ -system . . . . .	12
2.4	Eight-level atom . . . . .	14
<b>3</b>	<b>The fibre based Fabry-Pérot cavity</b>	<b>20</b>
3.1	The fibres . . . . .	20
3.2	The cavity . . . . .	23
<b>4</b>	<b>The Paul trap</b>	<b>28</b>
4.1	The trapping potential and the equations of motion . . . . .	28
4.1.1	The trapping potential . . . . .	28
4.1.2	Equation of motion . . . . .	31
4.2	The fibre trap design . . . . .	31
4.3	Trap depth, pseudopotential and secular frequencies . . . . .	33
4.4	Pseudopotential minimum vs side rf voltage . . . . .	35
<b>5</b>	<b>Cavity-trap integration</b>	<b>40</b>
5.1	Electrode assembly design . . . . .	40
5.2	Concentricities and recesses . . . . .	41
<b>6</b>	<b>Ion trap and system assembly</b>	<b>47</b>
6.1	The cage and blocks . . . . .	47
6.1.1	Cavity alignment . . . . .	51
6.2	Vacuum system . . . . .	52
6.2.1	Baking and pressure . . . . .	53
6.3	Resonator and drive . . . . .	53
6.4	Magnetic field compensation coils . . . . .	54
<b>7</b>	<b>Laser system, optics and fibre cavity locking</b>	<b>56</b>
7.1	Lasers . . . . .	56
7.2	Imaging optics . . . . .	58
7.3	PMTs . . . . .	59
7.4	Laser frequency stabilisation . . . . .	59
7.5	Locking of the fibre cavity . . . . .	60
7.5.1	System response function . . . . .	62

7.5.2	Quality of lock . . . . .	64
<b>8</b>	<b>Trapped ions</b>	<b>65</b>
8.1	Trapping ions . . . . .	65
8.2	Excess Micromotion Compensation . . . . .	65
8.2.1	Corrected equations of motion . . . . .	66
8.2.2	Coarse detection and compensation of excess micromotion . . . . .	67
8.2.3	Fine detection and compensation of excess micromotion . . . . .	68
8.2.4	Phase difference treatment . . . . .	74
8.3	Stray magnetic field compensation . . . . .	76
<b>9</b>	<b>Ion-cavity coupling</b>	<b>80</b>
9.1	Radial coupling optimisation method . . . . .	80
9.2	Radial coupling optimisation . . . . .	84
9.3	Purcell Effect - decay rates and suppression of fluorescence . . . . .	86
<b>10</b>	<b>Conclusion and Outlook</b>	<b>93</b>
<b>A</b>	<b>Calcium 40 ions</b>	<b>97</b>
A.1	First ionisation of Calcium 40 . . . . .	97
A.2	$^{40}\text{Ca}^+$ Transitions . . . . .	98
<b>B</b>	<b>Solving the Mathieu Equation</b>	<b>100</b>
B.1	General solutions . . . . .	100
B.2	Stable solutions . . . . .	105
B.3	Equation of motion . . . . .	106
<b>C</b>	<b>The electrode assembly and its integration with a fibre cavity</b>	<b>109</b>
C.1	The electrode-assembly making method . . . . .	109
C.2	Insertion setup . . . . .	110
C.3	Brief account of previous designs . . . . .	114
<b>D</b>	<b>Biquad filters</b>	<b>116</b>
	<b>Bibliography</b>	<b>118</b>

# Chapter 1

## Introduction

This thesis presents work carried out toward the realisation of a node for a quantum network. The fields of Quantum Information and Quantum Computing have been advancing fast. The quantum phenomena leading to the birth of quantum information science are *superposition* and *entanglement*. A well known example exploring the hard-to-conceive quantum superposition principle is that of Schrödinger's cat who is in a superposition state of dead and alive. Entanglement is when the states of two or more particles (irrespective of their spatial separation) cannot be described independently. The measurement of one particle's state will instantaneously affect the state of the others. This phenomenon was widely debated amongst physicists with many arguing that there is an underlying deterministic structure (known as the hidden variables model) which can explain what appears to be "spooky action at a distance" in the statistical features of quantum mechanics. In 1972, however, the Bell measurements [1] settled the dispute by providing strong evidence against the local hidden variable theories. The Bell measurements have sparked great interest in the research area and have opened up promising avenues unparalleled in the classical world. Quantum key distribution (QKD), Quantum Cryptography (QC) and Shor's factorisation algorithms are good examples. QKD protocols harness the aforementioned superposition principle and the no-cloning theorem to allow remote users to generate a fully secure one-time-pad. In QC, using entanglement, one can teleport sensitive information thereby eliminating concerns of the message being intercepted by eavesdroppers. Shor's algorithm [2] is a factorisation protocol that puts at risk current public key cryptography techniques (implemented vastly in the encryption of passwords). The safety net for those using public key cryptography rests on the immense difficulty of the physical implementation of such factorisation algorithm.

All three examples above, QKD, teleportation and Shor's algorithm, have been realised

experimentally [3–5] as proof of principle on small scales. To date, the largest number factorised into primes using Shor’s algorithm is 21 [6]. Using other protocols, the number 143 has also been factorised into primes [7]. Here, the system uses only 4 qubits (-the qubit being the quantum counterpart of the classical bit). The physical expansion to systems using more qubits has been a technologically demanding task.

Examples of qubits used for implementing quantum computing include photons, neutral atoms, ions, superconducting qubits and the nuclear magnetic resonance system used in the aforementioned Shor’s factoring algorithm example. The polarisation of photons can be mapped onto qubit states. Likewise, the quantised energy level of atoms and ions can serve as qubit states. Whilst all exhibit quantum properties for use as qubits, they do not all meet the Divincenzo criteria [8] for constructing a scalable quantum computer. For instance photons make good flying qubits for transmitting information; however it is difficult to engineer interactions between photons. On the other hand, atomic species make excellent stationary qubits as they can be localised in atom traps. Whilst atoms can be trapped in magneto-optical traps for durations of few seconds, the invention of the quadrupole ion trap [9] has allowed the trapping of ions for days and has revolutionised the precise control and spectroscopy of ions. High fidelity readout, long coherence times, easy initialisation and control became accessible [10]. A qubit state preparation and readout fidelity of 99.93% as well as a coherence time of 50 seconds has been achieved [11]. Recently, a two-qubit gate fidelity exceeding the 99% minimum threshold, necessary for fault tolerant quantum computing [12], has been demonstrated with a calcium ion [13]. The work reported in this thesis uses an isotope of one such ion. Chapter 2.1 outlines its benefits as a quantum bit.

The trapping of ions is done by dynamic electric fields. Ions can be localised to 10 nm, a fraction of the optical wavelength used to interact with the ions. The states of trapped ions, as well as trapped atoms, suffer from decoherence due to the interaction of the systems with the environment. Among sources of decoherence, collisions with background gases can be suppressed by using sufficiently low pressures in the traps and the contributions from spontaneous emissions can be alleviated by using metastable states. However, in contrast to atoms in atom traps, trapped ions can be coupled to one another through their collective quantised motion to perform quantum gates. With this, decoherence becomes a negligible effect in the realisation of a quantum processor [14]. The coupling of the motion of ions due to the Coulomb repulsion is much stronger than any other interaction for typical separations of trapped ions. Damping of the motion of the ions is very slow resulting

in very long decoherence times during which many operations can be performed. Many trapped ions can be aligned in a desirable array and interacted-with on an individual, pairwise or subset basis. A good example is a linear Paul trap where a linear chain of ions can be trapped. For a demonstrative quantum computer, in the excess of  $10^5$  qubits are needed [15, 16]. Even so, it has not been possible to trap and entangle more than 14 qubits in an ion trap [17]. In addition to the technical difficulties of trapping long strings of ions under the same trapping potential (which come with an increased number of motional modes that need to be controlled), fundamentally, when qubits are encoded in noise-sensitive subspaces, entangling more qubits becomes difficult as decoherence can scale quadratically with the number of ions[18, 19] as opposed to the classically expected linear relationship.

To solve the scalability dilemma, distributed quantum computing has been proposed [20]. This scheme entails the networking of small scale quantum systems to produce one effective large system. One proposed avenue is the shuttling of ions between different trapping zones of an architecture of interconnected ion traps [21]. To this end, ions have been transferred between traps[22], ion pairs have been split with low loss of coherence [22] and ions have moved around corners [23]. The improvements on scaling-up of this method are however limited by the difficulty of engineering very large number of tightly confined and individually controlled stable laser beams. A more promising scheme is the use of cavity quantum electrodynamics (cQED) with trapped ions. By placing a trapped ion in an optical resonator the result is a hybrid system of stationary and flying qubits. The ions, as stationary qubits, are used for gate operations whilst the flying photonic qubits of the cavity are used for state transfer to other cQED-iontrap systems. By linking up multiple of these cQED-iontrap systems a large quantum network can be formed. cQED-iontrap systems have been used for the generation of single photons [24]. But two nodes of a cQED-iontrap system have yet to be interlinked. The efficiency of a quantum network can be greatly enhanced by working in the so called *strong coupling regime*[20] even though there are other proposals for scalable networks (e.g. [25] proposes a scheme using atomic ensembles without a cavity; [26, 27] propose a scheme with a large number of atoms *weakly* coupled to a cavity but have been strongly contested in [28] and the references therein). The strong coupling regime is one where the dissipative losses (atomic and cavity decay) are smaller than the coupling strength (or interaction rate) between the trapped ions and the cavity. Chapter 2.2 discusses the ion-cavity interaction and the different coupling regimes.

The ion-cavity coupling strength is inversely proportional to the square root of the cavity mode volume. As such, small cavities are sought. This led to the development of fibre-based Fabry-Pérot cavities (FFPC) [29] to produce cavities with mode volumes orders of magnitude smaller than that of conventional cavities. FFPCs are formed from a pair of fibres whose facets have been laser machined and coated with state-of-the-art ultra-low loss dielectric mirror coatings to form a high finesse cavity. Such fibre cavities are produced in our lab [30] and used in the experiment reported herein. They are characterised in Chapter 3.

FFPCs have been used to demonstrate strong coupling with neutral atoms [31]. Ions arguably being superior qubit candidates over neutral atoms, decade-long efforts have gone into achieving the strong coupling regime between an ion and an optical cavity [24, 32–39]. Despite these, strong coupling between a single ion and an optical cavity remains elusive. The principal challenge in this task is the integration of ion traps with optical cavities. When the optical cavities are placed far from the trapping electric field, the integration is relatively straightforward. However, as one brings the cavity mirror closer to the ion (in an effort to reduce the cavity mode volume) the trapping capabilities degrade dramatically. This is because dielectric surfaces become charged in the presence of light fields resulting in the distortion of the trapping electric fields [40]. To lessen this drawback, new trap designs have taken to shielding the FFPCs from the trapping electric field by inserting them in a protective tube. With this ions have been successfully trapped and coupled to an FFPC [38, 39]. Nevertheless, the cavity loss dominated the dynamics of these systems; ions have had yet to be coupled to a high finesse cavity capable of reaching the strong coupling limit. In our laboratory a novel trap has been designed for the integration of fibres and tested [41]. The trap has been further customised for the integration of FFPCs and I report the trap design in Chapter 4 and its integration with a fibre cavity in Chapter 5.

Good mechanical stability is an utmost necessity in cQED systems as the cavity length needs to be stabilised to sub pico-meter accuracies. For this an ion trap design with good stability has been designed and built. The apparatus is described in Chapter 6. The lasers, optical and electrical systems used for interacting with the ion and the cavity are described in Chapter 7. Single ions have been trapped for up to 8 hours in this system and the results are discussed in Chapters 8 and 9.

## Chapter 2

# $^{40}\text{Ca}^+$ ions and ion-cavity interaction

At the heart of the research carried out is the  $^{40}\text{Ca}^+$  ion and its interaction with an optical cavity. I discuss here the calcium ion and its benefits as a quantum bit. The ion-cavity interaction is discussed and the strong coupling regime defined. The master equation for the time evolution of the ion-cavity interaction used for numerical simulations is described.

### 2.1 The $^{40}\text{Ca}^+$ ion

The  $^{40}\text{Ca}^+$  ion is widely regarded as an excellent qubit for quantum information processing. To name a few examples of its success: the continuous generation of on-demand single photons has been demonstrated [24]; ions have been entangled with fidelities beyond the fault tolerance limit [42] required by some models of fault-tolerant quantum computation [43]; GHZ states with up to 14 qubits have been created [17]; the heralded entanglement of two ions in an optical cavity has been demonstrated [44]; a string of up to 5 ions has been optimally coupled to a high-finesse cavity [45].

The relevant electronic configuration of  $^{40}\text{Ca}^+$  is illustrated in Figure 2.1 and the relevant literature regarding the transitions is produced in Appendix A. The conventional spectroscopic notation,  $n^{2S+1}L_J$ , is used where  $n$  is the principal quantum number,  $S$  is the spin quantum number,  $L$  is the spectral notation for the orbital angular momentum and  $J$  is the total angular momentum quantum number. The optical wavelengths and decay rates for each transitions are also shown. One of the advantages of this ionic species is the availability of commercial diode lasers addressing all the optical transitions shown. The ion's ground state is  $4^2\text{S}_{1/2}$ . The P states are short lived states with lifetimes of  $\sim 7$  ns. In contrast, the D states are long-lived states with lifetimes of  $\sim 1$  s. This results in a  $\Lambda$  system whereby the qubit can be realised on the  $\text{S} \leftrightarrow \text{D}$  transitions. The ion can be

laser cooled on the  $S \leftrightarrow P$  transitions and trapped in an ion trap for many hours.  $\text{Ca}^+$  ions also offer a narrow linewidth quadrupole transition at 729 nm used in atomic clock experiments[46] as well as quantum computing [47].

In this experiment, the ion is Doppler-cooled on the  $4^2\text{S}_{1/2} \leftrightarrow 4^2\text{P}_{1/2}$  transition by a *pump* laser with a wavelength of 397 nm. In the cooling process, the ion can decay from the  $4^2\text{P}_{1/2}$  state to the meta-stable  $D_{3/2}$  state. For continuous cooling, we *repump* the ion from the  $D_{3/2}$  states to the  $P$  states using repump lasers. There are two possible schemes for this. One scheme is where an 866 nm beam is used to depopulate the  $3^2\text{D}_{3/2}$  state by exciting the ion to the  $4^2\text{P}_{1/2}$  state. This results in a three-level system where a coherent population trapping can occur in a superposition of  $4^2\text{S}_{1/2}$  and  $3^2\text{D}_{3/2}$  states. In the second recycling scheme, better cooling efficiency can be achieved by decoupling the  $4^2\text{S}_{1/2}$  and  $3^2\text{D}_{3/2}$  states [48]. This is done by employing lasers at 850 nm and 854 nm wavelengths to depopulate the  $3^2\text{D}_{3/2}$  and  $3^2\text{D}_{5/2}$  states respectively.

For studying the ion-cavity dynamics, the cavity is tuned to the  $4^2\text{P}_{1/2} \leftrightarrow 3^2\text{D}_{3/2}$  transition at 866 nm, a wavelength easily accessible for state-of-the-art high-reflective coatings of cavity mirrors.

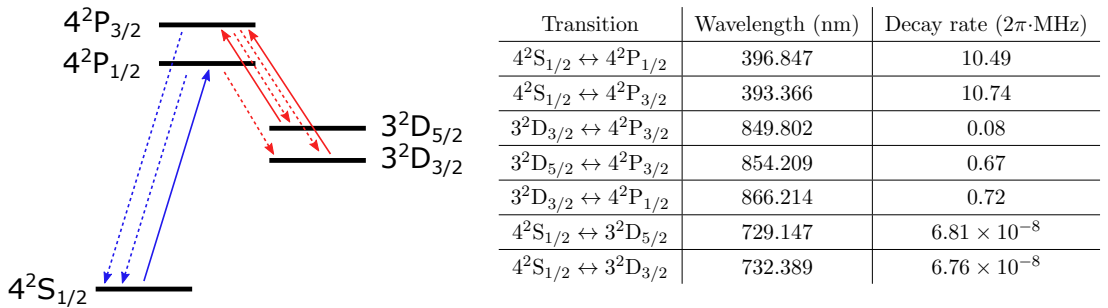


Figure 2.1: The relevant energy level configuration of  $^{40}\text{Ca}^+$  alongside the transition wavelengths (in air) and decay rates (half-linewidths) (see Appendix A for references). In the schematic, a pump laser (blue solid arrow) cools the ion on the  $4^2\text{S}_{1/2}$  to  $4^2\text{P}_{1/2}$  transition. The dotted arrows show the spontaneous decay channels. The red solid arrows indicate repumping lasers used to recycle the ion to the ground state,  $4^2\text{S}_{1/2}$ .

## 2.2 Ion-cavity interaction

To describe the ion-cavity interaction we start from the simplest model of a two-level atom coupled to a single mode of the radiation field. This formalism is then extended to a three-level model in a  $\Lambda$  configuration to imitate the  $S_{1/2} \leftrightarrow P_{1/2} \leftrightarrow D_{3/2}$  transitions in the Calcium ion. To this model, we formally incorporate the losses of the model, namely, spontaneous decay of the atom and field decay of the cavity. We show that the dynamics of this system exhibits two regimes, the weak and strong coupling regimes depending on the atom-cavity interaction rate relative to the dissipative loss rates. We look at these regimes here because this thesis reports the design of a system whose ion-cavity interaction rate can be tuned for a fluid transition between strong and weak coupling regimes. In the derivations below, I am following the treatments in [49] and [50].

### 2.2.1 Two-level atom

We consider a two-level atom with ground state  $|g\rangle$  and excited state  $|e\rangle$  coupled to cavity as illustrated in Figure 2.2. The cavity is represented by an harmonic oscillator with photon number state  $|n\rangle$ . The ion-cavity interaction is described by the interaction Hamiltonian in the rotating wave approximation[51]

$$H_{\text{int}} = \hbar g(r, z)(a\sigma^+ + a^\dagger\sigma^-), \quad (2.1)$$

where  $\hbar$  is the reduced Plank constant,  $a$  ( $a^\dagger$ ) is the photon annihilation (creation) operator,  $\sigma^+$  ( $\sigma^-$ ) is the atomic energy level raising (lowering) operator and  $g(r, z)$  is the ion-position dependent coupling rate between the ion and the cavity with  $r$  and  $z$  being the radial and axial distances from the cavity centre respectively. For the TEM<sub>00</sub> mode of waist  $w(z = 0)$ , the coupling rate is given by

$$g(r, z) = g_0 \frac{w(0)}{w(z)} \sin(kz) e^{-(r/w(z))^2}, \quad (2.2)$$

where  $k$  is the field wave number and  $g_0$  the maximum coupling rate. It is given by

$$g_0 = \sqrt{\frac{\mu_{eg}^2 \omega}{2\hbar\epsilon_0 V}} = \sqrt{\frac{3\lambda^2 c \gamma}{4\pi V}} \quad (2.3)$$

where  $\mu_{eg}$  is the electric dipole matrix element of the state  $|e\rangle$  to state  $|g\rangle$  transition<sup>1</sup>,  $\omega$  and  $\lambda$  are the transition's angular frequency and wavelength respectively,  $\epsilon_0$  is the vacuum permittivity,  $\gamma$  is the spontaneous decay rate (half-linewidth) and  $V$  is the cavity mode

---

<sup>1</sup>For the 866 nm transition in  ${}^{40}\text{Ca}^+$ ,  $\mu_{eg} = 1.6 \times 10^{-29}$  D.

volume given for a symmetric cavity of length  $L$  is given by

$$V = \frac{\pi L w(0)^2}{4}. \quad (2.4)$$

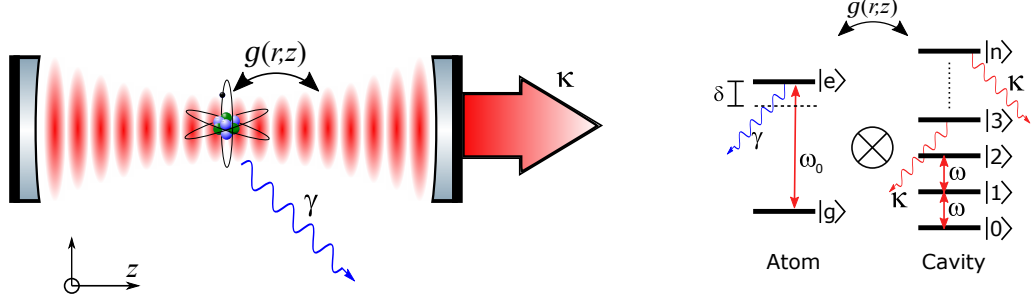


Figure 2.2: Left: Illustration of the atom-cavity dynamics. The atom interacts with the standing wave of the cavity field at rate  $g(r,z)$ . Right: A two-level atom coupled to a cavity modelled as a harmonic oscillator with Fock states  $|n\rangle$  separated by excitations of  $\hbar\omega$ . The atom has ground state  $|g\rangle$  and excited state  $|e\rangle$  separated by energy difference  $E_e - E_g = \hbar\omega_0$ .  $\gamma$  and  $\kappa$  are the respective decay rates (half-linewidths) of the atom and the cavity. The cavity is detuned by  $\delta = \omega - \omega_0$ .

The lossless system is described by the Jaynes-Cummings Hamiltonian

$$H_{\text{JC}} = H_{\text{atom}} + H_{\text{cavity}} + H_{\text{int}}, \quad (2.5)$$

where

$$H_{\text{atom}} = \sum_{i=g,e} E_i \sigma_{ii} \quad (2.6)$$

is the atom's Hamiltonian where  $E_i$  is the energy of level  $i$  and  $\sigma_{ij} = |j\rangle\langle i|$  is a projection operator;

$$H_{\text{cavity}} = \hbar\omega \left( a^\dagger a + \frac{1}{2} \right) \quad (2.7)$$

represents the quantised field in the cavity with frequency  $\omega$ . The eigenstates  $|\pm, n\rangle$  and eigenvalues  $\epsilon_n^\pm$  of the Hamiltonian are given by

$$|+, n\rangle = \cos \theta_n |e, n-1\rangle + \sin \theta_n |g, n\rangle \quad (2.8)$$

$$|-, n\rangle = -\sin \theta_n |e, n-1\rangle + \cos \theta_n |g, n\rangle \quad (2.9)$$

$$\epsilon_n^\pm = \bar{\epsilon}_n \pm \frac{\Delta\epsilon_n}{2} \quad (2.10)$$

where the mixing angle  $\theta_n$  is defined by

$$\tan(2\theta_n) = 2 \frac{g\sqrt{n}}{\delta} \quad (2.11)$$

with  $\delta = \omega - \omega_0$  being the detuning of the cavity and each level consists of a doublet with mean energy  $\bar{\epsilon}$  and splitting  $\Delta\epsilon$  given by

$$\bar{\epsilon}_n = n\hbar\omega \quad (2.12)$$

$$\Delta\epsilon_n = \hbar\sqrt{4ng^2 + \delta^2}. \quad (2.13)$$

The model thus far does not take losses into account. When the dissipative processes are considered the system is described by the master equation [52]:

$$\frac{\partial\rho}{\partial t} = \frac{i}{\hbar}[\rho, H_{JC}] + \mathcal{L}(\rho) \quad (2.14)$$

where  $i$  is the imaginary unit,  $\rho$  is the density matrix and the Liouvillian operator,  $\mathcal{L}$ , describes the dissipative evolution of the system and is given by

$$\mathcal{L}(\rho) = -\frac{1}{2} (\{\rho, C_a^\dagger C_a\} + \{\rho, C_{\sigma^+} C_{\sigma^-}\}) + C_a \rho C_a^\dagger + C_{\sigma^-} \rho C_{\sigma^+} \quad (2.15)$$

where the curly brackets indicate anti-commutators,  $C_a = \sqrt{2\kappa}a$  is the collapse operator for the cavity and  $C_{\sigma^\pm} = \sqrt{2\gamma}\sigma^\pm$  is the collapse operator of the two-level atom. The master equation (2.14) can be re-expressed in terms of an effective Hamiltonian,  $H_{\text{eff}}$ :

$$\frac{\partial\rho}{\partial t} = -\frac{i}{\hbar}(H_{\text{eff}}\rho - \rho H_{\text{eff}}^\dagger) + 2\kappa a \rho a^\dagger + 2\gamma \sigma_- \rho \sigma_+ \quad (2.16)$$

where

$$H_{\text{eff}} = H_{\text{JC}} + H_{\text{loss}} \quad (2.17)$$

and

$$H_{\text{loss}} = -\frac{i\hbar}{2}(2\gamma\sigma_+\sigma_- + 2\kappa a^\dagger a) \quad (2.18)$$

accounts for the dissipative losses.

We consider the unnormalised state<sup>2</sup>

$$|\psi(t)\rangle = A(t)e^{-i\delta/2}|g, 1\rangle + B(t)e^{i\delta/2}|e, 0\rangle \quad (2.19)$$

where  $A(t)$  and  $B(t)$  are the probability amplitudes of the ground and excited states respectively. It follows from the form of (2.16) that the evolution of this state is governed by the effective non-hermitian Schrödinger equation<sup>3</sup>. The resulting equations of motion

---

<sup>2</sup>Eq.(2.19) is an unnormalised quantum state because in contrast to the JCM model, this dissipative model has irreversible loss of excitations via spontaneous decay and cavity emission. Therefore a full wavefunction should include the state  $|g, 0\rangle$ .

<sup>3</sup>The usage of *non-hermitian* and *Schrödinger evolution* may seem contradictory. The approach used is justified in that if all we are interested in is the evolution between the states  $|g, 1\rangle$  and  $|e, 0\rangle$ , then

of the probability amplitudes read

$$\frac{dA}{dt} = -(i\delta - \kappa)A - igB \quad (2.20)$$

$$\frac{dB}{dt} = -\gamma B - igA. \quad (2.21)$$

The general solution of this set of equations takes the form

$$B = B_+ e^{\alpha_+ t} + B_- e^{\alpha_- t} \quad (2.22)$$

where

$$\alpha_{\pm} = \frac{1}{2}(\gamma + \kappa - i\delta) \pm \frac{1}{2}\sqrt{(\gamma + \kappa - i\delta)^2 - 4g^2} \quad (2.23)$$

and the coefficients  $B_{\pm}$  are determined from the initial conditions  $A(0) = 0$  and  $B(0) = 1$ .

More generally, the effective Hamiltonian yields new eigenvalues

$$\epsilon_n^{\pm} = \bar{\epsilon}_n \pm \frac{\Delta\epsilon_n}{2} \quad (2.24)$$

now with

$$\bar{\epsilon}_n = n\hbar\omega - in\hbar\kappa - i\hbar\gamma \quad (2.25)$$

$$\Delta\epsilon_n = \hbar\sqrt{4ng^2 + (\delta - i(\gamma - \kappa))^2}. \quad (2.26)$$

### 2.2.2 Coupling regimes

The coherent coupling rate, given by Equation (2.3), is tunable by the mode volume. In the weak and strong coupling regimes, the dynamics of the atom-cavity interaction evolve differently. To get a physical insight into these regimes, it is sufficient to consider the resonant case,  $\delta = 0$ .

#### Weak coupling

In the limit  $g \ll \kappa, \gamma$ , the dynamics of the system is dominated by dissipation. Integrating the rate equations (2.20) and (2.21) for a time interval  $t \gg \kappa^{-1}$  yields

$$\frac{dB(t)}{dt} = -\left(\gamma + \frac{g^2(\kappa + i\delta)}{\delta^2 + \kappa^2}\right)B(t). \quad (2.27)$$

---

it is sufficient to consider the evolution of the system under the influence of the effective Hamiltonian. Consider the two-level atom in Fig. 2.2. After a similar treatment of the master equation, taking the expectation value of the excited state  $|e\rangle$ , we find there is no contribution from the the Liouvillian operator,  $\mathcal{L}$ . Hence, the state evolves from an initial normalised state  $\alpha|g\rangle + \beta|e\rangle$  to  $\alpha|g\rangle + \beta e^{-\gamma t}|e\rangle$ . The final state is unnormalised but as far as the population of the excited state is concerned, the description is valid. Extending to the three-level model of eq.(2.19), the states  $|e, 0\rangle$  and  $|g, 1\rangle$  can be considered to form an effective upper state (analogous to  $|e\rangle$  in the two-level atom example).

Thus, in the resonant case, the excited state population decays exponentially at the rate  $\gamma' = \gamma(1 + 2C)$  where

$$C = \frac{g^2}{2\kappa\gamma} \quad (2.28)$$

is the cooperativity parameter and is used to describe the coupling regime of a cQED system. Further, we can make appreciable distinctions between the cases where  $\kappa$  or  $\gamma$  dominate as loss channels. In the so-called *bad-cavity* limit where the photon loss from the cavity dominates the dynamics of the system, that is  $\kappa \gg \gamma \approx g$ , the eigenvalues (2.24) become [50]

$$\epsilon_n^+ = n\hbar\omega - i\hbar \left[ \kappa \left( 1 + \frac{g^2}{\kappa^2} \right) (n-1) + \gamma \left( 1 + \frac{g^2}{\kappa\gamma} \right) \right], \quad (2.29)$$

$$\epsilon_n^- = n\hbar\omega - i\hbar\kappa \left( 1 - \frac{g^2}{\kappa^2} \right) n. \quad (2.30)$$

The cavity decays at a reduced rate  $\kappa' = \kappa(1 - g^2/\kappa^2)$  whilst the atom decays at an enhanced rate  $\gamma' = \gamma(1 + 2C)$  as seen earlier. The fraction of photons emitted into the cavity is given by [50]

$$\beta = \frac{2C}{2C + 1}. \quad (2.31)$$

If however the dissipation is dominated by the atom's spontaneous emission,  $\gamma \gg \kappa \approx g$ , we are in what is referred to as the *bad-atom* limit. Here, the eigenvalues for the system become

$$\epsilon_n^+ = n\hbar\omega - i\hbar\kappa \left( 1 + \frac{g^2}{\kappa\gamma} \right), \quad (2.32)$$

$$\epsilon_n^- = n\hbar\omega - i\hbar \left[ \kappa \left( 1 - \frac{g^2}{\kappa\gamma} \right) (n-1) + \gamma \left( 1 - \frac{g^2}{\gamma^2} \right) \right]. \quad (2.33)$$

In this scenario, the cavity now decays at an enhanced rate  $\kappa' = \kappa(1 + 2C)$  whilst the atomic decay is reduced to  $\gamma' = \gamma(1 - g^2/\gamma^2)$ .

### Strong coupling

In the strong coupling regime ( $g \gg \gamma, \kappa$ ), the exponent of the excited state population amplitude (2.23) reads

$$\alpha_{\pm} = -\frac{1}{2} (\gamma + \kappa) \pm ig. \quad (2.34)$$

As the amplitude of the imaginary part is much larger than that of the real part, the evolution consists of a slowly damped oscillation. As can be seen from (2.26), the doublets interact coherently at an effective Rabi frequency  $\Omega_n = \Delta\epsilon_n/\hbar = \sqrt{4ng^2 + \delta^2}$ . The time evolution of the state populations in this regime closely resembles the Jaynes-Cummings model (2.12, 2.13) with the incorporation of a slow decay.

### 2.2.3 Purcell Effect

We have seen in the weak coupling regime that the spontaneous emission rate of an atom can change. The enhancements and suppressions of emission rates are named after Edward Purcell who discussed this topics in 1946 [53]. The Purcell effect is closely tied to Fermi's golden rule which states that the spontaneous decay rate of atoms is proportional to the density of final states [54]. That is, by placing an atom in a cavity, we impose boundary conditions which change the dynamics of the atom. The Purcell factor,  $F_P$ , is defined as the ratio of the atomic emission rate in and outside the cavity:

$$F_P = \frac{\gamma'}{\gamma}. \quad (2.35)$$

In the weak coupling regime (2.27), we find (in the resonant case)

$$F_P = 1 + 2C \quad (2.36)$$

where the cooperativity,  $C$ , is given in (2.28). Substituting the expression for  $g$ , (2.3) yields

$$F_P = 1 + \frac{3\lambda^2 c}{4\pi\kappa V} \quad (2.37)$$

$$= 1 + \frac{3\lambda^2 L \mathcal{F}}{4\pi V} \quad (2.38)$$

$$= 1 + \frac{3\lambda^2 \mathcal{F}}{\pi^3 w(0)^2} \quad (2.39)$$

where in (2.38) we have introduced the cavity finesse<sup>4</sup>,  $\mathcal{F} = \pi c/(L\kappa)$  for cavity length  $L$  and in (2.39) we have used the mode volume  $V$  as defined in (2.4) for a symmetric cavity with waist  $w(0)$ . Large cavity finesses and small waist are sought after for large enhancement factors of emission rates.

## 2.3 $\Lambda$ -system

So far, we have been considering the two-level atom model. Here, we adapt that model to the three-level system of  $\text{Ca}^+$ . The line structure of  $\text{Ca}^+$  can be treated as a  $\Lambda$ -system in the presence of a weak magnetic field. The ion-cavity interaction of the  $\Lambda$ -system is depicted in Figure 2.3. Now,  $\gamma = \gamma_{PS} + \gamma_{PD}$  is the total decay rate from the  $4^2P_{1/2}$  state with contribution  $\gamma_{PS}$  from the  $4^2P_{1/2} \leftrightarrow 4^2S_{1/2}$  and contribution  $\gamma_{PD}$  from the  $4^2P_{1/2} \leftrightarrow 3^2D_{3/2}$ .  $\kappa$  remains the decay rate of the field in the cavity.

---

<sup>4</sup>The finesse is a parameter used to describe the calibre of a cavity. It is discussed in Chapter 3.2

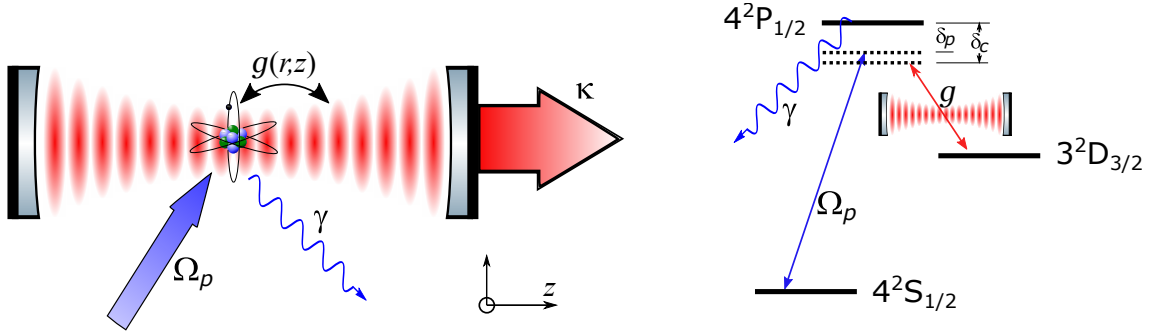


Figure 2.3: Left: Illustration of the ion-cavity dynamics. The ion interacts with the standing wave of the cavity field at rate  $g(r, z)$ . Right: The  $\Lambda$ -system coupled to the cavity. A pump laser with Rabi frequency  $\Omega_p$  and detuning  $\delta_p$  addresses the  $4^2S_{1/2} \leftrightarrow 4^2P_{1/2}$  transition. The cavity is coupled to the  $3^2D_{3/2} \leftrightarrow 4^2P_{1/2}$  transition with detuning  $\delta_c$ .

We couple the cavity to the  $3^2D_{3/2} \leftrightarrow 4^2P_{1/2}$  transition of the  $\Lambda$ -system. A pump beam excites the ion to the  $4^2P_{1/2}$  state. We use Dirac's notation to define  $|S\rangle$  as the  $4^2S_{1/2}$  state,  $|P\rangle$  as the  $4^2P_{1/2}$  state and  $|D\rangle$  as the  $4^2P_{3/2}$  state.

To the two-level Jaynes-Cummings Hamiltonian (2.5), the new Hamiltonian adds an energy contribution for the additional level and an ion-pump interaction term. The lossless Hamiltonian becomes

$$H_{JC} = H_{\text{ion}} + H_{\text{pump}} + H_{\text{cavity}} + H_{\text{int}} \quad (2.40)$$

where

$$H_{\text{ion}} = \sum_{i=S,P,D} E_i |i\rangle \langle i| \quad (2.41)$$

is the ion's Hamiltonian where  $E_i$  is the energy of level  $i$ ;

$$H_{\text{pump}} = \frac{\hbar\Omega_p}{2} (e^{-i\omega_p t} |P\rangle \langle S| + e^{i\omega_p t} |S\rangle \langle P|) \quad (2.42)$$

gives the interaction between the ion and the pump laser when the latter is treated as a classical field with angular frequency  $\omega_p$  and the Rabi frequency is  $\Omega_p$ ;  $H_c$  and  $H_{\text{int}}$  remain unaltered. (Note the notation change in  $H_{\text{int}}$  of the  $4^2P_{1/2} \leftrightarrow 3^2D_{3/2}$  transition decay rate.)

As before, when dissipative processes are taken into account, the evolution of the system is described by a master equation of the form of (2.14).

To the Liouvillian of two-level atom (2.15), we must now add the new loss channel,  $\gamma_{PS}$ . The Liouvillian becomes

$$\mathcal{L}(\rho) = -\frac{1}{2} \left( \{\rho, C_a^\dagger C_a\} + \sum_{j=S,D} \{\rho, C_j \sigma^+ C_{j\sigma^-}\} \right) + C_a \rho C_a^\dagger + \sum_{j=S,D} C_{j\sigma^-} \rho C_{j\sigma^+} \quad (2.43)$$

where  $C_a = \sqrt{\kappa}a$  and

$$C_{j\sigma^\pm} = (\gamma_{Pj}\sigma^\pm)^{\frac{1}{2}}$$

In the interaction picture, and using the  $|P\rangle$  state as the energy reference, the Hamiltonian transforms to [55]

$$H_{JC} \rightarrow H'_{JC} = \hbar \left[ \delta_p \sigma_{SS} + \delta_c \sigma_{DD} + (\delta_c - \delta_p) a^\dagger a + \frac{\Omega_p}{2} (\sigma_{PS} + \sigma_{SP}) + g(\sigma_{PDA} + \sigma_{DPA}^\dagger) \right] \quad (2.44)$$

where we have taken the detuning,  $\delta_p$ , of the pump laser and the detuning,  $\delta_c$ , of the cavity (see Figure 2.3) into account;  $\sigma_{mn} = |m\rangle\langle n|$  is a projection operator. Substituting this Hamiltonian into the master equation (2.14) we can numerically solve the time evolution of the three-level system.

## 2.4 Eight-level atom

The Zeeman structure of the ion, neglected in the three-level model, is now introduced. The effective Rabi frequency depends on the polarisation of the pump beam in the ionic frame. Likewise, when the cavity is resonant or near-resonant, the measured coherent coupling rate,  $g$ , will be reduced by a factor of the Clebsch-Gordan coefficients of the concerned transitions in the Zeeman manifold.

We choose the ion's quantisation axis to be parallel to the cavity axis by applying a magnetic ( $B$ ) field in the  $z$  direction. This lifts the degeneracy of the sub-levels in the Zeeman manifold and alters the three-level system to an eight-level system as shown in Figure 2.4. The energy splitting of the Zeeman sublevel  $m_J$  is given by

$$\Delta E_{J,m_J} = m_J g_J \mu_B B \quad (2.45)$$

where  $\mu_B$  is the Bohr magneton and

$$g_J = 1 + \frac{J(J+1) - L(L+1) + S(S+1)}{2J(J+1)} \quad (2.46)$$

is the Landé g-factor and reads  $g_S := g(^2S_{1/2}) = 2$ ,  $g_P := g(^2P_{1/2}) = 2/3$  and  $g_D := g(^2D_{3/2}) = 4/5$ .

### **Ion Hamiltonian**

The energy levels split to

$$|S\rangle \rightarrow |S, m_S\rangle, \quad m_S \in \{\pm 1/2\} \quad (2.47)$$

$$|P\rangle \rightarrow |P, m_P\rangle, \quad m_P \in \{\pm 1/2\} \quad (2.48)$$

$$|D\rangle \rightarrow |D, m_D\rangle, \quad m_D \in \{\pm 1/2, \pm 3/2\}. \quad (2.49)$$

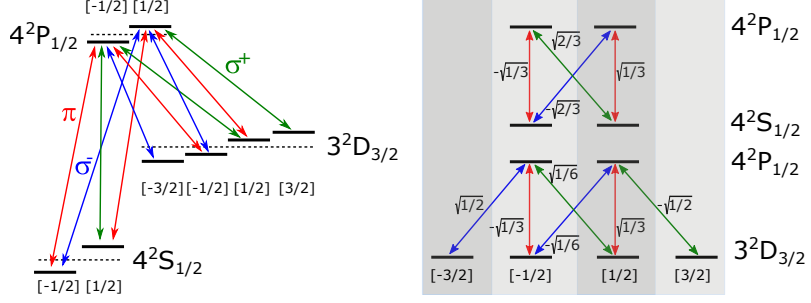


Figure 2.4: Eight-level system. The Zeeman sub levels are shown with their  $m_J$  quantum number in square brackets.  $\pi, \sigma^+$  and  $\sigma^-$  transitions are shown in red, blue and green arrows respectively. Left: Illustration of the energy splitting. Right: The Clebsch-Gordan coefficients for the dipole allowed transition in the Zeeman manifold.

As such, the ion's Hamiltonian in the interaction picture decomposes to

$$H'_{\text{ion}} = H_{\text{ion},S} + H_{\text{ion},P} + H_{\text{ion},D} \quad (2.50)$$

where

$$H_{\text{ion},S} = \sum_{m_S} (\hbar \delta_p + m_S g_S \mu_B) \sigma_{S m_S, S m_S} \quad (2.51)$$

$$H_{\text{ion},P} = \sum_{m_P} m_P g_P \mu_B \sigma_{P m_P, P m_P} \quad (2.52)$$

$$H_{\text{ion},D} = \sum_{m_D} (\hbar \delta_c + m_D g_D \mu_B) \sigma_{D m_D, D m_D} \quad (2.53)$$

and where the projection operator  $\sigma_{K,m_L;L,m_L} = |K, m_K\rangle \langle L, m_L|$  has been extended to include the Zeeman sub-levels.

### **Ion-pump interaction**

The ion-pump interaction is altered because different pump polarisations will address the dipole-allowed transitions with different strengths (depending on the dipole moment of the transition). We define polarisation vector  $\vec{\epsilon}_\pm = (\hat{x} \pm i\hat{y})/\sqrt{2}$  and  $\vec{\epsilon}_0 = \hat{z}$  for the circular and linear polarisation respectively and corresponding to the  $\sigma^\pm$  and  $\pi$  transition in Figure 2.4. The ion-pump interaction decomposes to

$$H'_{\text{pump}} = \frac{\hbar}{2} \sum_{m_S} \sum_{m_P} \left( \vec{\epsilon}_p \cdot \mathbf{d}_{S m_S}^{P m_P} \sigma_{P, m_P; S, m_S} + \vec{\epsilon}_p \cdot \mathbf{d}_{P m_P}^{S m_S} \sigma_{S, m_S; P, m_P} \right) \quad (2.54)$$

where  $\vec{\epsilon}_p$  is the pump polarisation and the vector

$$\mathbf{d}_{L m_L}^{K m_K} = \mathcal{C}_{L, m_L}^{K, m_K} \cdot \vec{\epsilon}_+ \quad \text{if } m_K - m_L = 1 \quad (2.55)$$

$$\mathbf{d}_{L m_L}^{K m_K} = \mathcal{C}_{L, m_L}^{K, m_K} \cdot \vec{\epsilon}_0 \quad \text{if } m_K - m_L = 0 \quad (2.56)$$

$$\mathbf{d}_{L m_L}^{K m_K} = \mathcal{C}_{L, m_L}^{K, m_K} \cdot \vec{\epsilon}_- \quad \text{if } m_K - m_L = -1 \quad (2.57)$$

$$\mathbf{d}_{L, m_L}^{K, m_K} = 0 \quad \text{otherwise.} \quad (2.58)$$

$\mathcal{C}_{L,m_L}^{K,m_K}$  is the Clebsch-Gordan coefficient for the  $|K, m_K\rangle \leftrightarrow |L, m_L\rangle$  transition. The coefficients dictate the relative transition probability in the Zeeman manifold and are given in Figure 2.4.

### **Ion-Cavity interaction**

Similarly, the dipole moments of the  $P \leftrightarrow D$  transition in the Zeeman manifold alter the ion-cavity interaction Hamiltonian. The Hamiltonian becomes

$$H'_{\text{int}} = \hbar g \sum_{m_D} \sum_{m_P} \left( \vec{\epsilon}_a \cdot \mathbf{d}_{Dm_D}^{Pm_P} \sigma_{P,m_P;D,m_D} a + \vec{\epsilon}_a \cdot \mathbf{d}_{Pm_P}^{Dm_D} \sigma_{D,m_D;P,m_P} a^\dagger \right) \quad (2.59)$$

$$+ \hbar g \sum_{m_D} \sum_{m_P} \left( \vec{\epsilon}_b \cdot \mathbf{d}_{Dm_D}^{Pm_P} \sigma_{P,m_P;D,m_D} b + \vec{\epsilon}_b \cdot \mathbf{d}_{Pm_P}^{Dm_D} \sigma_{D,m_D;P,m_P} b^\dagger \right) \quad (2.60)$$

where  $\vec{\epsilon}_a$  and  $\vec{\epsilon}_b$  are the orthogonal polarisations of the cavity mode with respective annihilation operators  $a$  and  $b$ . Applying a magnetic field in the  $z$  direction leads the cavity mode being composed of  $\sigma^\pm$  polarisations purely.

### **Dissipation**

The cavity decay rate,  $\kappa$  is independent of the ion dynamics and only depends on the physical properties of the cavity. As such, the cavity's collapse operator remain unaltered.

However the spontaneous emission losses now have to include the Clebsch-Gordan coefficients. In the presence of the B-field, the spontaneous emission rates decompose to account for each dipole-allowed transition in the Zeeman manifold:

$$\gamma_{KL} \rightarrow |\mathcal{C}_{L,m_L}^{K,m_K}| \gamma_{KL} \quad (2.61)$$

Accordingly, the collapse operators become

$$C_{S\sigma}^\pm = \sqrt{2|\mathcal{C}_{S,\pm 1/2}^{P,\mp 1/2}| \gamma_{PS} \sigma_{S,\pm 1/2;P,\mp 1/2}} \quad (2.62)$$

$$C_{S\sigma}^0 = \sum_{m=\pm 1/2} \sqrt{2|\mathcal{C}_{S,m}^{P,m}| \gamma_{PS} \sigma_{S,m;P,m}} \quad (2.63)$$

for the  $\sigma^\pm$  and  $\pi$  transitions, respectively, in the Zeeman manifold of the  $|P\rangle$  and  $|S\rangle$  states, and

$$C_{D\sigma}^\pm = \sum_{m=\pm 1/2} \sqrt{2|\mathcal{C}_{D,m\pm 1}^{P,m}| \gamma_{PD} \sigma_{D,m\pm 1;P,m}} \quad (2.64)$$

$$C_{D\sigma}^0 = \sum_{m=\pm 1/2} \sqrt{2|\mathcal{C}_{D,m}^{P,m}| \gamma_{PD} \sigma_{D,m;P,m}} \quad (2.65)$$

for the  $\sigma^\pm$  and  $\pi$  transitions, respectively, in the Zeeman manifold of the  $|P\rangle$  and  $|D\rangle$  states.

### **Simulation**

To see the Purcell effect, a Matlab Quantum Optics Toolbox [56] was used to simulate the steady state population of the  $4^2P_{1/2}$  state and the cavity emission using the eight-level atom model. Figure 2.5 shows the results. Here, we are in the bad-cavity regime with  $(g, \kappa, \gamma_{PD}) = 2\pi \cdot (0.25, 0.45, 0.06)\gamma_{PS}$ . The cavity is aligned in the  $z$  direction. The pump is vertically polarised, detuned by  $\delta_p = 2\pi \cdot (-11)$  MHz and has Rabi frequency  $\Omega_p = 0.6\gamma_{PS}$ . The degeneracy of the Zeeman sub-levels is lifted by a magnetic field  $B = -1.2$  G in the  $z$  direction. The cavity length is scanned and the emissions of the  $|P\rangle \leftrightarrow |S\rangle$  and  $|P\rangle \leftrightarrow |D\rangle$  transitions simulated. Without any repumping, the population would be trapped in the metastable  $|D\rangle$  manifold. To avoid this, repumping was introduced by modelling it as a direct decay from the  $|D\rangle$  level to the  $|S\rangle$  state. The repumping efficiency was tuned by changing the decay rate in this transition. For low repumping efficiencies, it has been verified that this is a good approximation to the more complete model which would include the  $4^2P_{3/2}$  and  $3^2D_{5/2}$  states when 850 nm and 854 nm lasers are used to repump the ion (see Fig. 2.1). In the experimental scenario where 850 nm and 854 nm lasers repump the ion, there would be a contribution of 393 nm photons to the total number of collected photons in the  $|P\rangle \rightarrow |S\rangle$  transition<sup>5</sup>. As such, the simulation is designed to consider the emission in the  $|D\rangle \rightarrow |S\rangle$  as 393 nm photons. This emission is added to the 397 nm emission to get the total UV fluorescence. The simulated cavity emission rate is the total emission of the cavity when no loss due to imperfections of in the cavity mirrors is taken into account.

As the detuning of the cavity approaches that of the pump beam, the emission of 866 photons ( $|P\rangle \rightarrow |D\rangle$  decay channel) is enhanced by the two-photon Raman process. As expected, the emission rate of 866 nm photons rises with repumping efficiency. The enhancement of the cavity emission is accompanied by a suppression of the effective decay rate of the 397 nm transition,  $|P\rangle \rightarrow |S\rangle$ . Although, small repumping rates lead to small cavity emission rates, the Purcell effect is clearly observed through the fall of the effective decay rate of the pump transition. Suppressions by up to 72% compared to the cavity-less model ( $g = 0$ ) are expected for the given parameters. The relationship between the pumping efficiency and the suppression rate is illustrated in Figure 2.6. The suppression rate falls with larger repumping efficiency as the coherence rate  $g$  between the  $|D\rangle$  and  $|P\rangle$  states is exceeded by the decay rate,  $\gamma_{DS}$ , of the newly introduced decay channel,  $|D\rangle \rightarrow |S\rangle$ . It is not a surprise, therefore that maximum suppression seen in the  $|P\rangle \rightarrow |S\rangle$  decay occurs in the limit of no repumping.

---

<sup>5</sup>Given that we do not spectrally separate the 393 nm and 397 nm photons in the detection optics

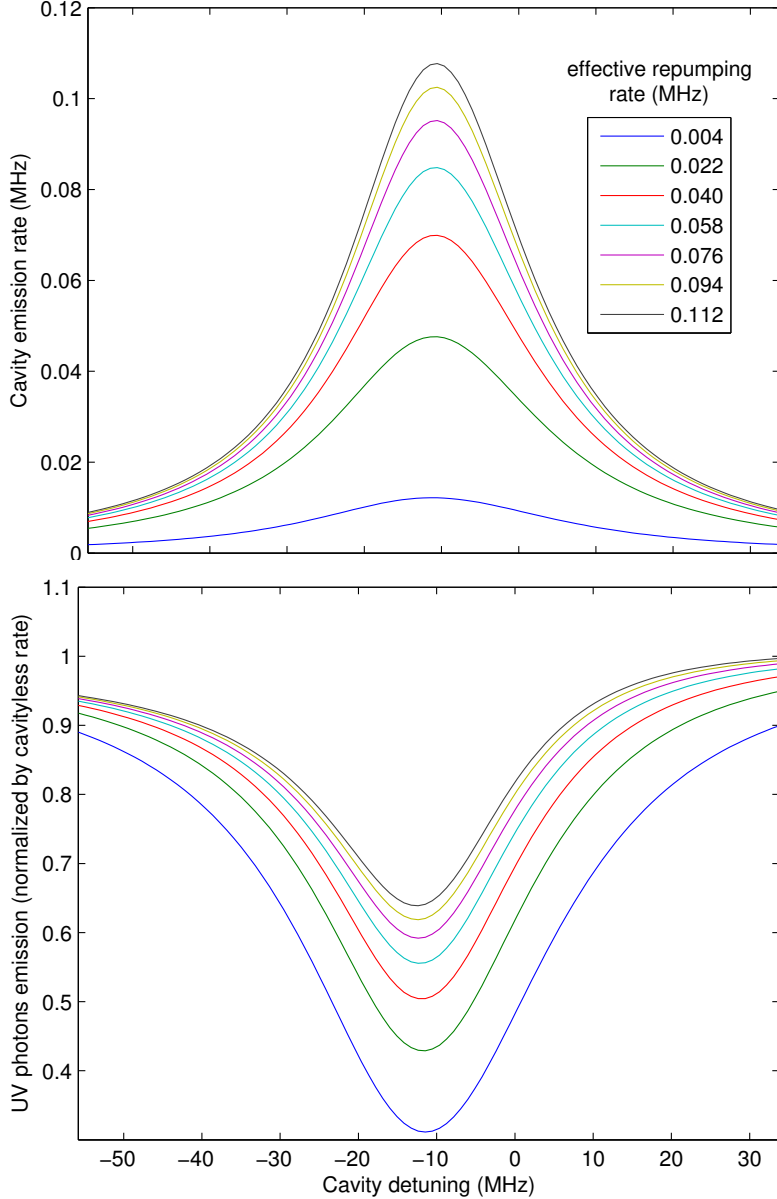


Figure 2.5: Emission rates as the cavity length is scanned over the Raman resonance for varying repumping efficiencies. Top: The emission rate of 866 nm photons of the  $|P\rangle \leftrightarrow |D\rangle$  transition. Bottom: The emission rate of 397 nm and 393 nm photons of the  $|P\rangle \rightarrow |S\rangle$  transitions. The resonance is shifted by -11 MHz because the Raman resonance occurs when the cavity detuning matches  $\delta_p$ .

In summary, a two-level atom model showed that in the strong coupling regime, coherence of the atom-cavity dynamics is retained for an appreciable period making the model resemble that of the ideal Jaynes-Cummings model. This makes the strong coupling regime sought after for quantum computation and quantum networking. In the bad-cavity limit of the weak-coupling regime, we have seen the atomic emission rate can be enhanced

due to the Purcell effect. Alternately, when the atomic decay dominates the system losses, suppression of the emission rates is to be expected. To the two-level atom, an additional level was added to form the  $\Lambda$  system of the calcium ion. The cavity is tuned to the  $4^2P_{1/2} \leftrightarrow 3^2D_{3/2}$  transition. The interaction picture Hamiltonian for this model was presented. An applied B-field lifts the degeneracy of the Zeeman levels resulting in an eight-level atom. Adjustments to the three-level model Hamiltonian are made to incorporate the new levels and produce a master equation which is used to numerically simulate the dynamics of the eight-level system.

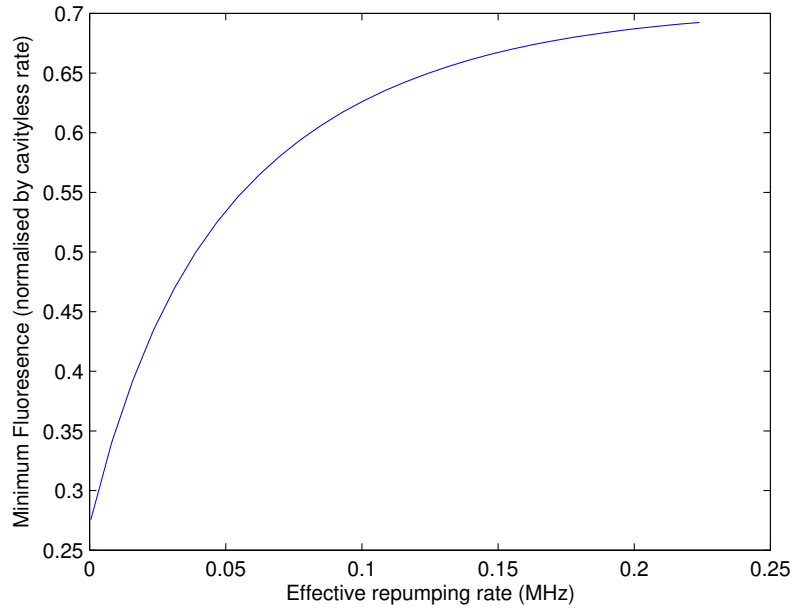


Figure 2.6: UV photons emission rate dependency on the repumping efficiency.

## Chapter 3

# The fibre based Fabry-Pérot cavity

The principal aim of this research is to establish strong coupling between a trapped ion and an optical cavity. As the coupling strength is inversely proportional to the square root of the cavity mode volume, it is in our interest to have the cavity mirrors as close as possible to the ion. The caveat is that trapping capabilities degrade and often perish in the presence of dielectric materials near the trapping region [40]. The trapping field gets distorted by the mirrors. The solution therefore becomes to use small mirrors that can be shielded from the trapping electric field. Mirrors machined on the end facets of optical fibres proved to be ideal candidates [38]. These fibre based Fabry-Pérot cavities (FFPCs) offer the possibility of tight integration with an ion-trap [41, 57–59] with the extra benefit of not requiring additional optics to collect emissions from the ion.

### 3.1 The fibres

The production process of FFPCs employed in our lab is detailed in [30]. The end facet of an optical fibre is ablated with multiple pulses of a CO<sub>2</sub> laser to produce a concave curvature. The high intensity pulses melt and smoothen the fibre facets to produce a surface with extremely low surface roughness [29]. Following this, a Michelson interferometer is used to deduce the radius of curvature of the shot fibre.

The FFPC used in the experiment is formed from a pair of metal coated fibres<sup>1</sup>. Metal coating was chosen for ultra high vacuum (UHV) compatibility. In the interest of consistency with the nomenclature used in the lab database, we refer to the individual FFPC fibres by their assigned names: f112 and f108.

f112 is a single mode fibre and f108 is a multi mode fibre. Images of their facets after

---

<sup>1</sup>IVG Fiber Cu800/200 (single mode), Cu180/198(multimode)

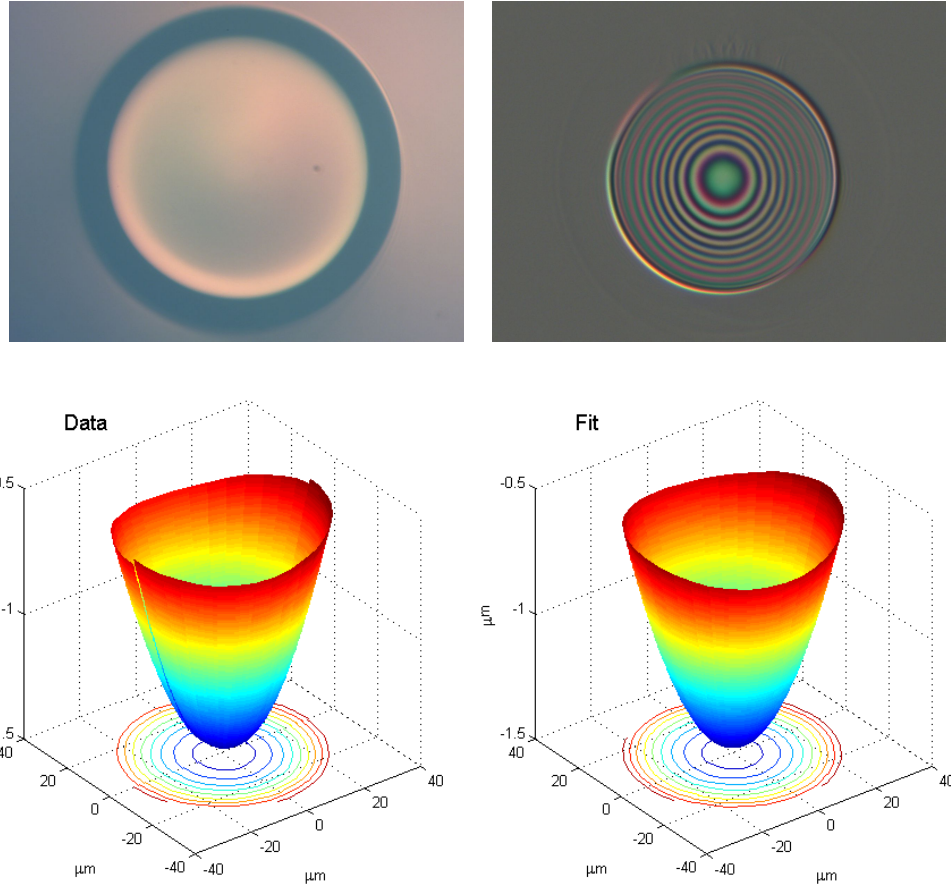


Figure 3.1: Fibre f112 laser machined facet. Top left: Optical image of the fibre facet. The small dark spot is dust on the imaging device. Top right: Interference image of the fibre facet from which the radius of curvature is extracted. Bottom: Data and Gaussian fit of the fibre facet curvature.

the CO<sub>2</sub> laser machining process as well as their reconstructed curvatures are presented in Figures 3.1 and 3.2. After the fibre facet machining process, the fibres are sent for state-of-the-art high reflectivity coating<sup>2</sup> at 866 nm. Detailed fibre specifications are given in Table 3.1. Here, the radii of curvature are obtained from the 3-dimensional Gaussian fits shown in Figures 3.1 and 3.2. The associated errors are systematic errors in obtaining the interference images ; the fitting errors are negligible in comparison.

The f108 facet picture shown in Figure 3.2 is one taken immediately after the laser machining process. Its current facet however has been contaminated. We endeavour to avoid any contact of the fibres' facet with any hard material as this will potentially damage the fibre either by contamination or by damage to the coating layer. Sometimes,

---

<sup>2</sup>Advanced Thin Films, 5733 Central Avenue Boulder, Colorado USA

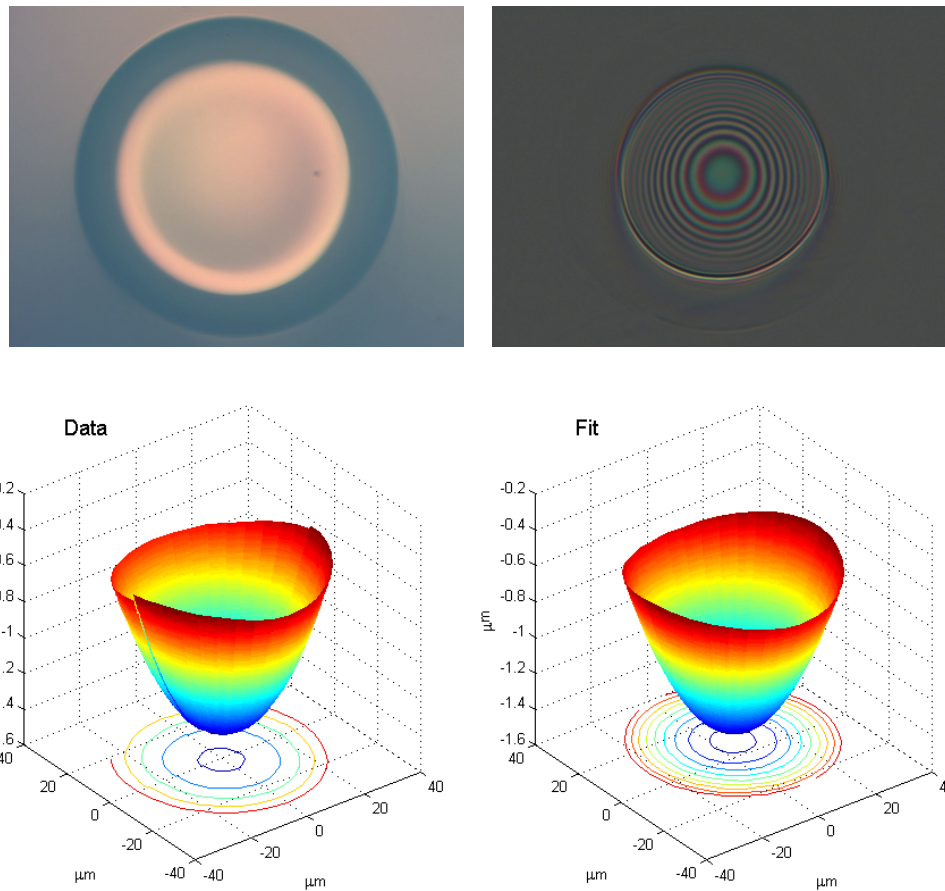


Figure 3.2: Fibre f108 laser machined facet. Top left: Optical image of the fibre facet. The small dark spot is dust on the imaging device. Top right: Interference image of the fibre facet from which the radius of curvature is extracted. Bottom: Data and Gaussian fit of the fibre facet curvature.

delicate handling is not sufficient to ensure this. During the removal of the fibre from its storage, a brief contact between the fibre tip and its mount resulted in the deposition of dust. Despite this, the fibres' performance remains intact as we shall see from the finesse measurements that follow. The acquired dust is outside of the active region (beam spot diameter) forming the cavity. The spot size on the fibres is discussed in the following section.

Table 3.1: Cavity fibres' details

	Fibre	
	f112	f108
Type	Single mode	Multi mode
Model	IVG Cu800/200	IVG Cu180/198
Core diameter ( $\mu\text{m}$ )	$6 \pm 0.5$	$180 \pm 3$
Cladding diameter ( $\mu\text{m}$ )	$200 \pm 2$	$198 \pm 3$
Fibre coating diameter ( $\mu\text{m}$ )	$260 \pm 10$	$240 \pm 10$
Numerical aperture	0.13	0.22
Major axis radius, $R_x$ ( $\mu\text{m}$ )	$581 \pm 10$	$587 \pm 10$
Minor axis radius, $R_y$ ( $\mu\text{m}$ )	$542 \pm 10$	$529 \pm 10$
$\bar{R} = \sqrt{R_x R_y}$ ( $\mu\text{m}$ )	$561 \pm 7$	$557 \pm 7$
Ellipticity, $E = (R_x - R_y)/R_x$	$0.07 \pm 0.02$	$0.10 \pm 0.02$
Transmission <sup>3</sup> at 866 nm (ppm)	$25 \pm 1$	$25 \pm 1$
Loss at 866 nm (ppm)	$62 \pm 1$	$62 \pm 1$

## 3.2 The cavity

To form a cavity, the fibres are mounted with their coated ends facing one another as shown in Figure 3.3a. Note that this is a test set up. A microstage and a calibrated microscope are used to adjust their separation, the cavity length.

The finesse is used to quantify the quality of a cavity. It is given by

$$F = \frac{\pi\sqrt{R}}{1-R} \quad (3.1)$$

where  $R$  is the reflectivity of the mirrors. For large finesses ( $\geq 30$ ),  $F$  takes a form well

---

<sup>3</sup>Coating company's measurement on a reference plate that was coated alongside the fibres. The error is a conservative estimate.

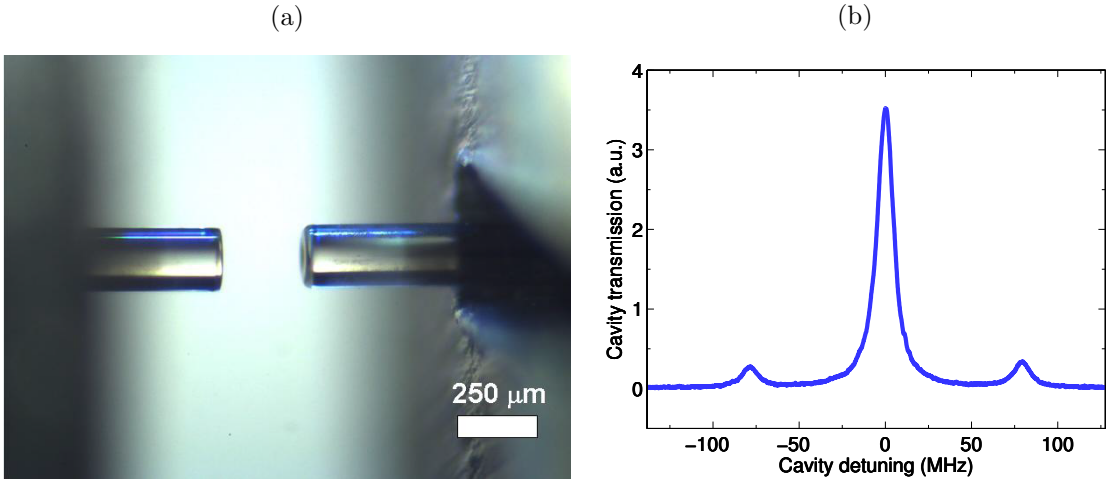


Figure 3.3: (a) Image of two laser machined and coated fibres brought together to form a cavity. (b) A typical transmission signal when a frequency modulated laser is input into the cavity while the cavity length is scanned across the resonance. The separation of the sidebands from the carrier signal corresponds to the modulation frequency. This information is used to calibrate the x-axis from time to frequency domain. The cavity length for this data is approximately 300  $\mu\text{m}$ . Figures produced from [30].

suit for experimental measurements:

$$F = \frac{\text{FSR}}{\delta\nu} = \frac{c}{2l\delta\nu},$$

where FSR is the free spectral range,  $\delta\nu$  is the cavity full width at half maximum in frequency,  $c$  is the speed of light and  $l$  the cavity length.

Once the cavity length has been set, it suffices to find the linewidth,  $\delta\nu$ , to compute the finesse. To find  $\delta\nu$ , we input a frequency-modulated 866 nm beam into one of the fibres and we monitor the transmitted signal from the other fibre. The cavity length is scanned by means of a piezo-electric transducer upon which one of the fibres is mounted. Note that the scan length amplitude is negligible with respect to the cavity length.

At the transmission side, a carrier signal with sidebands at the laser modulation frequency is seen as in Figure 3.3b. The sidebands, separated by two times the modulation frequency, serve as calibration to deduce the linewidth,  $\delta\nu$ .

It is noted that the piezo has a linear response to voltage in a small voltage range. The response is non-linear in general. A triangular wave signal is applied to the piezo to scan the cavity length around a resonance. The finesse for the f112-f108 pair for varying cavity length is illustrated in Figure 3.4. We have fineses in excess of 40,000 at the cavity

lengths of interest to us which are in the range of 300 - 400  $\mu\text{m}$ . The experiment is run at a cavity length of 367  $\mu\text{m}$ . This cavity length was measured in situ with a precision of less than 0.1  $\mu\text{m}$ . The method employed is as follows. We input two lasers into the cavity and look at the transmission peaks whilst scanning the cavity length (as is done in the finesse measurements). One of the lasers is a frequency stabilised 866nm laser which we use as a reference. The second laser is an 894 nm laser whose wavelength we can tune. We tune this laser's wavelength until its transmission peak out of the cavity spectrally overlaps with that of the 866 nm laser. We call this wavelength  $\lambda_1$  and the cavity length can be defined as  $L = 0.5n\lambda_1$  where  $n$  is an integer (giving the number of half-wavelength that can fit into the cavity length). We then increase (or alternatively decrease) the 894 nm laser's wavelength gradually until the new wavelength has a transmission peak which overlaps with the 866 nm peak and call this new wavelength  $\lambda_2$ . For the nearest neighbour wavelength, now,  $n - 1$  (or  $n + 1$ ) half-wavelength of  $\lambda_2$  fit in the cavity. Hence the cavity length is given by

$$L = \frac{\lambda_1\lambda_2}{2(\lambda_2 - \lambda_1)}. \quad (3.2)$$

At this cavity length, the cavity linewidth is  $\nu = 9.4$  MHz. Thus, the (amplitude) decay rate is

$$\kappa = 2\pi \cdot 4.7 \text{ MHz}. \quad (3.3)$$

For high finesse cavities, the cavity finesse (3.1) is also given by

$$F = \frac{2\pi}{T + L}$$

where  $T$  and  $L$  are the cavity transmission and loss respectively.  $T$  is measured off a reference plate that was mirror-coated alongside the fibres. Given the cavity finesse and the fibres' transmission, the loss can be deduced. Both figures are given in Table 3.1. A loss of  $124 \pm 2$  ppm is calculated for the cavity. The high losses come from absorption and scatter by the fibres. As the loss measurements are inferred from cavity finesse results, we cannot accurately state the loss contribution from the individual fibres. In Table 3.1, it was assumed that the loss can be distributed equally between each fibre.

For a cavity with length  $L$  formed from mirrors with radii of curvature  $R_1$  and  $R_2$  the smallest mode waist,  $w_0$ , is defined by

$$w_0^2 = \frac{L\lambda}{\pi} \left( \frac{g_1 g_2 (1 - g_1 g_2)}{(g_1 + g_2 - 2g_1 g_2)^2} \right)^{1/2} \quad (3.4)$$

where  $\lambda$  is the mode field wavelength and  $g_i = 1 - L/R_i$ .

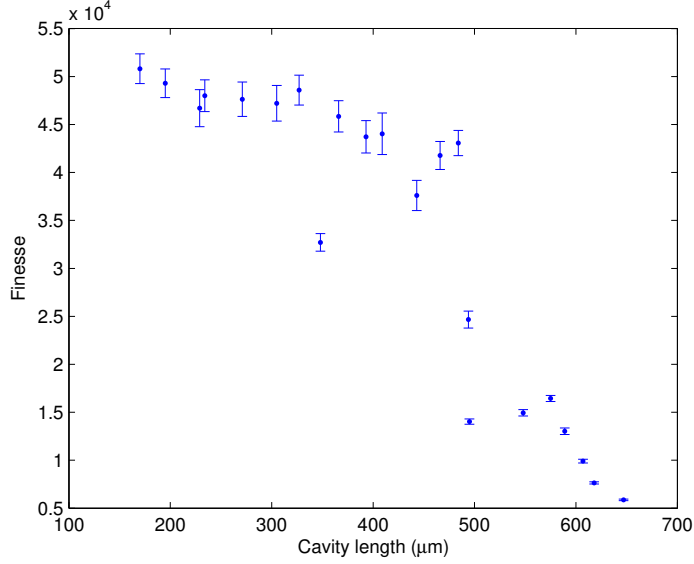


Figure 3.4: Finesse vs cavity length for the f112 and f108 pair inferred from the linewidth of resonant transmission peaks at 866 nm. The error bars are from standard deviations of 20 measurements. See main body for more details.

For a symmetric cavity ( $R_1 = R_2 = R$ ), the cavity mode waist becomes

$$w_0 = \sqrt{\frac{\lambda}{2\pi}} (L(2R - L))^{1/4}. \quad (3.5)$$

From the radii of curvature of the fibres' facets,  $\bar{R}$ , given in Table 3.1 and using a cavity length of 367  $\mu\text{m}$ , we calculate the cavity waist to be  $8.51 \pm 0.05 \mu\text{m}$  for the TEM<sub>00</sub> mode. At the fibres' facet the spot size (radius) is circa 10  $\mu\text{m}$ . The mode volume is given by (2.4).

A key parameter of interest to us is the coupling strength,  $g$ , which has a dependence on the geometrical properties of the cavity. The coupling strength is inversely proportional to  $V$  as given in Equation 2.3.  $g_0$  is plotted as a function of the cavity length in Figure 3.5. We find  $g_0(L = 367\mu\text{m}) = 2\pi \cdot 17.2 \text{ MHz}$ . The merit of this figure is that at this cavity length,  $g$  exceeds both the cavity decay rate,  $\kappa$  (Eq. (3.3)) and the atomic spontaneous emission rates of the  $P$  state (Fig. 2.2) making this cavity suitable for the strong coupling regime.

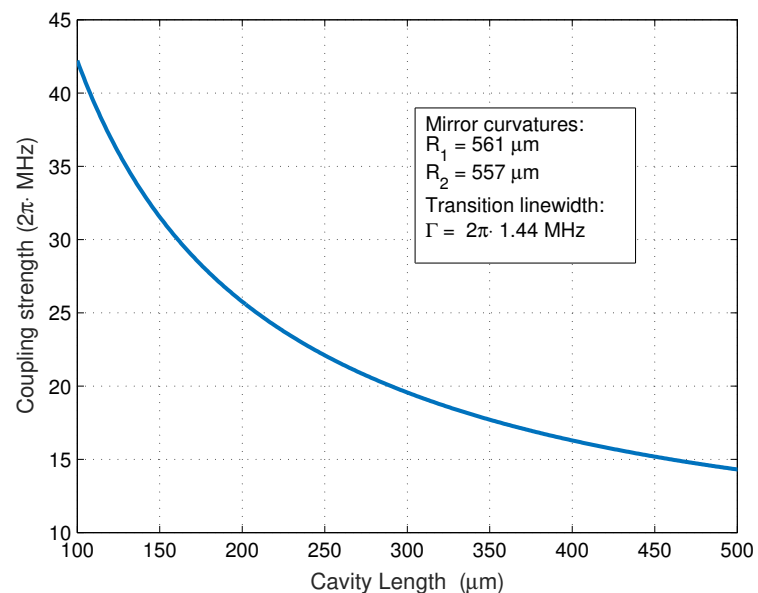


Figure 3.5: Computed maximum coupling strength,  $g_0$ , vs cavity length when the cavity is coupled to the  $P_{1/2} \leftrightarrow D_{3/2}$  transition of a  $^{40}\text{Ca}^+$  ion.

# Chapter 4

## The Paul trap

Having introduced the cavity-related part of the experiment this section is solely intended to introduce the ion trapping part. I start by covering the essentials of ion trapping theory using an ideal Paul trap model. I then introduce the custom design used in the experiment placing emphasis on the trapping region. The trap depths and secular frequencies are computed. Also discussed are surrounding electrodes that play roles in stabilising the trap and in controlling the ion's position.

### 4.1 The trapping potential and the equations of motion

#### 4.1.1 The trapping potential

Earnshaw's Theorem [60] states that it is impossible to confine a charged particle in 3D using electrostatic fields alone. In search for a non-static potential,  $\phi$ , which allows the stable confinement of an ion in a region in space, we need to solve Laplace's equation,  $\nabla^2\phi = 0$  (since  $\nabla \cdot \mathbf{E} = \nabla \cdot (-\nabla\phi)$  and we have from Gauss' law in free space  $\nabla \cdot \mathbf{E} = 0$ ). At the lowest order expansion, the function which obeys Laplace's equation in 3D Cartesian coordinate  $(x, y, z)$  is of the form

$$\phi = k(\alpha x^2 + \beta y^2 + \gamma z^2), \quad (4.1)$$

with constant  $k$  and condition  $\alpha + \beta + \gamma = 0$ .

We note from the condition above that not all coefficients  $\alpha, \beta$  and  $\gamma$  can simultaneously be positive (nor negative). In physical terms, at any given time, there could be a positive confining potential in two of the three dimensions but there must also be an *anti-trapping* potential in the third dimension.

We set  $\alpha = \beta = 1$ . Then,  $\gamma = -2$ . This choice gives a cylindrically symmetric potential:

$$\phi = k(r^2 - 2z^2), \quad (4.2)$$

where  $r^2 = x^2 + y^2$  is the radial distance in the  $xy$  plane from the origin.

Ion traps producing equipotentials of the above equation are made of a pair of hyperboloid endcap electrodes of revolution about the  $z$ -axis and a ring electrode around the  $z$ -axis, also with a hyperbolic cross section [9]. These traps are commonly referred to as Paul traps after Wolfgang Paul who was awarded the Physics Nobel Prize in 1989 for this invention. A schematic of a near-ideal Paul trap is shown in Figure 4.1.

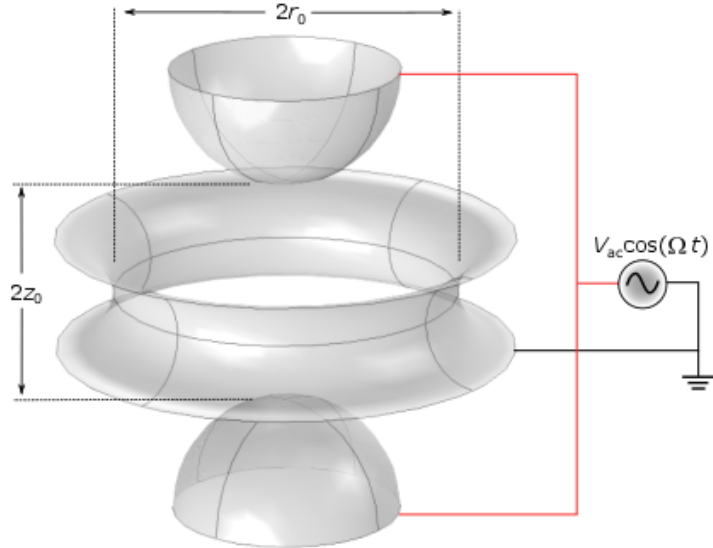


Figure 4.1: A near-ideal Paul ion trap. Rf is applied to the endcaps whilst the ring is held at rf-ground. The ion is trapped at the centre. The endcaps are separated by  $2z_0$  and the ring has radius  $r_0$ .

Paul traps can be operated in different ways. An ac potential can be applied to both the endcap electrodes and the ring electrode but with a phase difference of  $180^\circ$ . Alternatively, the potential  $\phi$  can be applied to the endcap electrodes whilst grounding the ring electrode (or vice-versa). In what follows, we choose to ground the ring electrodes and apply a potential  $\phi_0$  to both endcaps (with no phase difference),

$$\phi_0 = U_{dc} + V_{ac} \cos(\Omega t) \quad (4.3)$$

where  $U_{dc}$  is the DC potential of applied to the endcap electrodes in addition to the radio frequency (rf) voltage with angular frequency  $\Omega$  with peak amplitude  $V_{ac}$ .

When the endcap and ring hyperbolas share the same asymptotes, consideration of the boundary conditions yields

$$\phi_0 = \phi(0, z_0, t) - \phi(r_0, 0, t) \quad (4.4)$$

$$= k(-2z_0^2 - r_0^2). \quad (4.5)$$

Thus, our trapping potential becomes

$$\phi = \frac{-\phi_0}{2z_0^2 + r_0^2}(r^2 - 2z^2) \quad (4.6)$$

The equations of motion of a particle of mass  $m$  and positive charge  $e$  in the Paul trap are

$$m\ddot{r} = eE_r = -e\frac{\partial\phi}{\partial r} \quad (4.7)$$

$$m\ddot{z} = eE_z = -e\frac{\partial\phi}{\partial z}. \quad (4.8)$$

Thus the equation of motion in the radial plane becomes

$$m\ddot{r} = \frac{2e}{r_0^2 + 2z_0^2}(U_{dc} + V_{ac}\cos(\Omega t))r \quad (4.9)$$

The above is in the form of the Mathieu equation

$$\frac{d^2x}{d\tau^2} + (a - 2q\cos(2\tau))x = 0 \quad (4.10)$$

Going into dimensionless units by setting  $\tau = \Omega t/2$ , we have  $dt^2 = 4 d\tau^2/\Omega^2$ . Then,

$$\frac{d^2r}{d\tau^2} + \frac{8e}{m\Omega^2(r_0^2 + 2z_0^2)}(-U_{dc} - V_{ac}\cos(2\tau))r = 0. \quad (4.11)$$

And thus the  $a$  and  $q$  parameters of the Mathieu equation for the radial equation of motion are respectively,

$$a_r = \frac{-8eU_{dc}}{m\Omega^2(r_0^2 + 2z_0^2)}, \quad (4.12)$$

$$q_r = \frac{4eV_{ac}}{m\Omega^2(r_0^2 + 2z_0^2)}. \quad (4.13)$$

Similarly, or by inspection of equation 4.6, we find the  $a$  and  $q$  parameters for the axial equations to be respectively

$$a_z = -2a_r = \frac{16eU_{dc}}{m\Omega^2(r_0^2 + 2z_0^2)}, \quad (4.14)$$

$$q_z = -2q_r = \frac{-8eV_{ac}}{m\Omega^2(r_0^2 + 2z_0^2)}. \quad (4.15)$$

### 4.1.2 Equation of motion

The Mathieu equation (4.10) is solved in Appendix B to find its general solution. Physical limitations are then imposed to extract the stable solutions. The first order solution to the ion's equation of motion for the typical case where  $(|a_i|, |q_i|) \ll 1$  is given by[61]:

$$u_i = u_{1i} \cos(\omega_i t + \psi_{1i}) \left[ 1 + \frac{q_i}{2} \cos(\Omega t) \right], \quad (4.16)$$

with  $i = \{r, z\}$  where we have used the definitions  $u_r = r$  and  $u_z = z$  and where

$$\omega_i = \frac{1}{2}\Omega \sqrt{a_i + \frac{1}{2}q_i^2} \quad (4.17)$$

gives the ion's secular frequencies.

The first term in the expansion of (4.16) gives the ion's secular motion. The second is a periodic motion much smaller in amplitude and modulated at the trap drive frequency. This term is dubbed intrinsic micromotion; micro-, because of its small amplitude relative to the secular motion amplitude.

In the presence of a static electric field,  $\mathbf{E}_{dc}$ , which typically arises due to stray charges around the trapping region, the solution (4.16) becomes

$$u_i = [u_{0i} + u_{1i} \cos(\omega_i t + \psi_{1i})] \left[ 1 + \frac{q_i}{2} \cos(\Omega t) \right] \quad (4.18)$$

where

$$u_{0i} = \frac{e\mathbf{E}_{dc} \cdot \hat{u}_i}{m\omega_i^2}. \quad (4.19)$$

The static field displaces the ion's average position and superimposes an additional oscillatory motion at the trap drive frequency. This is referred to as excess micromotion. This excess micromotion impedes efficient cooling and localisation of the ion and is therefore a generally unwelcomed motion. It can be nullified however simply by compensating the static field with external DC fields. This is discussed in detail in Section 8.2.

## 4.2 The fibre trap design

A modified version of the Paul trap design is used to cater for the needs of this experiment, which are:

- i. shielded integration of a fibre cavity
- ii. optical access
- iii. the ability to compensate excess micromotion in 3D

iv. the ability to move the ion's trapped position in 3D.

The basic design [41] is shown in Figure 4.2a and has been tested and proved to work with fibres. It consists of a pair of two concentric tubes, one inside the other. The pair face one another. To trap an ion in the centre, an rf signal is applied to the inner tubes while the outer tubes are held at rf-ground (or vice versa). The fibres are inserted into the inner electrodes and are therefore shielded from the rf potential. Further, as the fibres share the same symmetry axis as the trap, they do not interfere with the trapping E-field by design. This basic design addresses requirements (i) and (ii) above. To fulfil all requirements, four *side electrodes* are added in the radial plane as shown in Figure 4.2b. The side electrodes are all 1 mm away from the trap centre. Two of these electrodes are used to compensate excess micromotion in the radial plane by applying a DC bias to them. The other two serve to shift the trapping potential minimum position in the radial plane. The key geometry dimensions are outlined in Table 4.1.

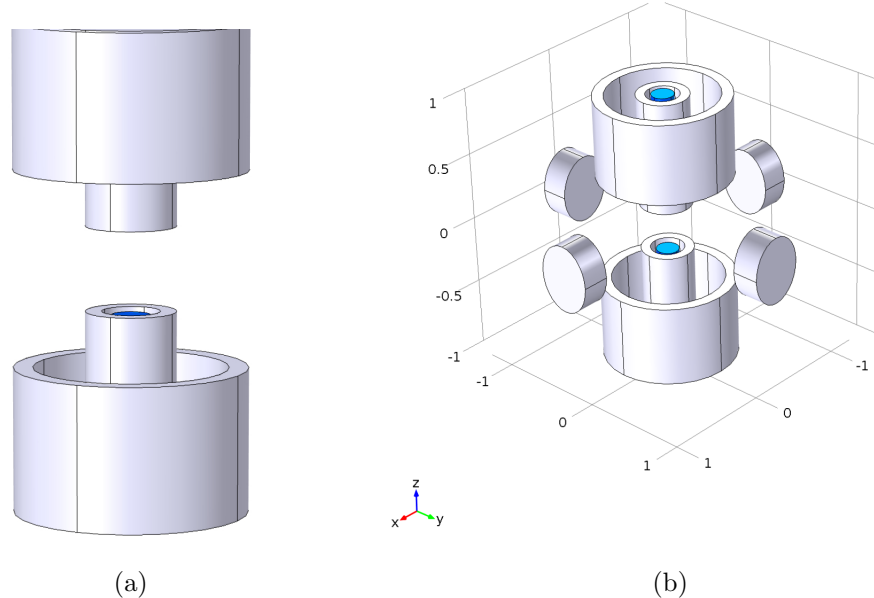


Figure 4.2: (a) The basic trap design. The inner and outer electrodes are concentric and electrically isolated from one another. The inner electrodes accommodate fibres (light blue). (b) A  $(2.5 \times 2.5 \times 2.5)$  mm<sup>3</sup> cut-out view of the trapping region. The side electrodes are used for micromotion compensation and moving the ion.

Table 4.1: Key dimensions near trapping region

Inner electrode inner diameter	$300 \mu\text{m}$
Inner electrode outer diamter	$465 \mu\text{m}$
Outer electrode inner diameter	$1000 \mu\text{m}$
Outer electrode outer diamter	$1200 \mu\text{m}$
Separation between inner electrodes	$350 \mu\text{m}$
Outer electrodes recess from inner electrodes	$230 \mu\text{m}$
Fibre recess from inner electrodes	$15 \mu\text{m}$
Side electrode diameter	$500 \mu\text{m}$
Side electrode separation from trap centre	$1000 \mu\text{m}$

### 4.3 Trap depth, pseudopotential and secular frequencies

The trap depth is the energy required by an ion to escape the trapping potential. A useful tool to compute this is the pseudopotential. The pseudopotential is the time-averaged energy of the ion in a trapping field. For an ion with charge  $e$  and coordinate  $\vec{u}(t)$  the pseudopotential is defined as:

$$m \left\langle \frac{d^2 \vec{u}(t)}{dt^2} \right\rangle = -e \nabla \cdot \tilde{\phi}, \quad (4.20)$$

where  $\langle \rangle$  denotes time averaging. For an ion experiencing an electric field  $\vec{E}(r, t) = \vec{E}_0 \cos(\Omega t)$  the pseudopotential definition yields

$$\tilde{\phi} = \frac{1}{4} \cdot \frac{e |\vec{E}(r, t=0)|^2}{m \Omega^2}. \quad (4.21)$$

A finite element modelling program<sup>1</sup> is used to simulate the pseudopotential in the fibre trap. These are electrostatic calculations. The rf frequency is only used when calculating  $\tilde{\phi}$ . Figure 4.3a shows the instantaneous potential when 200 V is applied to the outer electrodes. Figure 4.3b shows the pseudopotential a  $^{40}\text{Ca}^+$  ion sees when a 20 MHz rf drive signal of 200 V amplitude is applied to the outer electrodes. In both cases, the inner and side electrodes are grounded. With these settings, the axial trap depth is 0.6 eV and the radial depth is in excess of 1 eV (see the maximum pseudopotentials in Fig. 4.5). Cylindrical symmetry is broken because of the presence of the side electrode as can be seen in Figure 4.4. The trap depth is shallower in the  $\hat{x}$  and  $\hat{y}$  directions than in the  $\hat{x} \pm \hat{y}$  directions where there is no grounded side electrode to weaken the rf field from the

---

<sup>1</sup>COMSOL Multiphysics

outer electrodes. It can be seen in 4.5 that, near the trap centre, the presence of the side electrodes causes a negligible difference between the pseudopotentials in the  $\hat{x}$  and  $\hat{x} \pm \hat{y}$  directions.

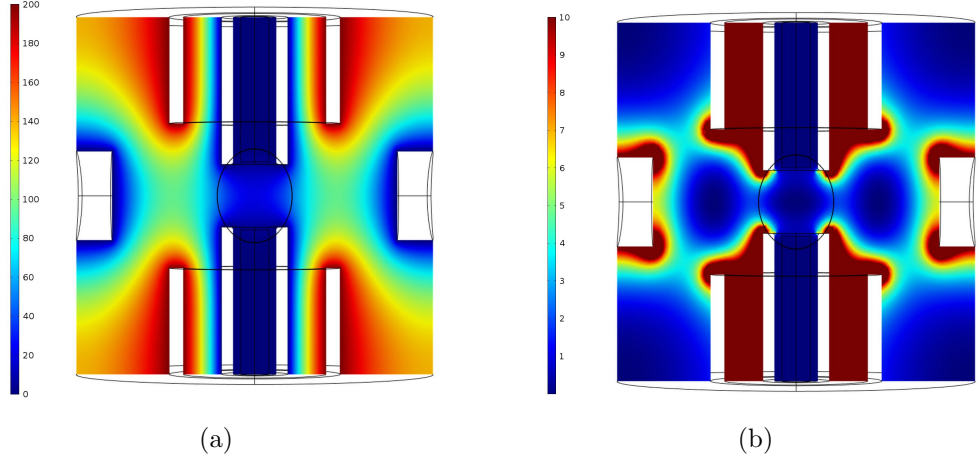


Figure 4.3: (a) A cross-sectional view of the instantaneous potential in volts when 200 V is applied to the outer electrodes whilst the inner and side electrodes are held at rf-ground. (b) The cross-sectional pseudopotential (in eV) when the trap drive is a 20 MHz ac-signal with 200 V amplitude. The side and inner electrodes are held at ground. In (b) the pseudopotential has been capped at 10 eV to use more of the legend spectrum range near the trapping region for emphasising the pseudopotential structure.

When the pseudopotential is parabolic and of the form  $\tilde{\phi} = \alpha u^2$ , we find from the pseudopotential definition (4.20) that

$$m \langle \ddot{u}(t) \rangle = -2e\alpha \vec{u}(t). \quad (4.22)$$

This is equivalent to the equation of motion in a harmonic oscillator

$$\frac{d^2 \vec{u}}{dt^2} = -\omega^2 \vec{u}. \quad (4.23)$$

Thus the secular frequency,  $\omega$  can be found from

$$\omega = \sqrt{\frac{2e\alpha}{m}}. \quad (4.24)$$

By fitting quadratic functions to the pseudopotential simulations, I extract the second order coefficients,  $\alpha$ , to find the secular frequencies<sup>2</sup>. The secular frequencies were computed for varying rf voltage amplitudes and are presented in Figure 4.6. At a typical rf voltage amplitude of 200 V, we have an axial secular frequency of

$$\omega_a = 2\pi \cdot 2.72 \text{ MHz} \quad (4.25)$$

---

<sup>2</sup>The first order coefficient is negligible

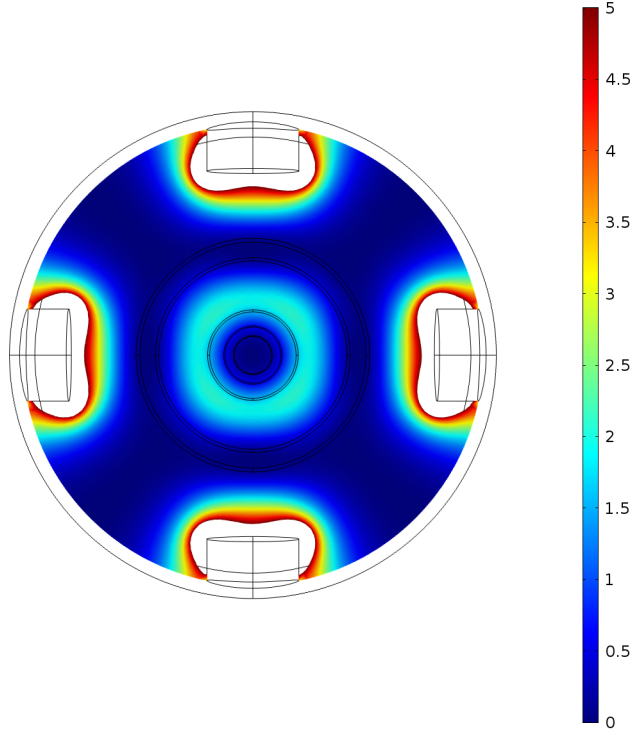


Figure 4.4: The pseudopotential in eV in the radial plane. The pseudopotential on the colour map is capped at 5 eV to place emphasis on the pseudopotential structure near the trapping region.

and radial secular frequency of

$$\omega_r = 2\pi \cdot 1.46 \text{ MHz.} \quad (4.26)$$

#### 4.4 Pseudopotential minimum vs side rf voltage

Two of the side electrodes are used to shift the ion's trapped position to optimise its overlap with the cavity mode. This is achieved by applying an rf voltage to the side electrodes. rf is used as opposed to dc because as seen in Section 4.1.2, dc induces excess micromotion. Moreover, excess micromotion can also be caused by a phase shift between the rf signals on side electrodes and the main electrodes. This is discussed in more detail in Section 8.2. Therefore the rf applied on the side electrodes must be in phase with that of the main electrodes. rf on the side electrodes shifts the pseudopotential minimum. In order to move the ion in the radial plane, side electrodes that are orthogonal to one another are used.

How much one can move the ion by applying rf signal to the side electrodes is simulated. An oscillating voltage at 20 MHz is applied to one of the side electrodes whilst the other side electrodes are held at ground. Figure 4.7a shows the cross sectional potential

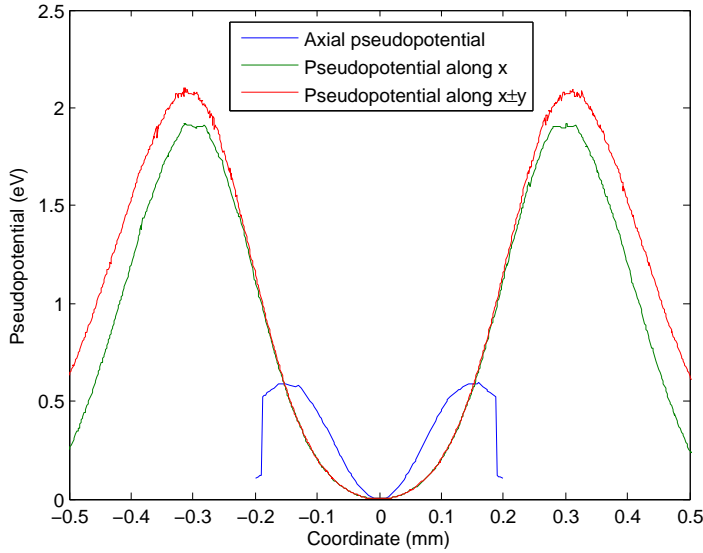


Figure 4.5: The simulated axial and radial pseudopotentials. The axial pseudopotential (blue) falls sharply at  $\pm 190\mu\text{m}$  where it meets the fibres. The wings of the pseudopotential in the x (green) and y (red) directions differ because of the presence of side electrodes. Nevertheless, the difference is negligible near the trap centre.

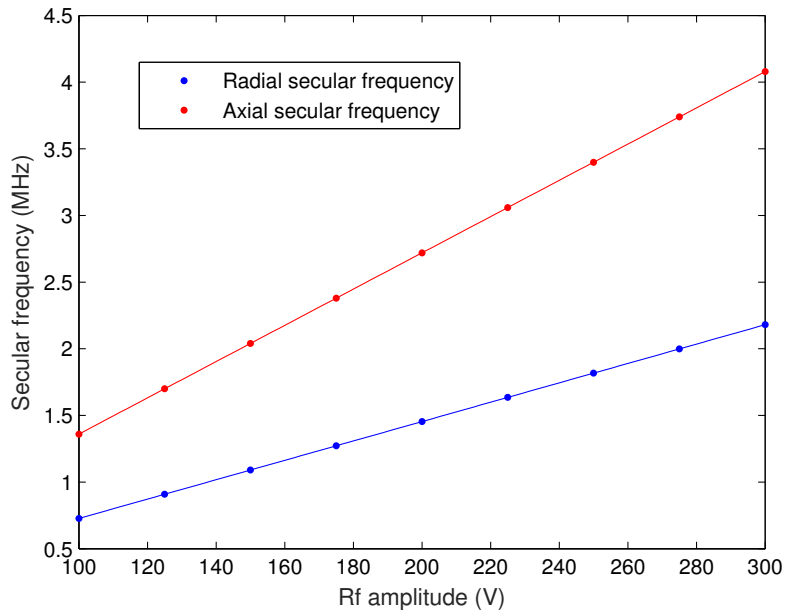


Figure 4.6: The radial (blue dots) and axial (red dots) secular frequencies computed for varying Rf voltage amplitude. The lines are linear fits. We find slopes of 7.3 kHz/V radially and 13.6 kHz/V axially.

when 200 V is applied to one of the side electrodes. Figure 4.7b shows the pseudopotential. For this setup, the amplitude is varied from 200 V to -200 V and the resulting

pseudopotentials are illustrated in Figure 4.8. Near the pseudopotential minimum, the pseudopotential-to-position relationship is well described by a quadratic function. By fitting to the simulations, I extract the pseudopotential minimum position and present it as a function of the rf-signal amplitude in Figure 4.9. It is found that we can move the ion's position from  $-16 \mu\text{m}$  to  $21 \mu\text{m}$  with  $\pm 200 \text{ V}$  range on the side electrode. The asymmetry arises predominantly because of the grounded side electrode facing the side electrode on which rf is applied. Given the concentricity of the fibres with respect to the inner electrodes we achieved (see Chapter 5), this range should suffice to correct misalignments between the ion and the cavity mode that may arise because of imperfection when assembling the set up. Note that this displacement range can be increased (i) by lowering the trap depth (i.e. reducing the rf amplitude on the outer electrodes) or (ii) by applying larger amplitudes to the side electrodes. Recall that the main rf signal is applied to the outer electrodes whilst the inner electrodes are grounded. If the main rf signal was instead applied to the inner electrodes (and the outer electrodes were grounded) it would be more demanding (in terms of side rf voltage) to move the ion radially. This is because of the grounded outer electrodes which act as a shield.

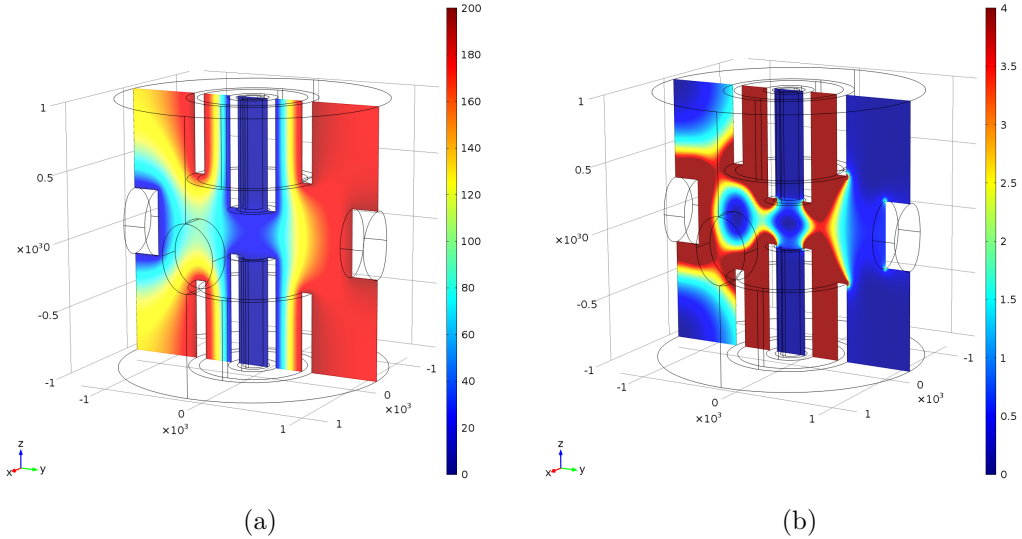


Figure 4.7: A cross-sectional view of (a) the instantaneous potential in volts at  $t = 0$  and (b) the pseudopotential in eV when a signal  $V = 200 \cos(2\pi \cdot 20\text{MHz} \cdot t)$  is applied to the outer electrodes and one of the side electrodes; the inner electrode and the remaining three side electrodes are held at ground.

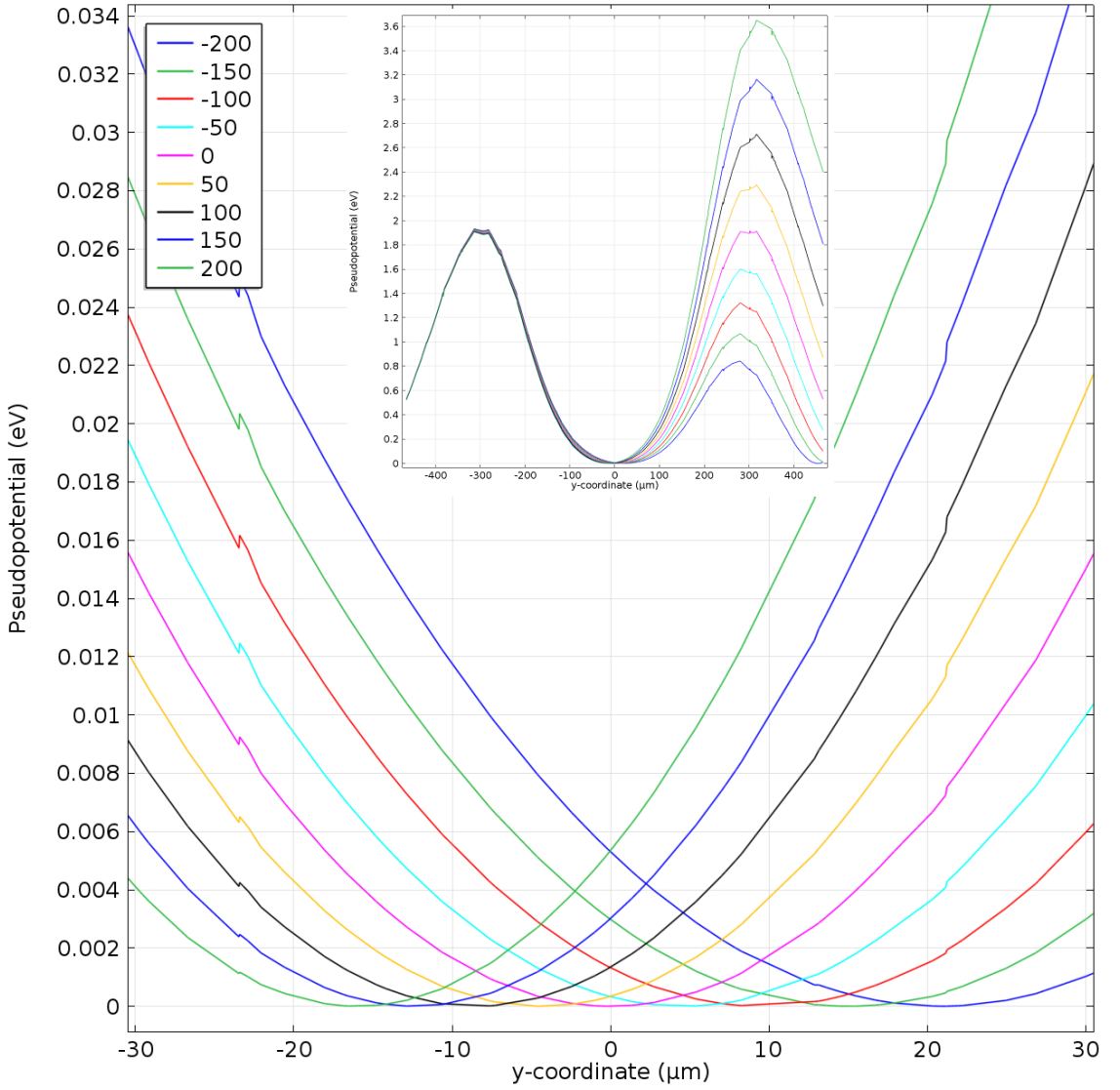


Figure 4.8: The pseudopotential as a function of position for varying rf voltage amplitudes on the side electrode. Inset, the pseudopotential for a larger position range. The duplicated legend colours can be distinguished by following the general trend of the pseudopotentials. The features around  $\pm 22 \mu\text{m}$  and  $\pm 300 \mu\text{m}$  are numerical artefacts from poor mesh refining in the finite element modelling simulations and are not to do with the trap geometry.

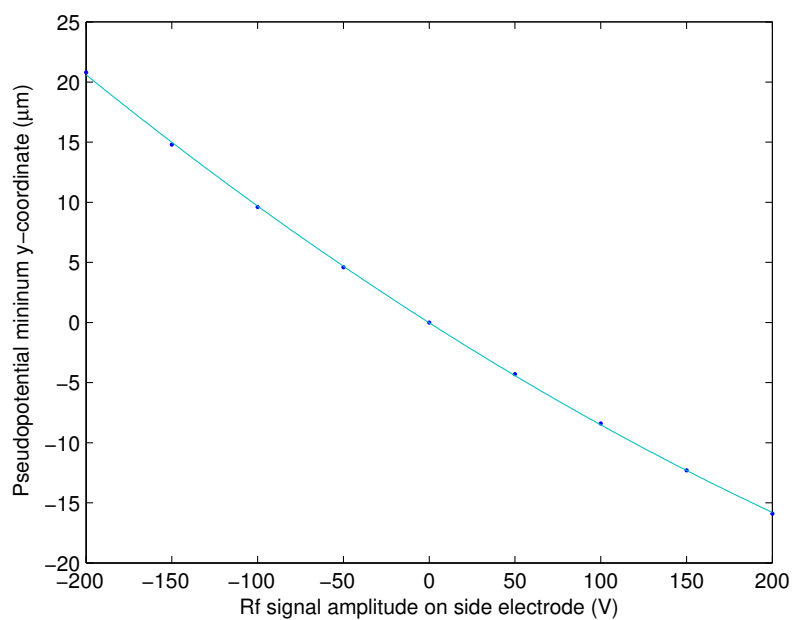


Figure 4.9: The pseudopotential minimum position vs the rf-amplitude applied on the side electrodes. In dark blue dots are the computed data points. The light blue curve is a quadratic fit revealing the ion's displacement with applied side rf voltage, as  $y = 6.1 \times 10^{-5} V_s^2 - 0.1 V_s$ .

# Chapter 5

## Cavity-trap integration

Here, I give an account of the detailed parameters of the integrated cavity-trap system. First the dimension of the electrode assemblies are laid out. The concentricity of the fibres in the electrodes is an important parameter here. This is because we want to ensure that the trapped ion's position overlaps well with the cavity mode lest we get no ion-cavity coupling.

### 5.1 Electrode assembly design

As briefly seen in the pseudopotential simulation model in Section 4.2 an electrode assembly consists of two stainless steel electrodes<sup>1</sup> (which are hollow cylinders) one inside the other. They are separated by a ceramic spacer for electrical insulation. See Figure 5.1. The assembly dimensions are given in Table 5.1.

A good concentricity between the inner electrode (IE) and the outer electrode (OE) contributes to ensuring the pseudopotential is symmetric and the ion is trapped along the axis of cylindrical symmetry of the IE. It is tricky to ensure good concentricity because the three assembly components do not have a tight fit due to mismatch in diameters. For instance, the quoted manufacturer<sup>2</sup> tolerance for the ceramic spacer diameters is  $\pm 50\ \mu\text{m}$ . The method used for making electrode assemblies and ensuring good concentricity is discussed in Appendix C.1. Figures 5.2 and 5.3 present the facet of assemblies 1 and 2 respectively.

---

<sup>1</sup>Cooper's Needle Works, 26g Thinwall

<sup>2</sup>Degussit ceramic spacers/Friatec Technical Ceramics



Figure 5.1: Left: The electrode assembly design. The inner electrode (IE) and outer electrode (OE) are separated by a ceramic spacer. The spacer protrudes out of the OE at the rear by 2 mm to allow the application of adhesives to fix the three components to one another. The spacer is also sufficiently far from the OE front facet (2 mm) that it does not alter the trapping potential. Right: Picture of the electrode assemblies mid-preparation (the rear of the IE are crimped and yet to be polished). The amber material at the rear of the assembly (circled) is the adhesive that holds the assembly together.

## 5.2 Concentricities and recesses

f112 and f108 were inserted in assemblies 1 and 2 respectively. After the insertion procedure, each fibre was recessed by  $12 \mu\text{m}$  from the inner electrode facet. See Appendix C.2 for the detailed procedure. Following this, the fibre is glued<sup>3</sup> to the electrode assembly at the rear end of the inner electrode. The glue used is a slow curing (24 hours) UHV compatible glue. Due to the long cure time, a small drift of the recess is expected. The recess was remeasured using a high magnification microscope with a short focal depth. By monitoring the translated distance of the assembly required in order to move the image focus from the fibre facet to the inner electrode, we can deduce the fibre recess.

For f112, the recess was measured to be  $15.5 \pm 0.5 \mu\text{m}$ . In the case of f108, it was more difficult to judge when the fibre was in focus. This is perhaps because of a more pronounced curvature at the edges. The f108 fibre's cladding near the edge will have endured higher intensity laser shots compared to f112 because of its large core. The f108 recess is estimated at  $18 \pm 9 \mu\text{m}$ . Recall the cavity length was accurately measured to be  $367 \mu\text{m}$  and the separation of the inner electrodes set to  $350 \mu\text{m}$ . The inconsistency suggests that the systematical error in measuring the recess of the fibres has been underestimated.

---

<sup>3</sup>STYCAST 2850-FT

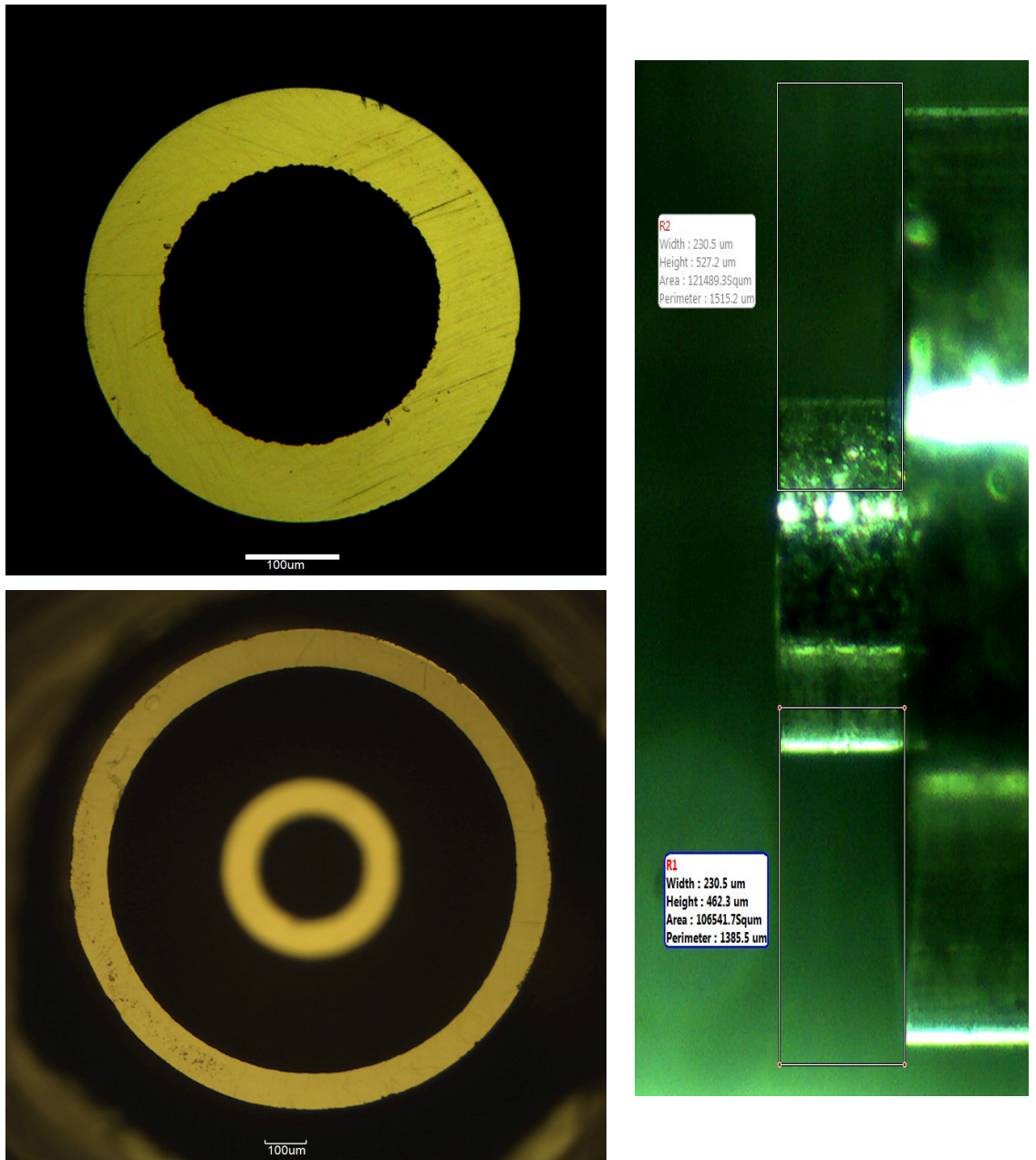


Figure 5.2: Facet and protrusion details for assembly 1 post assembling. Top left: the polished facet of the IE. Bottom left: the polished facet of the OE. The IE becomes out of focus because of its protrusion. A concentricity measurement reveals the centres of the 2 electrodes are separated by  $2.0 \mu\text{m}$ . Right: A side image of the assembly reveals a protrusion of the IE from the OE facet of  $230.5 \mu\text{m}$ .

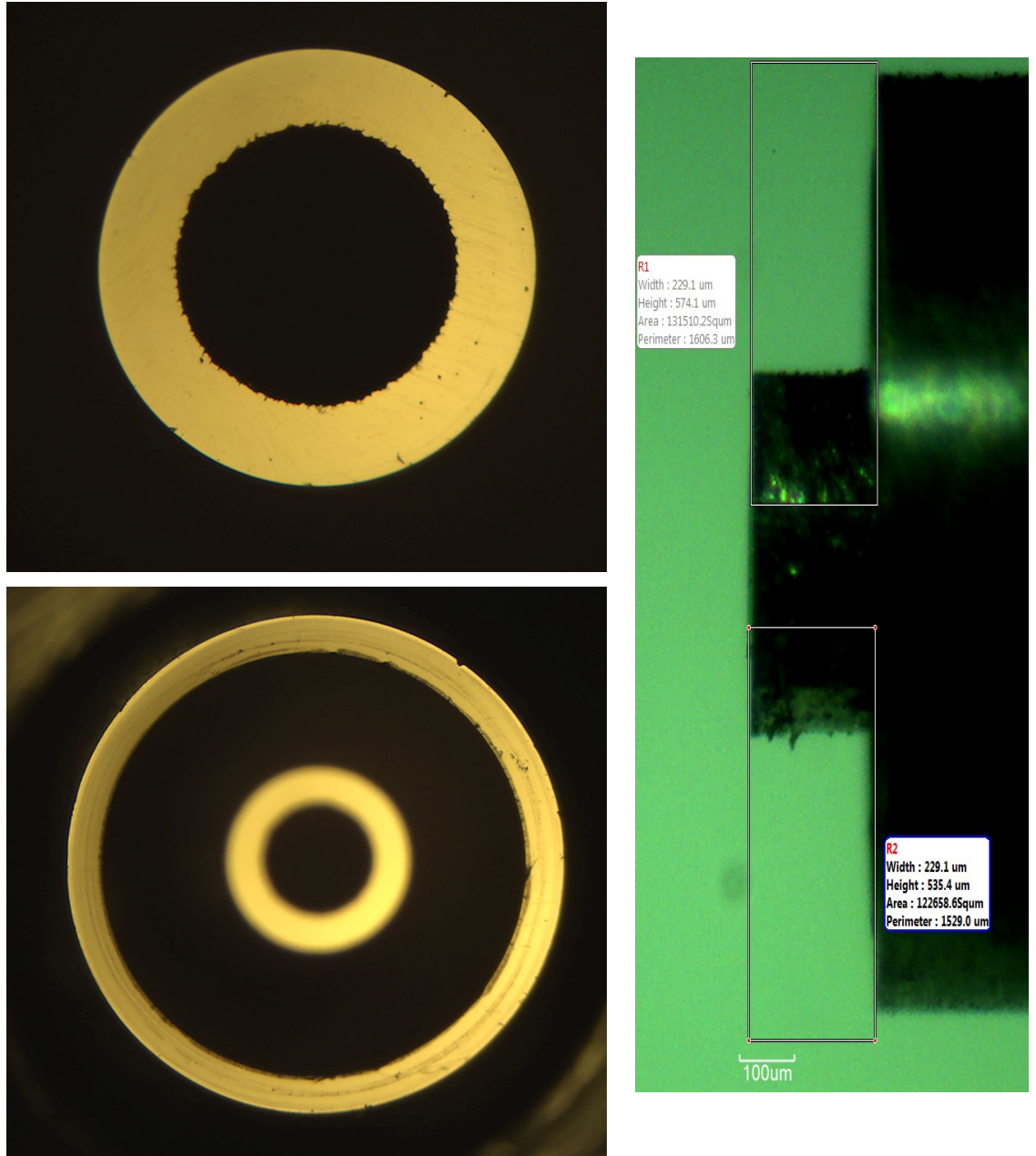


Figure 5.3: Facet and protrusion details for assembly 2 post assembling. Top left: the polished facet of the IE. Bottom left: the polished facet of the OE. The IE becomes out of focus because of its protrusion. A concentricity measurement reveals the centres of the 2 electrodes are separated by 11.5  $\mu\text{m}$ . Right: A side image of the assembly reveals a protrusion of the IE from the OE facet of 229.1  $\mu\text{m}$ .

The concentricities for the two assemblies were measured. See Figure 5.4. For assembly 1, the fibre-electrode concentricity is measured to be  $3.4 \pm 1.2 \mu\text{m}$ . For assembly 2, it is  $9.4 \pm 1.2 \mu\text{m}$ . In the worst case scenario, after aligning the fibre cavity, the ion will be trapped  $7.6 \mu\text{m}$  radially away from the cavity mode centre (see Figure 5.5). This is within the estimated cavity mode waist. With the obtained concentricities, we should therefore be able to see ion-cavity coupling without the need to move the ion.

Table 5.1: Cavity fibres' details

	Assembly 1		Assembly 2	
	IE	OE	IE	OE
Outer Diameter ( $\mu\text{m}$ )	$466.4 \pm 1.2$	$1152.7 \pm 2.8$	$466.3 \pm 1.2$	$1195.0 \pm 2.8$
Inner Diameter ( $\mu\text{m}$ )	$298.1 \pm 1.2$	$981.4 \pm 2.8$	$297.2 \pm 1.2$	$1017.3 \pm 2.4$
Length (mm)	$6.0 \pm 0.5$	$4.0 \pm 0.5$	$6.0 \pm 0.5$	$4.0 \pm 0.5$
IE-OE recess ( $\mu\text{m}$ )	$230.5 \pm 2.8$		$229.1 \pm 2.8$	
IE-OE concentricity ( $\mu\text{m}$ )	$2.0 \pm 1.2$		$11.5 \pm 2.8$	
Fibre-IE concentricity ( $\mu\text{m}$ )	$3.4 \pm 1.2$		$9.4 \pm 1.2$	
Fibre-IE recess <sup>4</sup> ( $\mu\text{m}$ )	$15.5 \pm 0.5$		$18 \pm 9$	

---

<sup>4</sup>The inconsistency of these figures with the cavity length and inner electrodes' separation (which are believed to be more accurately measured) suggests that there is a systematical error which results in the overestimation of the recesses.

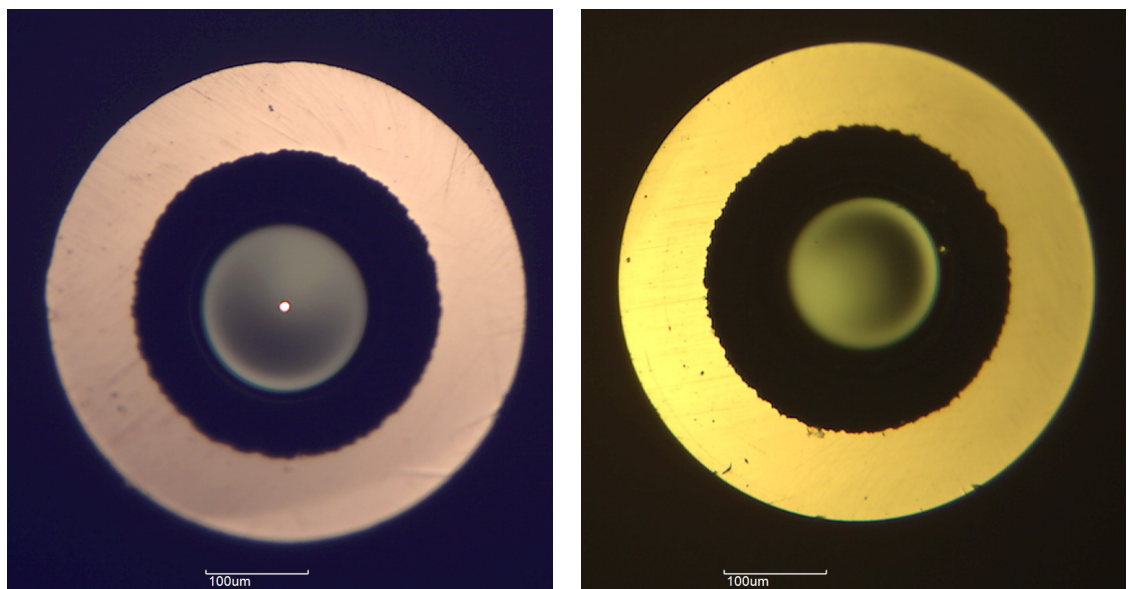


Figure 5.4: Left: Fibre f112 after being inserted and glued to assembly 1. The image shows the facet of the fibre and the inner electrode. The core of the fibre is illuminated by a red laser pen. A circle is fitted to the inner electrode to assess the concentricity of the pair. The centres are separated by  $3.4 \mu\text{m}$ . Right: Fibre f108 after being inserted and glued to assembly 2. Since the core of this multimode fibre is large, it is moot to illuminate it to find the centre. A circle is fitted to both the fibre and the inner electrode to assess the concentricity of the pair. The centres are separated by  $9.4 \mu\text{m}$ .

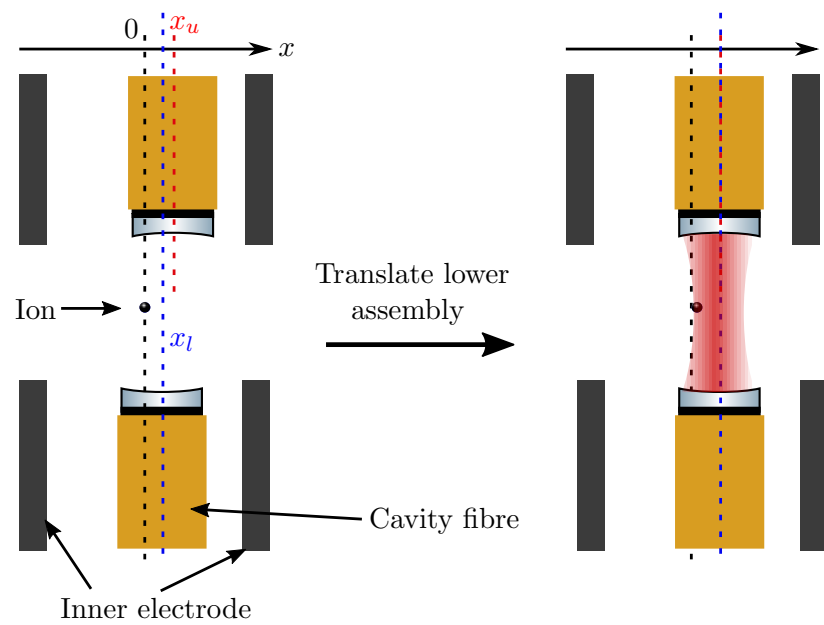


Figure 5.5: Cross sectional schematic of the alignment of the cavity and the resulting ion-cavity overlap. Left: The upper and lower inner electrodes are concentric. Here, the ion is trapped at position  $x = 0$ . The axis of symmetry of the upper inner electrode is used as a reference. The centre of the upper fibre is at  $x_u$  (red dotted line) and that of the lower fibre is  $x_l$  (blue dotted line). Right: the lower assembly is translated by  $x_u - x_l$  to align the cavity. As a result the ion is trapped at  $x = 0.5(x_u - x_l)$ .

# Chapter 6

## Ion trap and system assembly

In this chapter, the aggregate system is described. It will be seen that though the trapping region is miniaturised, the system as a whole is significantly larger. This is partly to accommodate mechanical and electrical translational stages used for the alignment of the cavity. Another key reason for the bulkiness is the consideration of mechanical vibration isolation for stable locking of the cavity length.

### 6.1 The cage and blocks

Figure 6.1 shows an image of the trap system. At the top is the *cage*<sup>1</sup> wherein trapping happens. The cage sits upon *block 1*<sup>2</sup> which contains mechanical and electrical translation stages for coarse and fine alignment of the cavity respectively. On this block and immediately outside the cage, a Macor platform supports the calcium filled oven. Figure 6.2 offers a detailed view. The oven's atomic flux is aimed at a collimator<sup>3</sup> which guides the atomic flux to propagate between the trapping electrodes. The electrically isolated nuts on either side of the oven support are used as DC supply platforms for the winding<sup>4</sup> around the oven as can be seen in the bird's eye view in figure 6.3.

The upper fibre (f112) is guided from the top of the cage to the side of block 1 where it is clamped between teflon wedges for strain relief (see figure 6.4). Also from this figure we can see where the rf signal is applied and how it is isolated from the rest of the system.

---

<sup>1</sup>Made of stainless steel

<sup>2</sup>Made of stainless steel

<sup>3</sup>Stainless steel tube of diameter 0.5 mm. The collimator is crimped at the trapping region side only to leave a slit opening of 240 um. This is to mitigate large deposits of calcium on the trapping electrodes and fibres.

<sup>4</sup>Tantalum wire is used for its high melting point to support the large currents used for resistively heating the oven.

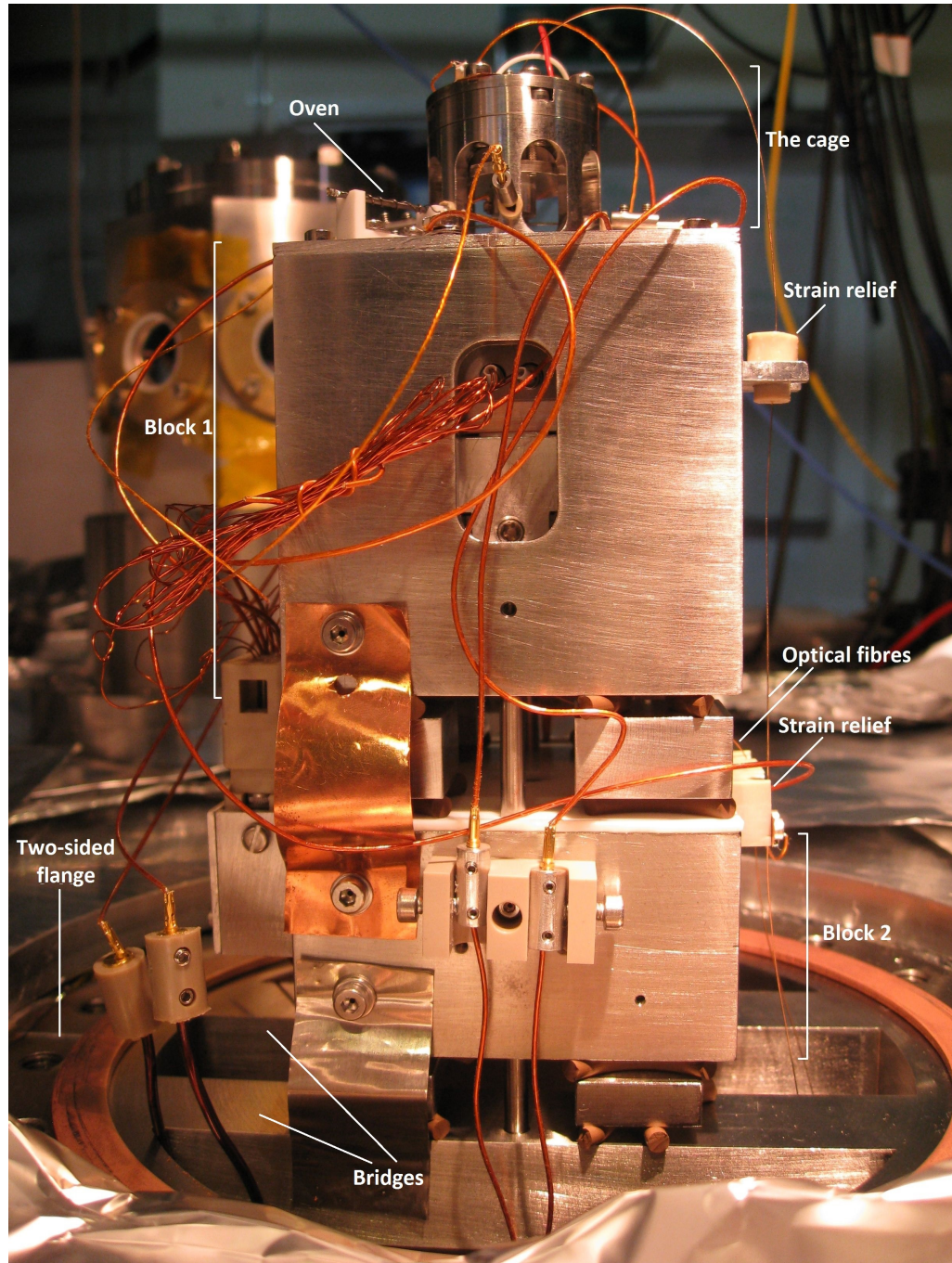


Figure 6.1: A two-sided flange is fixed to an optical table. On its bridges, the trap is assembled. A rod from each bridge runs vertically up through block 2 and part of block one as a precautionary measure to keep the system from toppling. Cuts of UHV compatible Viton rings are used to provide vibrational isolation between the bridges and the blocks. Further details are given in the main text.

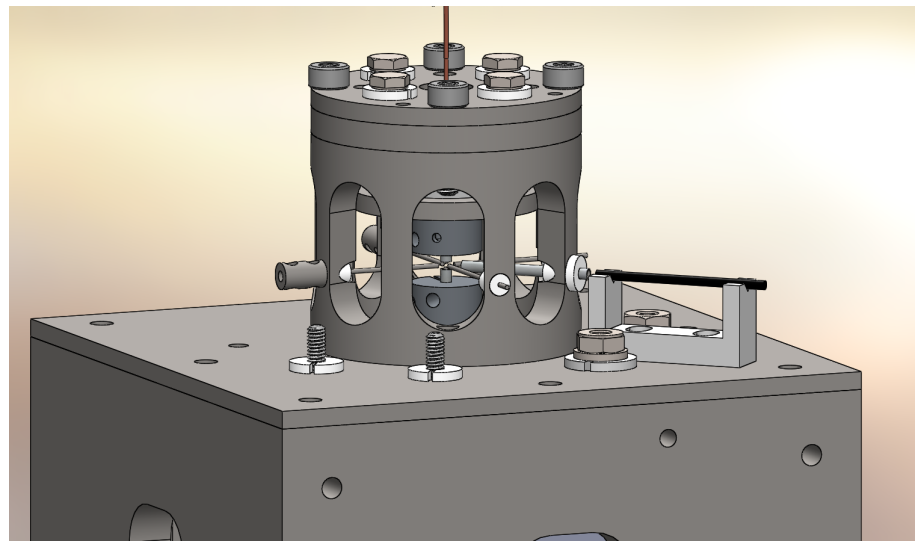


Figure 6.2: A close up schematic of the cage and oven. The oven is aimed at a collimator whose role is to collimate the atomic beam between the trapping electrodes. The cage has 8 windows for optical access.

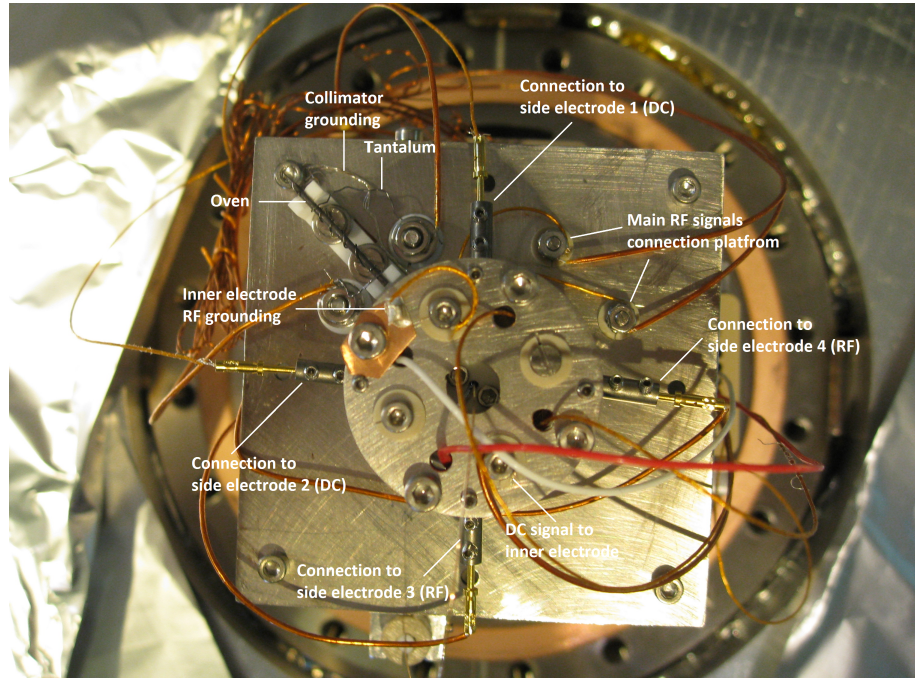


Figure 6.3: A bird's eye view of the cage and block 1. Fibre f112 can be seen exiting the cage at the centre. The 4 wires entering the cage are for driving piezos used for nano-position control of the fibre.

Both electrode assemblies are held by stainless steel hollow cylinders (*cone-mounts*<sup>5</sup>) using grub screws. Rf is applied to these cone-mounts for driving the trap. For this, intermediary wires are conductively glued<sup>6</sup> to one of the grub screws (see inset of Figure 6.4). These wires are then connected to an rf connection platform atop block 1 (see at 1 and 2 o'clock of the cage in Figure 6.3). These intermediate connections are used to relieve the trapping electrodes (and therefore the fibre cavity by extension) from any tension and mechanical vibrations. The second grub-screw on the cone-mount is used to fix the electrode assemblies to the cylinders. The cylinders are attached to the rest of the system via Macor connectors (in white in figure 6.4).

As shown in appendix C.1, flexible wires are also attached to the inner electrodes. These are used for rf-grounding the inner electrodes and applying a DC bias.

The side electrodes and the oven collimator are held by the cage but are electrically isolated from it by PEEK spacers. DC and rf are applied to the side electrodes via barrel-connected wires. The oven collimator is grounded by a wire welded to the collimator on one side and connected to the block on the other. The blocks and cage are electrically grounded.

*Block 2* (fig. 6.1) has a thin teflon layer above it. This is to avoid any electrical contact between the lower fibre and the block as the fibre curls around under block 1 before it is fixed at the strain relief on block 2. Recall that the fibre is copper coated and that it is concentric with the inner electrode and glued with a non-conductive adhesive. Despite this, electrical breakdown may occur because of the thin layer of glue. On block 2, there are also interfaces for side rf and DC connections.

The whole set up rests on the bridges (see fig. 6.1) of a two-sided flange. The flange has four arms used to fix it to the base of an optical table. Metal sheets are used to ground block 1 and 2 to the flange. Block 1, 2 and the flange are separated by small stainless steel block sandwiched between cuts of Viton rubber rings for vibrational isolation of the trapping region from the rest of the system.

Running the experimental fibres all the way through feedthroughs to the air side is impractical. The fibres have to be connectorised with ferrules and then mated with fibres from the feedthroughs. For the multimode fibre (f108), this is a relatively straight forward task because very little transmission loss is incurred when mating the 200  $\mu\text{m}$  diameter fibres. On the other hand, when mating single mode fibres of typical core diameter of 6

---

<sup>5</sup>Made of aluminum. The name cone-mount is adopted from the previous designs where the cylinders were cone shaped.

<sup>6</sup>EPO-TEK H21D

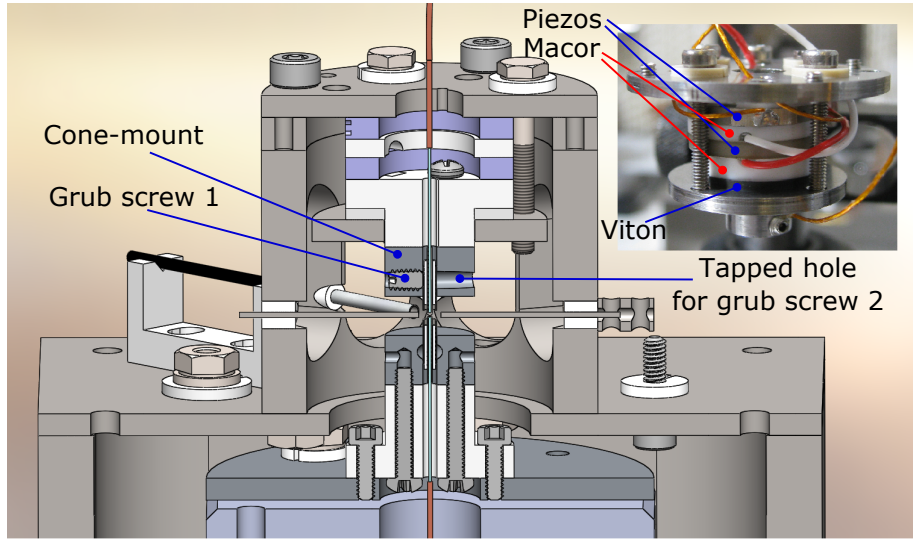


Figure 6.4: Cross section of the cage and upper part of the block. There is a passage for both fibres along the central axis of the trap. Inset: An image of the upper assembly. The beige rings are piezos, the white rings are Macor. The black ring is a Viton<sup>7</sup> ring used to allow compression in order to change the cavity length with the piezos.

$\mu\text{m}$ , a small misalignment will result in detrimental losses. A tightly fitting ferrule must be used. The only fibre for which we could find fitting ferrules was the *IVG 600/125* which has a standard cladding diameter of  $125 \mu\text{m}$ . For this reason, the f112 fibre was spliced to this fibre. The resultant was subsequently mated with a home made feedthrough using the same fibre. The total transmission including the splice efficiency and the connectorisation losses is estimated to be 70%.

### 6.1.1 Cavity alignment

For precision radial alignment of the fibre cavities, an *xy piezo*<sup>8</sup> is used to move the lower assembly in the x-y plane. For coarse alignment a mechanical stage on which the xy piezo sits is used. To lock or scan the cavity length, the stack of ring piezos on the upper assembly is used (see figure 6.4). One long range<sup>9</sup> (multilayer) piezo and one short range<sup>10</sup> (monolayer) piezo separated by Macor spacers are used. More details on the piezos are given in Table 6.1.

---

<sup>7</sup>UHV compatible, VACOM

<sup>8</sup>Piezojena systems PXY100

<sup>9</sup>Noliac multilayer NAC2124-C04

<sup>10</sup>Noliac monolayer NCE51-Ring-OD15-ID9-TH2

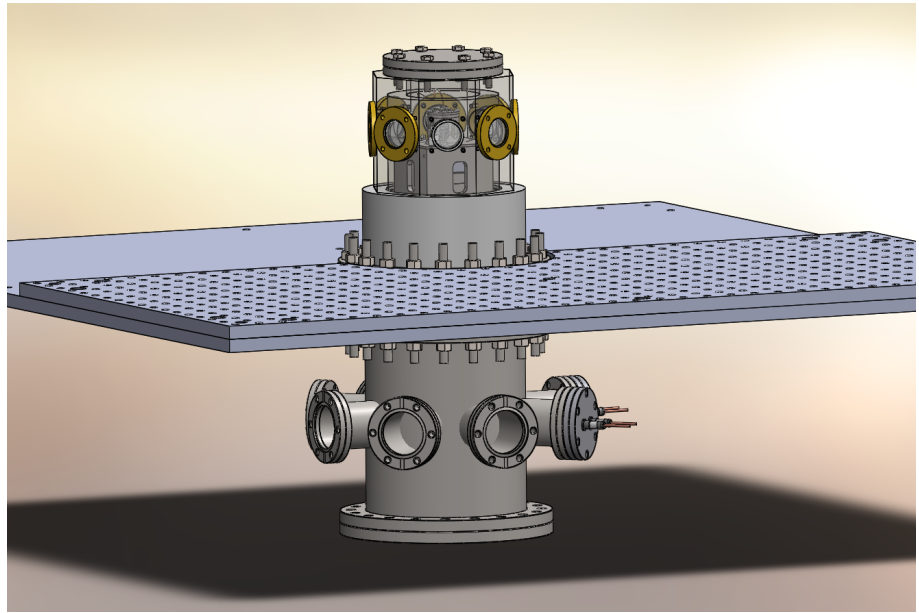


Figure 6.5: The system minus some feedthrough connections and vacuum pumps. The chamber lid and one of its brass window supports have been made transparent in order to reveal block 1 and the cage. Below the breadboard, an eight-way reducer cross is attached to the two-sided flange for the attachment of various feedthroughs. The rf input feedthroughs are shown for example.

	xy piezo	Monolayer ring	Multilayer ring
Range ( $\mu\text{m}$ )	100	1.575	3.675
Stroke (nm/V)	667	0.45	1.50

Table 6.1: Piezo ranges and strokes

## 6.2 Vacuum system

A chamber is used to seal the system above the two-sided flange. The chamber diameter is 14 cm. A drawing can be seen in figure 6.5. A picture of the chamber is also visible in the background of figure 6.1. The chamber has windows aligned with those of the cage for optical access. The windows are coated for anti-reflection at the optical wavelengths of interest. They are 397 nm and 866 nm. The windows are sealed to the chamber with indium. Brass clamps with teflon spacers are used to maintain the seal.

Attached below the two-sided flange is an eight-way reducer cross where various feedthroughs are used for interfacing with the vacuum chamber. See the schematic in figure 6.5. The feedthroughs used are

1. a home made fibre feedthrough for the input fibre,
2. a commercial fibre feedthrough<sup>11</sup> for the output fibre,
3. a gate valve for gating a turbo pump,
4. a multipin electrical feedthrough<sup>12</sup> for DC connections,
5. a 2-pin power transmission feedthrough<sup>13</sup> for both main and side rf signal inputs and
6. an ion gauge<sup>14</sup>.

The base of the nippled tube is connected to an ion pump<sup>15</sup> mediated by a bellow.

### 6.2.1 Baking and pressure

All the materials used in the chamber are UHV compatible and high temperature rated. The system was baked for two weeks while pumping it down with a turbo pump. The baking temperature constraints were 156°C for the indium sealing the windows, 200°C for the fibre feedthroughs, 150°C for the *xy* piezos and 130°C for the ring piezos. The chamber above the optical table was baked at slightly under 100°C; the eight-way reducer cross was baked at 130°C; the ion pump was baked at 150°C. When cooling down to room temperature at the end of the baking period, in order to avoid condensation near the trapping region, the temperature atop the optical table was kept higher than the rest of the chamber.

Following bake out, the ion pump was flushed<sup>16</sup> before being turned on indefinitely. Subsequently, the turbo pump station is removed. The trap is operational at  $4.1 \times 10^{-10}$  mbar. This pressure is gauged from the ion pump current. The ion gauge is not in use as it was found to contribute a fixed rise in pressure when operational as well as causing mechanical vibrations. Its readings were nonetheless consistent with those of the ion pump.

## 6.3 Resonator and drive

For supplying high voltages at rf to the trapping electrodes a helical resonator following the design of [62] is used to set up an effective LCR system. The system quality was

---

<sup>11</sup>Lewvac FOA-I200-40CF

<sup>12</sup>Lewvac Mil-C-26482

<sup>13</sup>Lewvac FHP5-180C2-40CF

<sup>14</sup>IONIVAC IE 514

<sup>15</sup>Varian VacIon Plus 300 Starcell

<sup>16</sup>A process of intermittently turning the pump on and off that speedily rids it of contaminants.

measured to be  $Q = 125$  and its resonance frequency  $\Omega = 2\pi \cdot 19.57$  MHz.

An function generator is used to generate a resonant ac signal which is fed to a 30 dB amplifier. The amplified output is passed through a reflectometer before being fed to the helical resonator. The system impedance will have already been matched by tuning the primary coil of the helical resonator and monitoring the reflected signal. The typical trapping power is  $\leq 0.5$  W with very low reflection.

## 6.4 Magnetic field compensation coils

In the experiment, we would like to have a well defined magnetic field at the trapped ion's position. This means we need to compensate any ambient magnetic ( $B$ ) fields at the trap centre and chose a custom  $B$  field direction and magnitude. For this, 3 pairs of coils have been built around the chamber. See Figure 6.6 for an image of the coils around the chamber. We use a primed coordinate system for the magnetic field directions as is shown in Figure 7.1. Each coil mount on the  $x'y'$  plane has 600 turns and inner diameter of 40 mm. The top and bottom coils mounts have 85 turns each and diameter 17 mm. With these coils we can generate circa 6 G/A, 6 G/A and 20 G/A in the  $x'$ ,  $y'$  and  $z'$  directions respectively.

The coils are much larger than one would ordinarily expect for compensating  $B$  field contributions from Earth and typical lab equipment. This is because it transpired long after building the trap that the trapping and side electrodes are weakly magnetic. This was unexpected from the material of the electrodes.  $B$  field measurements of sample electrodes using Hall effect detectors revealed a magnitude of more than 10 G at similar distances from the electrodes as the intended ion-electrode separation. The magnetic field compensation is detailed later.

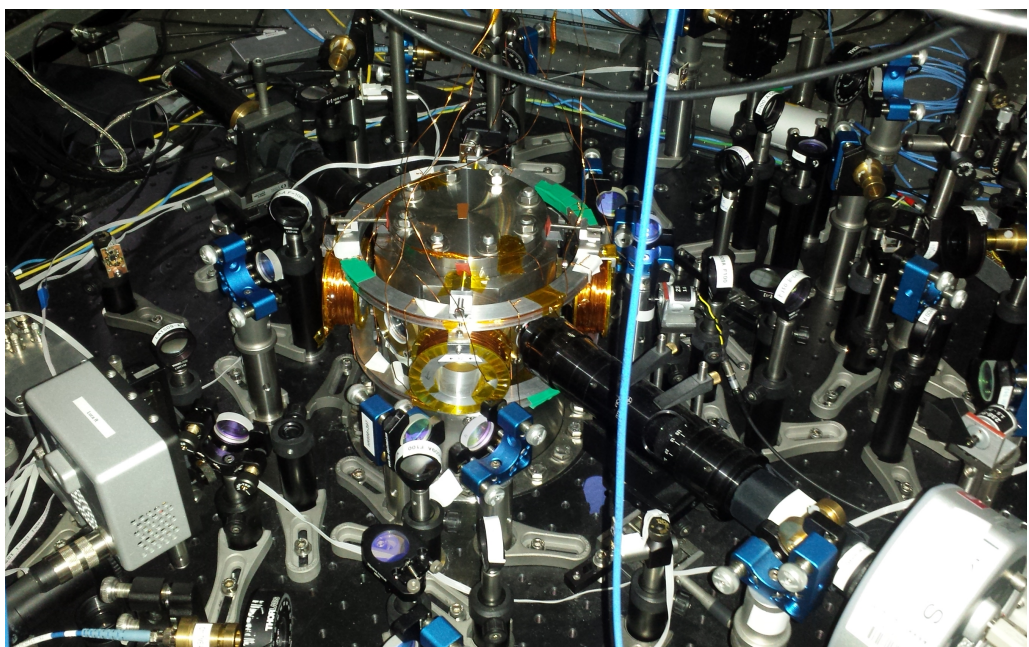


Figure 6.6: Image of the magnetic field compensating coils around the chamber. Some of the optical set-up is visible here but is discussed in full in the chapter that follows.

# Chapter 7

## Laser system, optics and fibre cavity locking

### 7.1 Lasers

Here, the optical setup is described. Figure 7.1 shows a schematic of all the free space lasers and optics used around the trap. The schematic is a projection on the horizontal (x-y) plane. All the lasers in this figure are sourced from polarisation maintaining fibres. The optics concerning the cavity are illustrated in Figure 7.2 and discussed later. Refer to these figures in conjunction with the descriptions that follow.

#### Ionisation lasers

We employ a resonant two-step photo-ionisation procedure to ionise  $^{40}\text{Ca}$  atoms to  $^{40}\text{Ca}^+$  [63, 64]. A 423 nm laser resonantly excites the atomic flux from the oven to a higher energy level,  $4^1\text{P}_1$ . A 375 nm laser ionises the excited atoms (Appendix A). The two ionisation lasers are independently aligned and focused at the trap centre for better loading efficiency. Combining these two lasers into one fibre can make the process less efficient because the two wavelengths are differently focused and refracted by the focusing lens and the chamber windows. We use around 150  $\mu\text{W}$  of 423 nm laser and 35  $\mu\text{W}$  of 375 nm laser to load. Typical loading times are between 20 and 30 seconds.

#### Cooling/pump beams

To fully compensate excess micromotion in 3D, three laser cooling beams are required. The lasers' propagation vectors must not be parallel nor all lie on the same plane. Ideally, they would form an orthogonal basis but due to the geometrical restrictions, namely the lack of free space optical access along the z-direction, compromises must be made.

The 397 nm cooling beams are referred to as *beam 4*, *beam 6* and *beam 7*<sup>1</sup>. They enter

---

<sup>1</sup>The nomenclature of these beams comes from the numbering of the branch path in the laser distribution setup from which they are sourced.

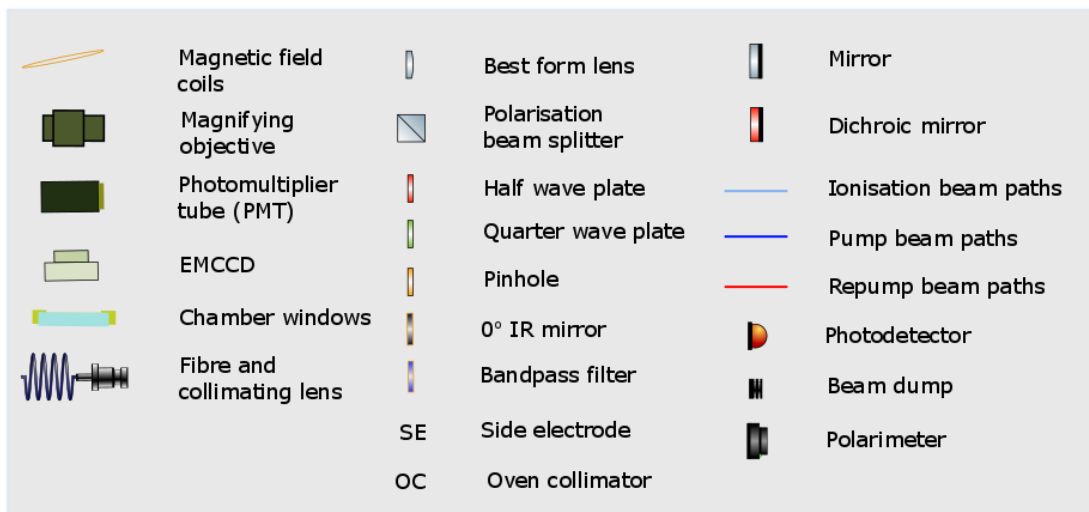
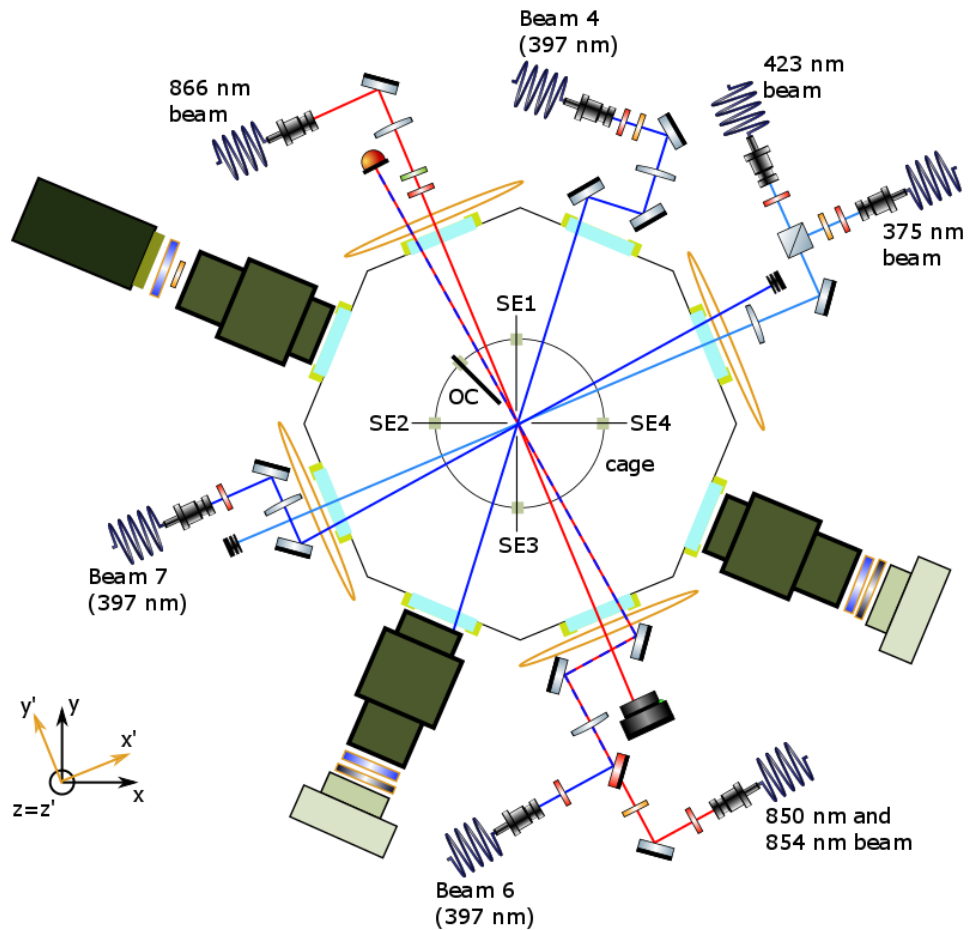


Figure 7.1: The optical set up around the trap. The non-primed coordinate system is used to define the DC voltage space in accordance with the voltages applied on side electrodes 1 and 2. The primed coordinate system is used as the B field basis.

the trap with angles  $7.8^\circ$ ,  $-8.6^\circ$  and  $\sim 7^\circ$  respectively from the horizontal plane. At the ion position, beam 4, beam 6 and beam 7 have angles  $46.5^\circ$ ,  $6.5^\circ$  and  $91.5^\circ$  respectively from the  $y'$  axis. Each cooling beam path uses a best form convex lens of focal length  $f = 100$  mm (in addition to collimation lenses at the fibre output). This is primarily to minimise the beam spot size at the ion (to reduce scatter). The fibre collimation lens focuses the fibre output  $2f$  behind the best form lens which itself is  $\sim 2f$  away from the ion.

With knife edge measurements on a replica setup, we have deduced a waist (radius) size of  $\sim 17\mu\text{m}$  at the ion's position for the cooling beams. In the path of beam 4, a pinhole is added at the focus of the fibre output to *clean* the beam and remove any halos.

### Repumpers

The 850 nm and 854 nm lasers are combined into one fibre and brought over to the trap. These repumping lasers are made to co-propagate with beam 6 (cooling beam) after combining them at a dichroic mirror. The best form lens on the beam 6 path is also used in a similar scheme as for the cooling lasers to minimise the repumpers' beam waist. A pinhole after the fibre output is used to rid the beam of halos and reduce scatter. The waist of these repumpers at the ion's position is measured to be  $16 \mu\text{m}$  on a replica setup.

The 866 nm repumper undergoes the same focusing method. This beam is on the horizontal plane and is co-propagating with the direction of the B-field generated by the coils along the  $y'$  axis. This choice allows for easier magnetic field compensation. A half wave plate (HWP) and a quarter wave plate (QWP) are added to this branch for polarisation control when compensating the stray B-field. On the other side of the chamber, a polarimeter can be placed to analyse the beam's polarisation.

## 7.2 Imaging optics

To visualise the ion's position in 3D, two EMCCD<sup>2</sup> cameras are used. The cameras are oriented orthogonally on the radial plane. This way orthogonal planes can be imaged.  $5\text{-}10\times$  objectives are used to magnify the images. Appropriate filters<sup>3</sup> are inserted before the EMCCDs.

The ion's position in 3D is useful information in two key tasks. The first is when performing coarse compensation of excess micromotion where we record the ion's average position at different trap depths. The second is when probing the relative ion-cavity coupling strength at different ion positions on the radial plane. There is however not

---

<sup>2</sup>Andor Luca R and Andor Luca S

<sup>3</sup>A  $0^\circ$  IR HR mirror and a Semrock brightline 395/11nm bandpass filter

enough resolution power to quantify the ion-cavity coupling versus the axial position of the ion since the spatial variation of the cavity field occurs on much finer scales in the axial direction.

The camera images are also used when first aligning the laser beams to the trap centre. The beams are pointed at and focused on the trapping electrodes as a good starting point for alignment. The beam spot image on the electrodes can also be used to gauge the minimisation of the beam waist.

### 7.3 PMTs

A free space PMT collects the ion's fluorescence. The ion's fluorescence is focused at the centre of a  $50\ \mu\text{m}$  pinhole by a  $\times 5$  objective<sup>4</sup> before impinging on the PMT. The pinhole significantly reduces scatter collection and thus improves the signal to noise ratio (SNR).

With the collection happening 7 cm away from the ion, the detected signal is a small fraction of the fluorescence. Up to about 10 000 counts per second can be detected on a background of 300-400 counts per second.

There is a second optional method to collect fluorescence which is especially useful when trapping for the first time. This method is to directly collect the ion fluorescence from the output fibre. This is done through the lower of the two cavity fibres which is a multimode fibre and is only  $190\ \mu\text{m}$  away from the ion. There is a caveat however. The 397 nm fluorescence is completely drowned in scatter from the electrodes. The solution is to detect 393 nm fluorescence only (of the  $P_{3/2} \leftrightarrow S_{1/2}$  ionic transition) by filtering out any 397 nm light for a background free detection [65]. The main advantage of this method is that no free space alignment is required.

### 7.4 Laser frequency stabilisation

For operations that do not require well-tuned frequencies, the lasers are locked to a wavelength meter<sup>5</sup> accurate to 10 MHz. Otherwise, a frequency stabilisation system has been built to stabilise the lasers to within 500 kHz. An 894 nm laser is stabilised to an atomic transition in Cs. The stability of the 894 nm laser (60 kHz) is transferred to other lasers by means of a scanning-cavity-transfer lock (SCL). Both the stabilisation of the laser and the stability transfer are described largely in [66, 67]. Instead of polarisation

---

<sup>4</sup>Nikon MM series, NA = 0.13

<sup>5</sup>High Finesse WS-6

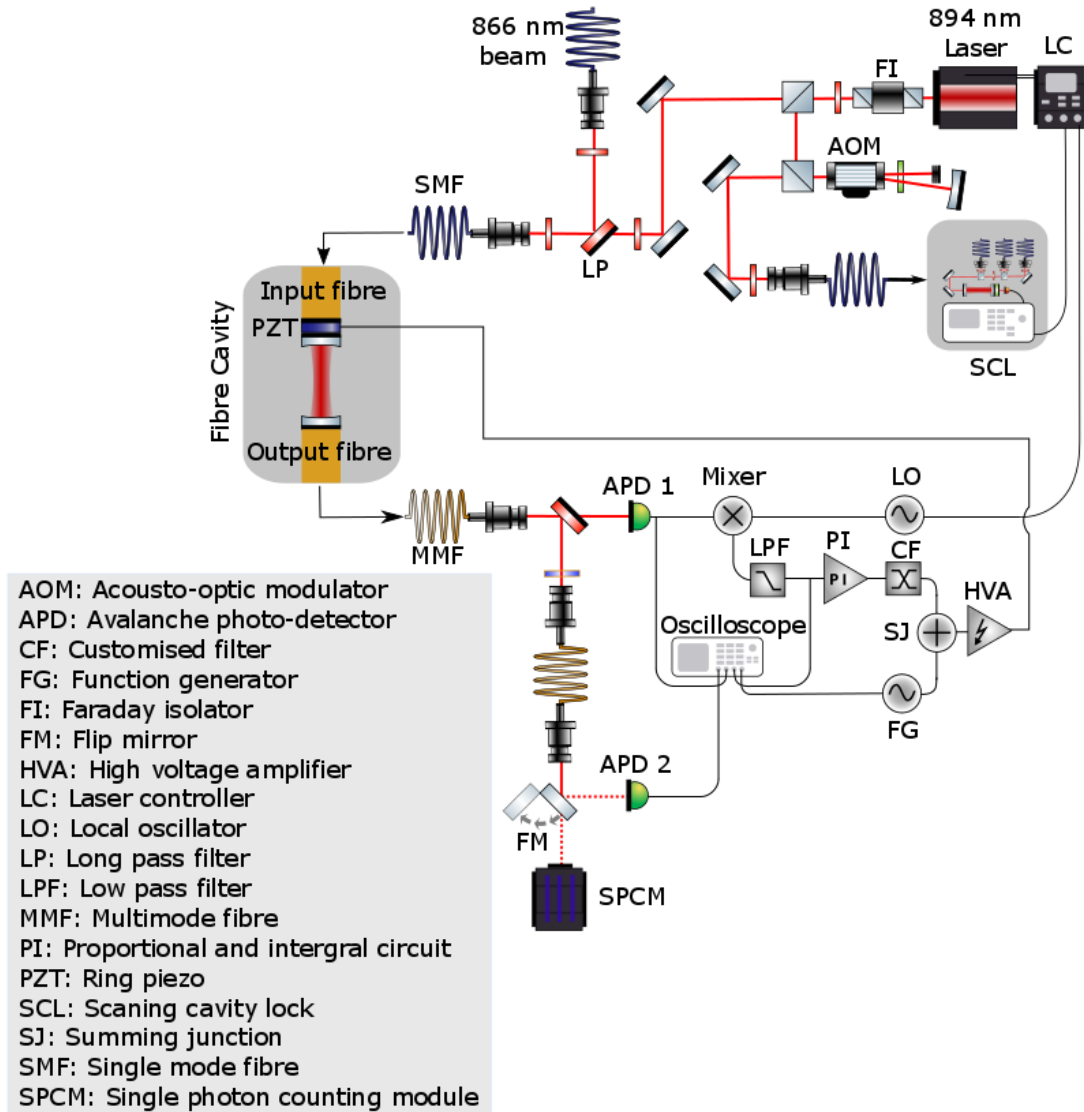


Figure 7.2: The optical and electrical set up for cavity locking. The optical components are described in the legend of figure 7.1.

spectroscopy, saturated absorption spectroscopy is now used. The locking electronics have also been upgraded.

## 7.5 Locking of the fibre cavity

The piezos used for scanning and locking the fibre cavity length have been described in section 6.1.1. The optical and electrical set up is illustrated in figure 7.2.

An 894 nm diode laser is used for locking the cavity. This 894 nm laser is different to that used in the SCL. It cannot be the same for reasons that will become apparent shortly. The 894 nm beam is spatially overlapped with an 866 nm beam which is tuned

to the atomic transition in  $^{40}\text{Ca}^+$ . The overlapped beams are fibre-coupled to the cavity. The cavity length is scanned by driving the ring piezos (PZT) with a ramp signal from a function generator (FG). The cavity output is detected by two avalanche photo-detectors (APDs). The 894 nm and 866nm resonance peaks are traced on an oscilloscope. The 894 nm laser's wavelength is tuned to overlap the two resonance peaks such that when locking the cavity to the 894 nm laser, the cavity is simultaneously locked to the 866 nm transition in  $^{40}\text{Ca}^+$ . Once the 894 nm wavelength has been set, it is frequency stabilised by the scanning cavity lock (SCL) which feeds back to the laser.

A dichroic long pass mirror (866 LP) combines the 866 nm and 894 nm lasers at the input side of the fibre cavity. This dichroic mirror reflects 866 nm light and transmits longer wavelength. Its transmission, however, is highly polarisation dependent. As a result the LP filter on the output side of the fibre only performs slightly better than a 50:50 beam splitter in filtering out the 894 nm light (whose polarisation is scrambled at the output due to the multimode fibre).

On the reflected branch of the dichroic mirror, a bandpass filter is used to filter 866 nm from the beam before coupling it into a multimode fibre (MMF). The output of this fibre is either coupled to APD 2 or a single photon counting module (SPCM). This is represented in the schematic with a flip mirror (FM). The output is coupled to APD 2 for using the 866 nm resonance peak on the oscilloscope as a reference for tuning the 894 nm laser. Once this has been done, the fibre is plugged to the SPCM for measuring the 866 nm cavity emission rate.

To lock the cavity length, the Pound-Drever Hall (PDH) technique [68] is used in cavity transmission. A local oscillator (LO) modulates the laser current. The LO signal is also mixed with the APD 1 signal before passing through a low pass filter (LPF) to generate an error signal. A proportional and integral circuit (PI) generates the required signal for the piezos to stabilise the cavity length. A high voltage amplifier (HVA) provides the necessary gain. Because of the distinct response function of the combined piezo and feedback system, it becomes necessary to include a custom filter (CF) in the feedback loop. The system response function is further described in section 7.5.1.

Once the cavity is locked, the lock point (or the cavity length) is easily tuned and scanned by adjusting the modulation frequency (FM) of the acousto-optic modulator in the branch of the 894 nm laser setup that goes to the SCL. The double pass AOM setup sends a frequency-shifted beam to the SCL. As the frequency of this beam is changed by tuning the AOM, the SCL will feedback to the laser to recover the AOM-branched beam's

original frequency. In the process, the main laser's frequency will have been shifted by the same amount the AOM has been shifted. As the cavity is locked to the main branch (without an AOM), it will follow changes in the main laser's frequency.

### 7.5.1 System response function

For a stable cavity lock using a PI feedback, the system should ideally respond uniformly (in gain and in phase) for different feedback frequencies. This is not the case in practice as the impedances of the various components (piezos, HVA, etc...) cause non-uniformity in the gain and phase responses of the system. The mechanical response of the piezos (and the viton ring) also play a role in the non-uniform responses to different input frequencies.

Custom filters have been introduced to cancel non-uniform responses. First, the response function to the input piezo voltage of the system was measured. To do this, the 894 nm and 866 nm lasers at the input of the fibre cavity in figure 7.2 are replaced with a 698 nm laser. On the output side, the dichroic mirror is lifted and the output beam directly coupled to APD 1 and the transmission signal studied on the oscilloscope. The FG is used to scan the piezos with a sinusoidal signal at different frequencies. The PI feedback is disengaged and there is no contribution from it to driving the piezos.

A 698 nm laser is chosen as it gives a cavity finesse of approximately 10. This finesse is large enough for the beam not to transmit straight through but low enough to stably stay at a side of the resonance peak and monitor the transmission response when the piezos are subjected to varying signals. The amplitude and phase of the cavity transmission signal is recorded for various drive frequencies of the piezo.

The cavity response whilst driving the monolayer and the multilayer piezos individually with sinusoidal signals (with and without the HVA) was recorded on the scope and the phase and amplitude information were extracted. The results are presented in figure 7.3. The plots show a resonant-antiresonant feature around 900 Hz and 9 kHz. They have a *derivative-like* profile in gain accompanying a sharp drop in phase.

These sharp changes must be accounted for to have a good quality of lock. For this a custom filters has been built to compensate these changes. The filter consists of low-pass, band-pass and high-pass filters apportionately combined to cancel the non-uniform electrical response of the system (see Appendix D).

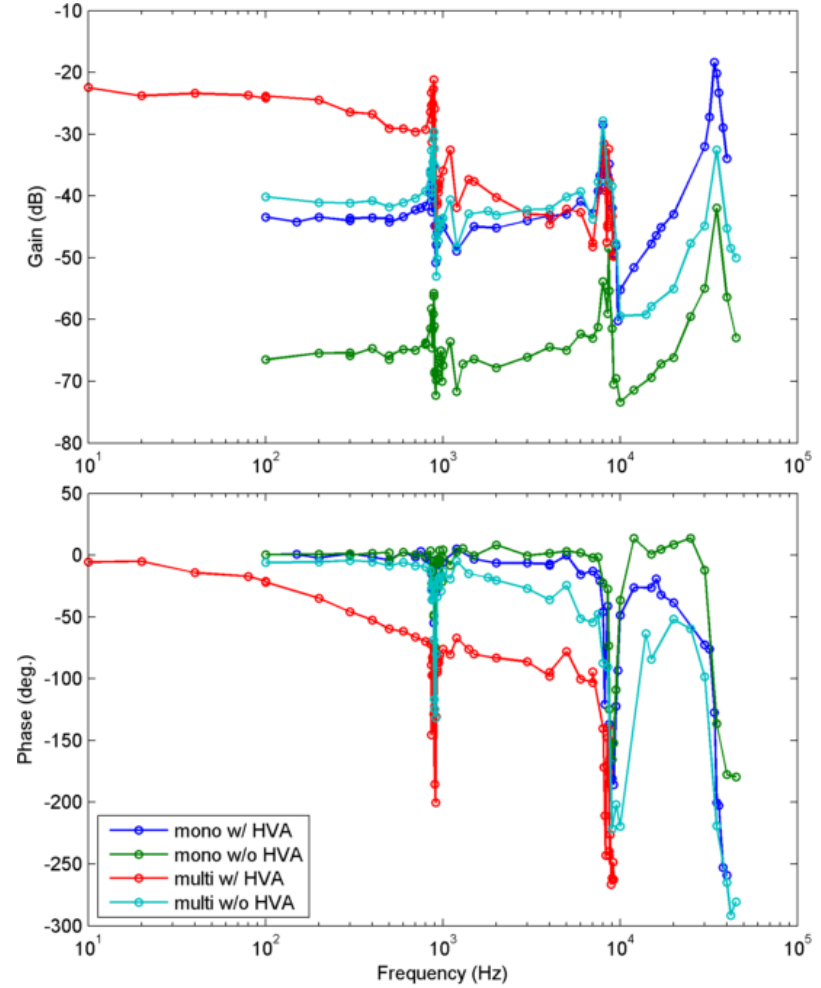


Figure 7.3: The cavity transmission gain and phase responses to input frequencies when driving (i) the monolayer piezo with the HVA in the circuit (blue), (ii) the monolayer piezo without the HVA (green), (iii) the multilayer piezo with the HVA (red) and (iv) the multilayer piezo without the HVA (cyan).

### 7.5.2 Quality of lock

The cavity is locked using the multilayer piezo. Since it is possible to lock the cavity with just this piezo, the monolayer piezo sits idly. The cavity finesse with the 894 nm laser is  $\sim 20\,000$  giving a linewidth of 22 MHz. We refer as *quality of lock* the standard to which the cavity length is stabilised. To assess this, we use the standard deviation of the aforementioned error signal (used to lock the cavity) and infer the frequency stability of the lock. We find a stability of 1.71 MHz. This is narrower than the linewidth of the cavity using an 866 nm laser, 9.4 MHz (see (3.3)). Therefore, we can have a stable lock at the wavelength of the ion's transition of interest to us.

# Chapter 8

## Trapped ions

### 8.1 Trapping ions

As described in previous sections, to load ions, the oven is first fired by resistively heating it. This creates an atomic beam between the trapping electrodes. The ionisation lasers ionise atoms in this beam. The ions see the trapping pseudopotential and are immediately trapped at the trap centre. They will become visible on the EMCCD images as they fluoresce under the cooling and repumping lasers. Occasionally, depending on the trap voltages, multiple ions can get trapped. To isolate a single ion, it suffices to block the repump lasers momentarily. This shelves the ions in the metastable D states preventing them from being cooled. Consequently, they heat up until they have enough energy to escape the trapping potential. An image of a trapped ion is shown in Figure 8.1. The trap is operated at secular frequencies in the range  $2.5 \text{ MHz} \leq \omega_a/(2\pi) \leq 3.9 \text{ MHz}$  axially and in the range  $1.6 \text{ MHz} \leq \omega_r/(2\pi) \leq 2.1 \text{ MHz}$  radially.

### 8.2 Excess Micromotion Compensation

Excess micromotion is a motion synchronous to the trap ac field caused by the presence of stray static charges and/or phase differences between the ac field at the trapping electrodes. Stray charges are usually deposited around the trapping region during the ion loading process. A single function generator is usually used to drive the electrodes of ion traps as is the case in this experiment. The source of phase difference at the trapping electrodes thus simplifies to a mismatch in length of the transmission lines to the trapping electrodes.

Excess micromotion results in inefficient cooling and broadens the transitional frequencies of the ion. The ion temperature plays an important role in the coupling strength of the ion to the cavity as it determines the wave-packet localisation. One of the key reas-

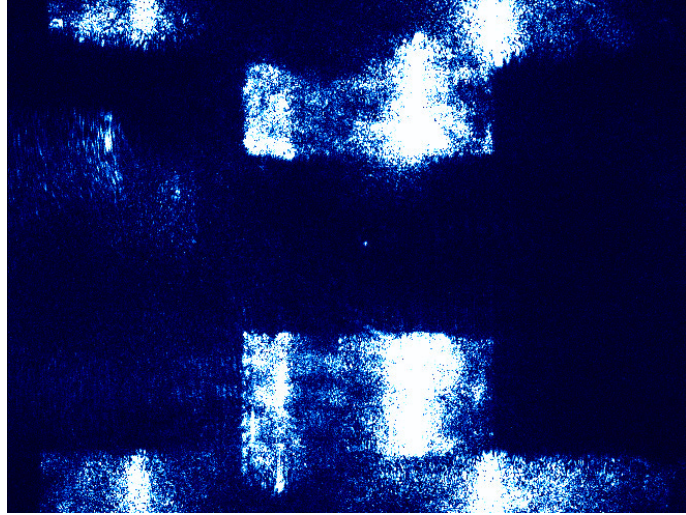


Figure 8.1: An EMCCD image of a single ion trapped at the trap centre. The inner and outer electrodes are visible.

ons we wish to minimise micromotion is in order to reduce the ion’s position wavefunction spread. Notably, we wish for the ion’s wavefunction spread to be small compared to the wavelength of the light field used in the cavity, 866 nm. This will allow us to map out the cavity’s standing wave pattern using the ion accurately and therefore be able to place the ion at an antinode of the cavity mode for optimal coupling.

In this section the ion’s equation of motion including the contributions from excess micromotion is defined. With this, we look at the techniques used to minimise excess micromotion.

### 8.2.1 Corrected equations of motion

I describe here the ion’s equation of motion including the contributions from excess micromotion. Recall from section 4.1.1 that the equation of motion for a single ion of mass  $m$  and positive charge  $e$  in a 3D Paul trap under potential  $\phi_0 = U_{dc} + V_{ac} \cos(\Omega t)$  is given by the Mathieu equation

$$\frac{d^2 u_i}{dt^2} + (a_i - 2q_i \cos(\Omega t)) \frac{\Omega^2}{4} = 0 \quad (8.1)$$

with  $i = \{r, z\}$  and

$$a_r = -\frac{1}{2}a_z = \frac{-8eU_{dc}}{m\Omega^2(r_0^2 + 2z_0^2)}, \quad (8.2)$$

$$q_r = -\frac{1}{2}q_z = \frac{4eV_{ac}}{m\Omega^2(r_0^2 + 2z_0^2)}. \quad (8.3)$$

where  $r_0$  and  $z_0$  are the respective distances to the ring and endcap electrodes from the trap centre.

The first order solution to the ion's equation of motion for the typical case of ( $|a_i|, |q_i| \ll 1$ ) is given in Equation 4.16.

In the presence of a static stray charge with field  $\mathbf{E}_{dc}$ , equation 8.1 becomes

$$\frac{d^2 u_i}{dt^2} + (a_i - 2q_i \cos(\Omega t)) \frac{\Omega^2}{4} = \frac{e\mathbf{E}_{dc} \hat{u}_i}{m}, \quad (8.4)$$

to which the solution to lowest order in  $a_i$  and  $q_i$  is [69]

$$u_i = [u_{0i} + u_{1i} \cos(\omega_i t + \psi_{1i})] \left[ 1 + \frac{q_i}{2} \cos(\Omega t) \right] \quad (8.5)$$

where

$$u_{0i} = \frac{4e\mathbf{E}_{dc} \cdot \hat{u}_i}{m(a_i + \frac{1}{2}q_i^2)\Omega^2} = \frac{e\mathbf{E}_{dc}}{m\omega_i^2} \hat{u}_i. \quad (8.6)$$

The excess micromotion here is the term  $u_{0i} \frac{q_i}{2} \cos(\Omega t)$ . The ion's average position in the presence of the static stray charge is  $u_{0i}$ .

In the presence of a phase difference,  $\psi_{ac}$ , between the trapping electrodes, the ion's equation of motion becomes[69]

$$u_i = [u_{0i} + u_{1i} \cos(\omega_i t + \psi_{1i})] \left[ 1 + \frac{q_i}{2} \cos(\Omega t) \right] - \frac{1}{4} q_i \alpha r_o \psi_{ac} \sin(\Omega t) \delta_{iz} \quad (8.7)$$

where alpha is a geometric factor and  $\delta_{iz}$  is the Kronecker delta function. We note that the equation of motion only changes in the axial direction by an additional oscillating term.

### 8.2.2 Coarse detection and compensation of excess micromotion

The paper [69] describes three methods of detecting micromotion. We employ two of the three methods discussed. The first, which we refer to as the open-and-close scheme, is used as a means of compensating micromotion coarsely. This scheme looks at the time averaged ion position as the trap pseudopotential amplitude is lowered and raised. The micromotion can be coarsely compensated using this technique. The second method, a more sensitive method, relies on detection of the fluorescence rate modulation induced by Doppler shift. We refer to this as the cross-correlation method. In this section we describe the open and close scheme.

#### Detection

As described in section 7.2, we have two EMCCD cameras to monitor the ion's average position in 3D. Equation (8.5) tell us that when no DC field is applied on the trapping electrodes, the ion's average position in the presence of a static field is shifted from the trap centre by

$$u_{0i} = \frac{4e\mathbf{E}_{dc} \cdot \hat{u}_i}{m \frac{1}{2} q_i^2 \Omega^2} \propto \frac{1}{V_{ac}^2}. \quad (8.8)$$

Thus, as we *open* the trap, that is as we lower  $V_{ac}$ , the ion's average position is shifted more from the trap centre than when the trap is closed (larger  $V_{ac}$ ). This shift in ion position is clearly detectable on the EMCCD images when there is a large micromotion.

To compensate the micromotion, we first close the trap and note the ion's position,  $\vec{p}$ , on the EMCCD images (see Figure 8.2a). Then we open the trap and note the movement of the ion in 3D (see Figure 8.2b). Subsequently we restore the ion's position back to  $\vec{p}$  by altering the voltages on the DC electrodes. We iterate these steps until the ion's position no longer changes when opening and closing the trap.

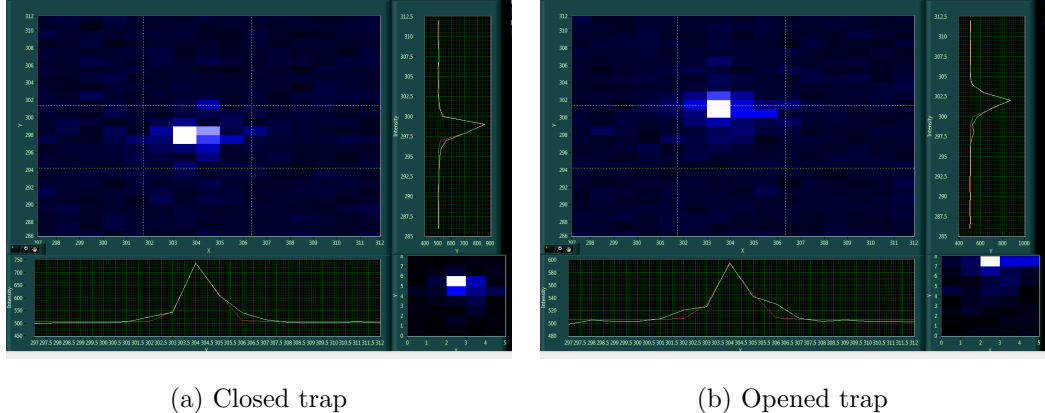


Figure 8.2: Zoomed in EMCCD images of the ion at two different trap depth. When the trap depth is large (a) the ion is close to the trap centre. The ion moves up from the trap centre when the trap depth is reduced (b). This indicates there's a stray E-field in pointing in the positive z direction. The images' data is averaged for a sub-pixel accuracy in determining the ion position.

The degree to which the excess micromotion is compensated using this method is limited by the resolution of the imaging optics. With the resolutions<sup>1</sup> we have, we cannot fully compensate the excess micromotion. As such, we complement this method with a follow-up technique having a finer ability to compensate micromotion. The description follows.

### 8.2.3 Fine detection and compensation of excess micromotion

#### Detection

With the rf correlation technique, the excess micromotion amplitude is gauged not from the EMCCD images but from the fluorescence rate detected by the PMT. Recall from equation (8.7) that the excess micromotion, be it from stray charges or phase difference

<sup>1</sup>Resolutions of 2.06  $\mu\text{m}/\text{pixel}$  and 2.23  $\mu\text{m}/\text{pixels}$  for the two EMCCD images.

in the trap electrodes, oscillates at the rf drive frequency,  $\Omega$ . As a result, in the frame of the ion, the cooling laser's frequency oscillates at the same frequency. To measure the amplitude of these oscillations, we look at the fluorescence signal from the ion. The arrival time of photons at the PMT is time binned in a period synchronous with the rf trap drive frequency by a multiple-event time-digitiser<sup>2</sup>. The excess micromotion is manifested as a modulation of the fluorescence signal as the ions sees a Doppler shifted light as it moves back and forth at the trap drive frequency. By reducing the amplitude of the modulation amplitude, one can minimise the excess micromotion.

We consider the case where  $\psi_{ac} \approx 0$ . We can say this is the case in our trap as we have built the transmission paths to the trapping electrodes to have the same length. The two paths use the same materials so they are expected to have the same impedance.

By sitting on the side of fringe of the ion's cooling transition spectrum, a linear response of the micromotion amplitude to the excess dc field can be observed. This is demonstrated here.

Let's consider a cooling beam with frequency  $\omega_l$  and wave vector  $\mathbf{k}$ . Let the ion's total motion,  $\mathbf{u}$ , be approximated by the superposition of the secular motion,  $\mathbf{u}_0$  and the excess micromotion,  $\mathbf{u}'$ . From (8.5), we find that

$$\mathbf{k} \cdot \mathbf{u}'(t) = \beta \cos(\Omega t) \quad (8.9)$$

where

$$\beta = \frac{1}{2} \sum_{i=x,y,z} k_i u_{0i} q_i. \quad (8.10)$$

The velocity of the ion due to excess micromotion is given by

$$\mathbf{v}' = \dot{\mathbf{u}}' = \frac{1}{2} \sum_{i=x,y,z} u_{0i} q_i \Omega \sin(\Omega t) \hat{\mathbf{u}}_i. \quad (8.11)$$

In the frame of an ion undergoing excess micromotion, the frequency of the laser is Doppler shifted by

$$-\mathbf{k} \cdot \mathbf{v}' = \beta \Omega \sin(\Omega t). \quad (8.12)$$

In the low intensity limit, the fluorescence rate is given by [69]

$$R_d = R_{max} \frac{\left(\frac{1}{2}\Gamma\right)^2}{\left(\frac{1}{2}\Gamma\right)^2 + [\omega_a - \omega_l - \beta \Omega \sin(\Omega t)]^2} \quad (8.13)$$

where  $R_{max}$  is the maximum fluorescence rate,  $\omega_a$  is the angular frequency of the atomic transition and  $\Gamma$  its line width. A natural choice for  $\omega_l$  is when  $\omega_l = \omega_a - \frac{\Gamma}{2}$  because this

---

<sup>2</sup>ACAM GP2 TDC, 65 ps bin size

maximises cooling efficiency by sitting at the steepest slope on the red detuned side of the fluorescence spectrum but also because it maximises the cross-correlation signal. Under this condition, we have

$$\frac{R_d}{R_{max}} = \frac{\left(\frac{1}{2}\Gamma\right)^2}{\left(\frac{1}{2}\Gamma\right)^2 + \left[\frac{\Gamma}{2} - \beta\Omega \sin(\Omega t)\right]^2}. \quad (8.14)$$

In the case where  $\beta\Omega \ll \Gamma$ , a justifiable assumption once micromotion has been coarsely compensated, we have

$$\frac{R_d}{R_{max}} \approx \frac{1}{2} + \frac{\beta\Omega}{\Gamma} \sin(\Omega t) \quad (8.15)$$

$$= \frac{1}{2} + \frac{\Delta R_d}{R_{max}} \sin(\Omega t) \quad (8.16)$$

where  $\Delta R_d$  is the amplitude of the oscillatory signal synchronous with the rf drive.

We note that

$$\Delta R_d \propto \beta$$

and

$$\beta = |\mathbf{k} \cdot \mathbf{u}'| \propto |\mathbf{k} \cdot \mathbf{E}_{dc}|$$

from equation (8.6). One can thus expect a linearity between the applied DC voltage on the electrodes and the ion's fluorescence modulation amplitude,  $\Delta R_d$ .

### Compensation method

To finely compensate the micromotion in three dimensions and place the ion at the rf minimum position, three cooling beams are employed. For each of the Doppler cooling beams there exists a plane in 3D voltage space where the *measured* micromotion is minimum. Whilst the micromotion amplitude is  $\sim 0$  on this plane for the selected beam, it will be vastly different for a second beam that probes the Doppler shift in a different direction. Likewise for the third beam. The intersection between these planes is the point of micromotion minimum. This is explained in detail here.

The trapping E-field of an endcap trap at a position  $\vec{x}$  is given by (4.2)

$$\vec{E}(\vec{x}) = \alpha(x, y, -2z) \quad (8.17)$$

where  $(x, y, -2z)$  is a vector and  $\alpha$  is some constant. Suppose now that a Doppler cooling beam is pointing along the direction  $\vec{l} = (l_1, l_2, l_3)$ . The micromotion amplitude seen by this laser is minimised on a plane satisfying the following relation:

$$\vec{E}(\vec{x}) \cdot \vec{l} = 0, \quad (8.18)$$

When the driven motion of the ion is along the direction of  $\vec{E}(\vec{x})$ . This is rewritten

$$l_1x + l_2y - 2l_3y = 0 \quad (8.19)$$

or

$$\vec{x} \cdot \vec{n} = 0 \quad (8.20)$$

where  $\vec{n} = (l_1, l_2, -2l_3)$ .

There are two orthogonal DC electrodes in the trap's radial plane, side electrode 1 and side electrode 2. Voltages  $u$  (on side electrode 1) and  $v$  (on side electrode 2) move the ion in the  $\hat{\mathbf{u}}$  and  $\hat{\mathbf{v}}$  directions respectively. DC voltages  $\frac{w}{2}$  and  $-\frac{w}{2}$  are superposed on the upper and lower rf-ground electrodes respectively such the ion sees a differential voltage of  $w$  moving it in the direction  $\hat{\mathbf{w}}$ .

Thus, the ion's position is given by

$$\vec{x} = A_u(u - u_0)\hat{\mathbf{u}} + A_v(v - v_0)\hat{\mathbf{v}} + A_w(w - w_0)\hat{\mathbf{w}}$$

where  $A_u$ ,  $A_v$  and  $A_w$  are some amplification factors and  $u_0$ ,  $v_0$ ,  $w_0$  are representing residual static voltage contributions that need to be compensated. Substituting  $\vec{x}$  to equation (8.20) gives the plane of micromotion minimum as

$$A_u(u - u_0)\hat{\mathbf{u}} \cdot \vec{n} + A_v(v - v_0)\hat{\mathbf{v}} \cdot \vec{n} + A_w(w - w_0)\hat{\mathbf{w}} \cdot \vec{n} = 0. \quad (8.21)$$

This plane's normal vector in  $uvw$ -space is given by

$$(A_u\hat{\mathbf{u}} \cdot \vec{n}, A_v\hat{\mathbf{v}} \cdot \vec{n}, A_w\hat{\mathbf{w}} \cdot \vec{n}). \quad (8.22)$$

It's key to make the following observations from the micromotion minimum plane given by equation (8.21) and its normal vector. As the number of stray charges, their positions in the trap and thus their contribution to the DC dynamics varies,  $(u_0, v_0, w_0)$  change causing also the absolute position of micromotion minimum plane to change. On the other hand however, despite these changes, the vector normal to the micromotion minimum plane (8.22) remains fixed as long as the amplification factors, the electrode configurations and the direction of the lasers are not altered.

### Finding the normal to the micromotion planes

To find the vector normal to the micromotion minimum plane for a given beam, one first need to find the plane. To do so, one starts from an arbitrary  $\vec{V}_0 = (u, v, w)$  value on the

DC electrodes and scans the voltage space in a chosen fixed direction<sup>3</sup>,  $\hat{\mathbf{n}}_i$ , to find the micromotion minimum position for this scan,  $\vec{V}_{min} = \vec{V}_0 + \alpha\hat{\mathbf{n}}_i$ , where  $\alpha$  is a constant. This procedure is illustrated in Figure 8.3. The scan in the same direction is repeated for at least two more starting voltages  $\vec{V}_0$  to obtain different micromotion minimum positions on the plane. Once one has three or more data points belonging to the micromotion minimum planes, one can fit a plane equation to them and extract the normal to the micromotion minimum plane. Using this methods, the micromotion minimum planes for each Doppler cooling beam have been measured and are presented in Figure 8.4.

### Automation of micromotion compensation

Finding the micromotion minimum planes for each beam and then finding their intersection each time we wish to compensate micromotion is a time consuming procedure. Instead we use the following scheme for a speedy and automated procedure.

Once the normal vectors to the micromotion minimum planes have been found for all the beams, one can follow the following 3-step procedure to find the global micromotion minimum position. I stress that the following is discussed in the voltage space and not in the real space.

Let us call  $n_1$  and  $n_2$  the normal vectors to the respective micromotion minimum planes,  $P_1$ , of beam 1 and  $P_2$  of beam 2. First we use beam 1 only and scan the voltage along direction  $d_1$  which is parallel to  $n_1$  until we find the micromotion minimum position. We are now sitting on plane  $P_1$ . We now wish to remain on this plane while we search for the micromotion minimum plane for beam 2. The intersection between planes  $P_1$  and  $P_2$  is a line which we shall call  $\mathbf{L}$ .  $\mathbf{L}$  lies on both planes which implies

$$\mathbf{L} \parallel \vec{n}_1 \times \vec{n}_2 \quad (8.23)$$

since  $\mathbf{L} \perp \vec{n}_1$  and  $\mathbf{L} \perp \vec{n}_2$ . The next step is therefore to move in the direction,  $\vec{d}_2$ , satisfying both

$$\vec{d}_2 \perp \vec{n}_1 \quad \text{and} \quad (8.24)$$

$$\vec{d}_2 \perp \mathbf{L}. \quad (8.25)$$

From equations (8.25) and (8.23), we get

$$\vec{d}_2 \perp \vec{n}_1 \times \vec{n}_2. \quad (8.26)$$

---

<sup>3</sup>the choice of this direction should reflect an intelligent guess of the expected normal vector the micromotion minimum planes, lest it ends up being parallel to the plane.

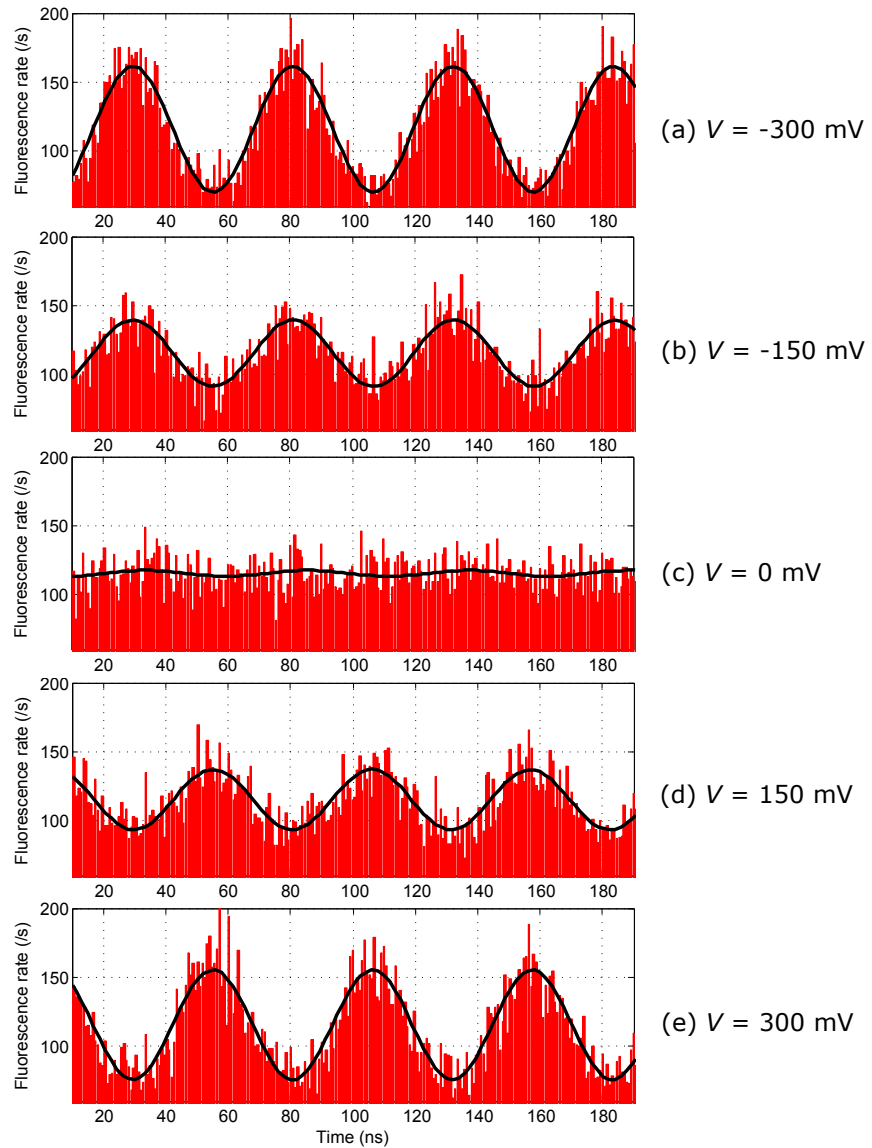


Figure 8.3: Fine micromotion compensation using fluorescence modulation. The red bars are the time-binned fluorescence count rates. The black curve is a sine fit to the data. The DC voltage  $V$  is scanned in a chosen direction from (a) -300 mV to (b) 300 mV in steps of 150 mV. We see the micromotion falling to near zero and rising back with a flipped phase.

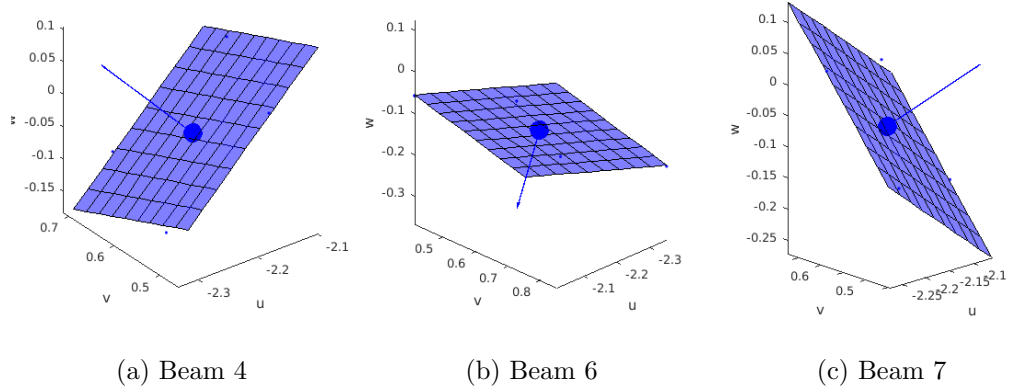


Figure 8.4: The planes of micromotion minimum in  $(u, w, w)$  voltage space for each Doppler cooling beam. The small blue dots are measured micromotion minimum positions. A plane is subsequently fitted. The large blue dot is a point on the plane from which position an arrow indicate the vector normal to the plane.

From (8.24) and (8.26), one obtains

$$\vec{d}_2 \parallel \vec{n}_1 \times (\vec{n}_1 \times \vec{n}_2). \quad (8.27)$$

Thus, in this step, beam 2 should be used whilst scanning the voltage in direction  $d_2$  to find a micromotion minimum position lying in both planes  $P_1$  and  $P_2$ .

In the third step, it suffices to use beam 3 whilst scanning in the direction  $d_3 \parallel \mathbf{L}$  to find the point along line  $\mathbf{L}$  which intercepts the micromotion minimum plane of beam 3. This point gives the global micromotion minimum point.

In summary, the three steps to be taken are

1. using beam 1 only find the micromotion minimum position along the direction  $\vec{d}_1 \parallel \vec{n}_1$  to sit on plane  $P_1$
2. using beam 2 only find the micromotion minimum position along the direction  $\vec{d}_2 \parallel \vec{n}_1 \times (\vec{n}_1 \times \vec{n}_2)$  to sit on the intersecting line  $\mathbf{L}$  of planes  $P_1$  and  $P_2$ .
3. using beam 3 only find the intersection point of all three planes by scanning along  $d_3 \parallel \vec{n}_1 \times \vec{n}_2$  (along  $\mathbf{L}$ ) to find the global micromotion minimum point.

#### 8.2.4 Phase difference treatment

In section 8.2.3 we assumed that there is no phase difference between the trapping electrodes and derived an expression describing how the detected fluorescence rate is affected by the excess micromotion (equation (8.15)). We saw that the fluorescence rate oscillates

synchronously with the rf signal and that there is no dependence of its phase on the excess micromotion amplitude. Here, we look at the case where there is a non-zero phase difference,  $\psi_{ac}$  between the rf signals at the two trap electrodes.

We consider again a cooling beam with frequency  $\omega_l$  and wave vector  $\mathbf{k}$ . Recall,  $\mathbf{u}$  is the ion's total motion and is approximated to be the superposition of the secular motion,  $\mathbf{u}_0$  and the excess micromotion,  $\mathbf{u}'$ .

From (8.7), we find that

$$\mathbf{k} \cdot \mathbf{u}'(t) = \frac{1}{2} \sum_i k_i u_{0i} q_i \cos(\Omega t) - \frac{1}{4} k_z \alpha r_0 \psi_{ac} \sin(\Omega t). \quad (8.28)$$

We redefine this as a single term

$$\mathbf{k} \cdot \mathbf{u}'(t) := \beta \cos(\Omega t + \delta) \quad (8.29)$$

and find from the sum to product rule

$$\beta \cos \delta = \frac{1}{2} \sum_i k_i u_{0i} q_i, \quad (8.30)$$

$$\beta \sin \delta = \frac{1}{4} k_z \alpha r_0 \psi_{ac} \quad (8.31)$$

with

$$\beta = \sqrt{\left( \frac{1}{2} \sum_{i=x,y,z} k_i u_{0i} q_i \right)^2 + \left( \frac{1}{4} k_z q_z r_0 \alpha \psi_{ac} \right)^2}. \quad (8.32)$$

In the frame of an ion undergoing excess micromotion, the frequency of the laser is now Doppler shifted by

$$-\mathbf{k} \cdot \mathbf{v}' = \beta \Omega \sin(\Omega t + \delta). \quad (8.33)$$

Thus, when there is a phase difference between the electrodes, the detected fluorescence rate, eq. (8.15), becomes

$$\frac{R_d}{R_{max}} \cong \frac{1}{2} + \frac{\beta \Omega}{\Gamma} \sin(\Omega t + \delta) \quad (8.34)$$

$$= \frac{1}{2} + \frac{\Delta R_d}{R_{max}} \sin(\Omega t + \delta). \quad (8.35)$$

We note that there is a phase dependent on the excess micromotion contributions both from static stray charges as well as from a phase difference in the rf signals at the trapping electrodes. Equations (8.29) and (8.33) can be thought of as a phasors with angle  $\delta$  between excess micromotion amplitude due to stray charges on the x-axis and the excess micromotion due to a rf phase difference on the y-axis. Thus, if there is a phase difference,  $\psi_{ac}$ , between the electrodes,  $\delta$  is expected to change significantly as the excess micromotion

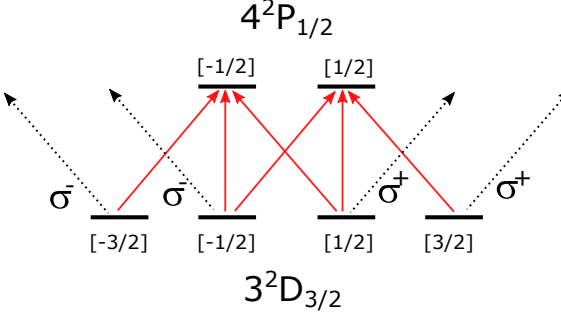


Figure 8.5: The Zeeman manifold on the 866 nm transition. The  $m_J$  quantum numbers are given in square brackets.

due to static stray charges is being compensated. As  $\delta$  changes, we would expect the phase of the rf-correlated fluorescence rate to change.

It is confirmed from the experiment that the phase of the fitted rf correlated fluorescence data does not change when the DC voltages are scanned (aside from a phase flip when we cross the plane of micromotion minimum).

### 8.3 Stray magnetic field compensation

To define the ion's quantisation axis we first need to compensate the stray magnetic field and then apply a well defined magnetic field. Current is applied to the coils on the chamber to apply an arbitrary magnetic field at the ion's position. To compensate the stray magnetic field, we use the ground state Hanle effect [70]. The method is described here.

Let's consider the transitions between the magnetic sublevels in the  $P_{1/2}$  and  $D_{3/2}$  states of  $^{40}\text{Ca}^+$  as depicted in figure 8.5. The dark state  $|\Psi\rangle$  is a superposition of the  $D_{3/2}$  sublevels uncoupled to the repumper, which is formally described as

$$\left( \sum_{m=-1/2}^{m=1/2} \sum_{m'=-3/2}^{m'=3/2} \hbar \Omega_{m,m'} |P_{1/2,m}\rangle \langle D_{3/2,m'}| \right) |\Psi\rangle = 0, \quad (8.36)$$

where  $\Omega_{m,m'}$  denotes the Rabi frequency between the Zeeman sublevels  $P_{1/2}$  and  $D_{3/2}$  states.

When the repumper only has a  $\sigma+$  polarisation, it is obvious from Figure 8.5 that  $|D_{3/2,1/2}\rangle$  and  $|D_{3/2,3/2}\rangle$  will be uncoupled dark states. Likewise, when the repumper is  $\sigma-$  polarised,  $|D_{3/2,-1/2}\rangle$  and  $|D_{3/2,-3/2}\rangle$  are the dark states. And when it's  $\pi$  polarised, the dark states are  $|D_{3/2,\pm 3/2}\rangle$ .

Because any polarisation of light can be viewed as a superposition of the  $\sigma+$ ,  $\sigma-$  and  $\pi$  polarisations, the dark state for an arbitrary polarisation will be a superposition of the

corresponding  $D_{3/2}$  sublevels. In other words, there is always a dark state being a certain superposition of  $D_{3/2}$  sublevels for an arbitrarily polarised repumper - as long as there is no magnetic field.

The magnetic field leads to a shift depending on the magnetic quantum number of the sublevels. This leads to a different time dependence of the individual sublevels. Thus, even if we have an uncoupled superposition state fulfilling the equation (8.36) at time  $t = 0$ , this superposition will be destroyed due to the different time-dependent phase factors of the constituent states. This destabilization of the dark states by a magnetic field is called the ground-state Hanle effect.

Note that the ground-state Hanle effect only occurs when the laser is composed of different multiple polarisations. When the repumper has a pure polarisation, i.e.  $\sigma+$ ,  $\sigma-$  or  $\pi$ , the dark state consists of a single Zeeman sublevel and hence its own time-dependent global phase is of no relevance for fulfilling the condition (8.36). Let's consider the case where we employ a linearly polarised repumper to probe the magnetic field. As we have seen, there is no dark state unless the repumper is  $\pi$ -polarised, i.e. its polarisation coincides with the direction of the magnetic field. In other words, when we observe the emergence of the dark state, the magnetic field should be aligned to the repumper polarisation and its components perpendicular to the repumper polarisation have been nullified. Therefore the full procedure to null the stray magnetic field would be as follows.

1. Fix the repumper polarisation in a certain direction, say  $x'$ <sup>4</sup> (referring to the coordinate system given in Figure 7.1).
2. Scan the magnetic field components in 2D, on the plane perpendicular to the repumper polarisation ( $y'z'$  plane), to find the fluorescence minimum.
3. At this fluorescence minimum, the magnetic field only has a component parallel to the repumper polarisation, aligned to the  $x'$ -direction.
4. Rotate the repumper polarisation by 90 degrees, for example to  $z'$ -direction. Now the repumper polarisation is perpendicular to the magnetic field.
5. Scan the magnetic field along the  $x'$ -direction. Because the magnetic field and repumper polarisation are guaranteed to be perpendicular to each other, at the fluorescence minimum the magnetic field is fully nullified.

---

<sup>4</sup>A primed coordinate system is used for the magnetic field to differentiate it from the coordinate system used to define the side electrode positions.

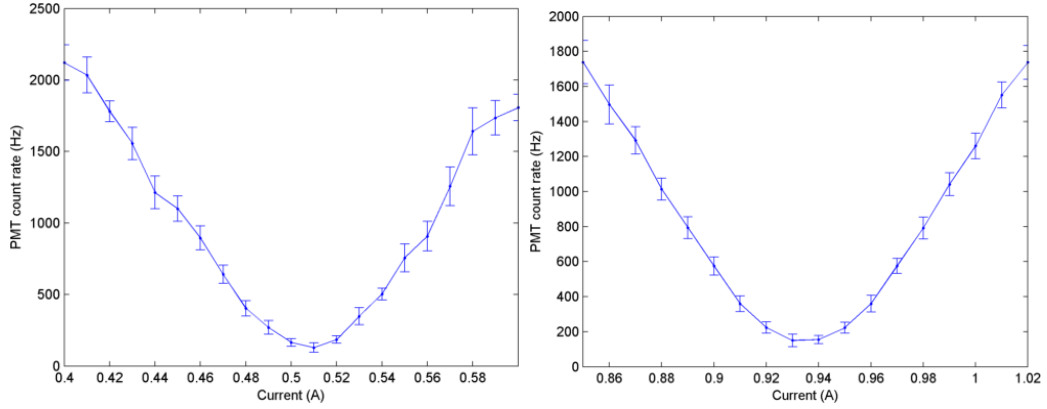


Figure 8.6: A scan of the current for the coils in the  $x'$  (left) and  $y'$  (right) directions. A dip in fluorescence is seen when the magnetic field is compensated in the subjected direction. The error bars are statistical errors from 20 measurements.

Following the procedure above, the currents supplied to the coils were scanned and the ion fluorescence rate recorded. The results are shown in Figures 8.6 and 8.7. Figure 8.6 shows the currents required in the coils for compensating the  $x'$  and  $y'$  components of the stray field. Figure 8.7 shows the fluorescence rate for a wider range scan of the magnetic field. A sharp Hanle dip is seen when the stray magnetic field is completely compensated.

As can be seen from Figure 8.6, a large current is required to generate the magnetic fields necessary to compensate the stray field. 510 mA is required for the  $x'$  direction coils and 935 mA for the  $y'$  direction one. These correspond to respective stray magnetic fields magnitudes of  $\sim 3.0$  G and  $\sim 5.6$  G<sup>5</sup>. For compensating the stray field in the  $z$  direction, a current of 42 mA (corresponding to 0.5 G) is needed. The large stray magnetic field is a result of the electrodes used in the trap being (unexpectedly) magnetic. This information only transpired in the wake of the investigation of the stray magnetic field in the ion trap.

The required currents to compensate the stray magnetic field in the  $x'$ ,  $y'$  and  $z'$  directions correspond to powers of close to 4 W, 14 W and 15 mW respectively being dissipated by the coils. We note that the large dissipated power can hamper the stability of the cavity as it is very sensitive to temperature fluctuations. This has not been observed for this experimental set-up but gathered from neighbouring experiments.

---

<sup>5</sup>These are estimations based on calibration measurements of the coils carried out with Hall effect sensors.

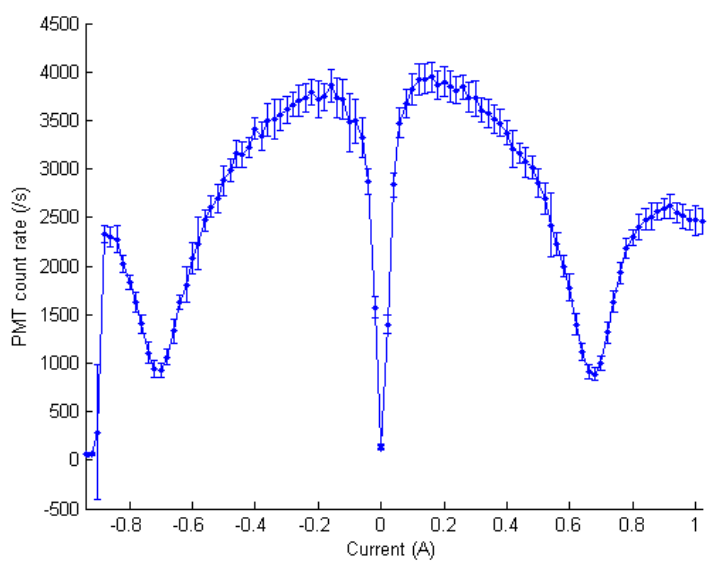


Figure 8.7: A scan of the current for the coils in the z direction. A Hanle dip is seen in the centre of the spectrum. The dips on either side of it, at approximately  $\pm 0.7\text{A}$  are from two-photon resonances (Raman excitations from the  $S_{1/2}$  level to the  $D_{3/2}$  level.). The fall in fluorescence near  $-0.9\text{ A}$  is due to the ion falling out of the trap at the end of the scan. The error bars are statistical errors from 20 measurements.

# Chapter 9

## Ion-cavity coupling

This chapter looks at the ion cavity coupling and presents the results. From the analysis of the alignment of the cavity and the trapping electrode assemblies in Section 5.2, we expected to have coupling between the trapped ions and the cavity without the need to change the ion-cavity overlap. To check this, the cavity was locked to the 866 nm transition with the method described in Section 7.5. To avoid large Stark shifts the 866 nm laser power injected into the cavity was reduced to a sub nW level. With this, it suffices to block all the free space repumpers to check for cavity coupling. If there is coupling, the ion will get repumped from the dark  $3^2D_{3/2}$  state by the 866 nm cavity field. Otherwise, fluorescence will not be seen. It was indeed the case that the ion and cavity were coupled as we could see the ion fluorescing without any free-space repumpers. See Figure 9.1 for the first image demonstrating the ion-cavity coupling.

Following this, we look at the optimisation procedure of the radial ion-cavity coupling. We demonstrate this for one radial direction. A system has been designed for the axial optimisation but has not yet been implemented. This design will be discussed. We have measured the coupling strength with the unoptimised ion-cavity overlap. Furthermore, we demonstrate anti-correlation between the UV fluorescence and the cavity emission due to the Purcell effect.

### 9.1 Radial coupling optimisation method

For radial optimisation of the ion-cavity coupling, we move the ion radially by applying an rf signal to the side electrodes as discussed in Section 4.4. Not detailed in the simulations of Section 4.4 is the method with which side rf is applied. Ideally, one would apply an rf voltage to the side electrodes in much the same way rf is applied to the main trapping

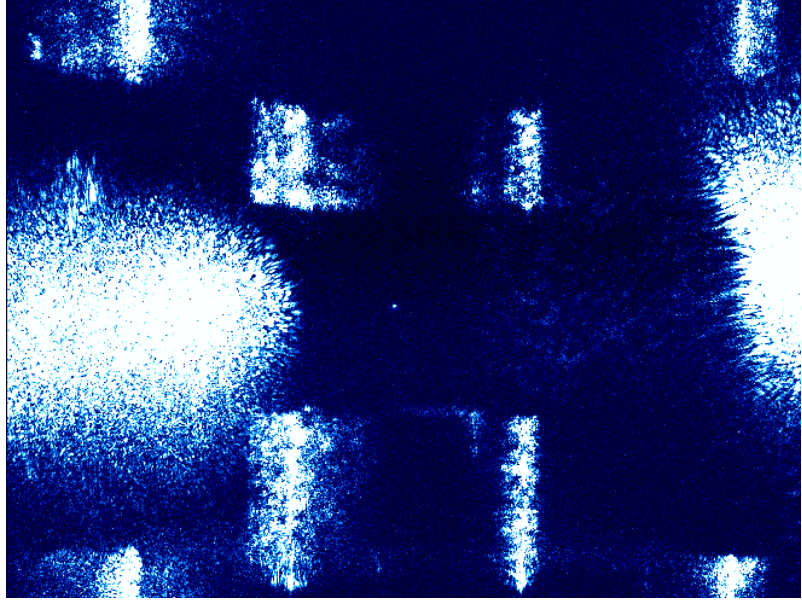


Figure 9.1: EMCCD image of a trapped ion being repumped by the cavity field. The ion is at the centre between the cylindrical electrodes. Here, no free space repumpers are used. The signals in the centre left and the far right centre are scatters from the side electrodes.

electrodes. That is, one would use another resonator to supply the needed rf voltage at the correct frequency and phase. This is however not possible in our setup as a strong capacitive coupling exists between the trapping electrodes and the side electrodes.

As a result we have resorted to a brute force method where we apply an amplified rf signal directly to the side electrodes<sup>1</sup>. This is illustrated in Figure 9.2. Function generator 1 (FG1) supplies rf signal to *Amplifier 1*<sup>2</sup> whose output goes to the main trapping electrodes via the helical resonator. The output FG2 of a dual function generator (DFG) is sent to *Amplifier 2*<sup>3</sup> whose output is directly attached to one of the side rf electrodes. The output FG2 is duplicated in the second channel of the DFG, FG3<sup>4</sup>. FG1 and the DFG are clock-synchronised. The signal from the side electrode must be in phase with the main rf signal lest the ion experiences excess micromotion due to rf phase mismatch. The phase of the rf signal at the side electrode is altered by changing the output phase,  $\phi_2$ , of FG2. To find the correct phase setting on the DFG for a given amplitude output, we scan the phase and monitor the ion's position on the EMCCD image. The ion's displacement will be greatest when the side rf is completely in phase ( $0^\circ$ ) or out of phase ( $180^\circ$ ) with the main rf. This can also be gauged from the simulation results (Figure 4.9) by looking

---

<sup>1</sup>The principal drawback of this method is substantial signal reflections due to impedance mismatch.

<sup>2</sup>Mini-Circuits ZHL-f1-2W

<sup>3</sup>Mini-Circuits LZY-1

<sup>4</sup>This is to avoid splitting the rf output of FG2.

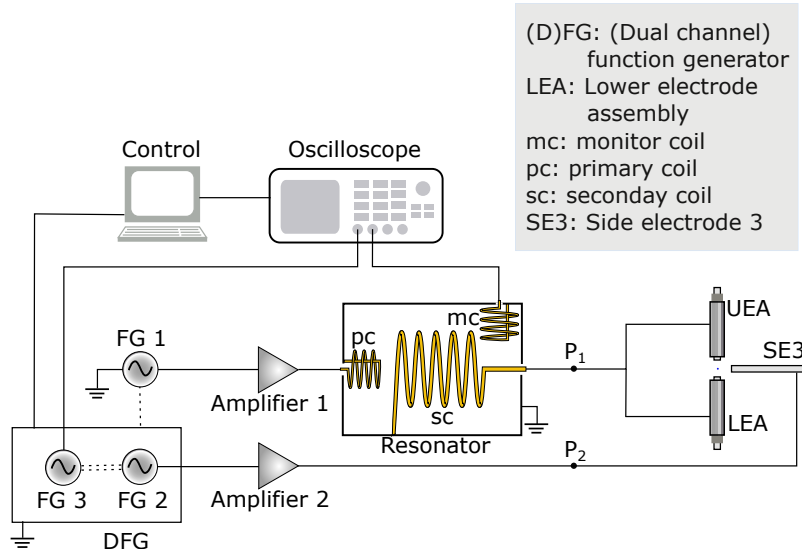


Figure 9.2: Schematic of the electrical setup for moving a trapped ion with the side rf electrodes. Function generator 1 is used to drive the main electrodes via an amplifier and a helical resonator. The channels of a dual function generator output identical signals. One is used to drive a side electrode via an amplifier. The second channel is monitored on an oscilloscope along with that of the monitor coil signal which picks up the signal at the helical resonator output. FG1 and the DFG are clock-synchronised. (The oscilloscope is triggered by the sync output of the DFG - not shown in the schematic.)

at the effects of a sign flip of the applied amplitude. The EMCCD image offers a good starting point for finding the necessary phase,  $\phi_2$ , for phase-matching; but the lower limit error on  $\phi_2$  is a few degrees due to the EMCCD's resolution. Therefore, we perform fine micromotion measurements (see section 8.2.3) for a phase range of a few degrees. By fitting and finding the micromotion minimum point, we reduced the error to  $\pm 0.5^\circ$ .

The required FG2 phase settings will vary for different amplitude settings because of a strong capacitive coupling between the electrodes in the trap. The capacitive coupling means that the voltage on the side electrode is composed of a contribution from the main rf signal in addition to the side rf signal. Likewise, the voltage on the main electrodes is comprised of a contribution from the side electrodes as well as from the main rf signal. For this reason, the monitor coil (mc) which picks up the signal at the helical resonator output (point  $P_1$ ) will be sensitive to the changes in the signal at the side electrodes. To keep the signal at the side rf in phase with that of the main rf as the voltages are changed translates to keeping the phase difference between  $P_1$  and  $P_2$  (see Fig. 9.2) constant. For this, the phase difference,  $\Delta\phi$ , between the the signals of FG2 and the mc is monitored

on an oscilloscope<sup>5</sup>.

When applying a signal on the side electrodes, if there is no phase difference between the side rf and the main rf as seen by the ion, the amplitude read at the mc will change but  $\Delta\phi$  will stay the same (apart from a  $180^\circ$  shift when the side rf amplitude is flipped). Hence, once the correct phase setting of FG2 is found by using the EMCCD image and the follow-up micromotion measurement for a given side rf amplitude, one should make a note of the target phase difference between the FG2 output and the mc signal,  $\Delta\phi_t$ . Then, when changing the side rf amplitude, in order to find the correct phase settings, it suffices to scan  $\phi_2$  until  $\Delta\phi = \Delta\phi_t$ .

Following the displacement of the ion using the procedure, the stray DC field,  $\mathbf{E}_{dc}$ , at the new ion position will be different. As such, the excess micromotion needs to be re-compensated. The ion's displacement with the side rf is illustrated in Figure 9.3. We plot the ion's displacement against the set side rf input amplitude of FG2 and find a linear relationship<sup>6</sup>. At each set side rf amplitude the excess micromotion was compensated and the required changes in the dc voltages recorded in Figure 9.4. As, expected, when the pseudopotential minimum moves in the  $y$  direction, only voltage  $u$  needs to be changed to compensate the excess micromotion.

---

<sup>5</sup>We do not compare to the phase of FG1 because it was empirically found that the phase difference between FG1 and the mc drifts (perhaps due to thermal drifts at the resonator).

<sup>6</sup>c.f. Figure 4.9; given the main rf voltage, we can use this slope to deduce the voltage on the side rf electrode.

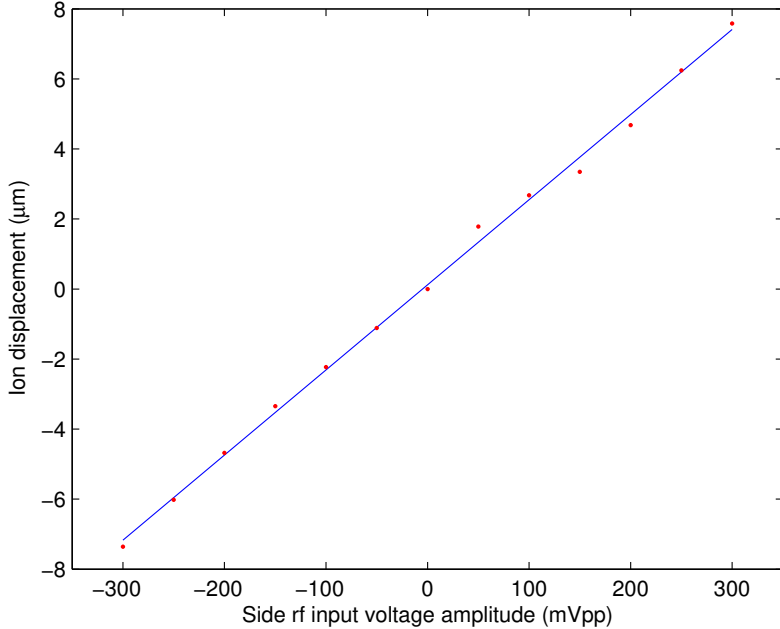


Figure 9.3: The ion displacement from the trap centre along  $\vec{y}$  vs the set input amplitude (DFG) when the rf is applied on side electrode 3. The red data points are recorded displacement from the EMCCD image. The data takes into account the angle between the EMCCD and the direction of ion displacement. The blue line is linear fit with a slope of  $2.43 \mu\text{m}/100 \text{ mVpp}$ .

## 9.2 Radial coupling optimisation

When the cavity field power is small, the cavity mode profile can be traced out by the fluorescence rate as the ion's position is scanned. To probe the cavity mode profile in the  $y$  direction, we move the ion with the method described above. For each ion position we lock the cavity<sup>7</sup> and measure the ion's fluorescence.

To successfully probe the cavity mode profile based on the ion's fluorescence, the power of 866 nm light in the cavity must not saturate the ion's repump transition and should be in a regime where the fluorescence rate is proportional to the repump power. This regime is achieved for injected 866 nm powers of sub-nW levels<sup>8</sup>. We reduce the power to these levels by using neutral density filters. As this input power is below the sensitivity of the photo-detector, it becomes difficult to reproduce the same power in the cavity field by monitoring the input power. A more direct method to gauge the power in the cavity is to

---

<sup>7</sup>The cavity does not stay locked as the side rf amplitude is changed. As we change the side rf voltage, thermal changes cause the cavity to drift. As such, we must unlock the cavity and wait for thermal equilibrium before relocking the cavity.

<sup>8</sup>As the 866 nm field power in the cavity is four orders of magnitude larger than the injected power.

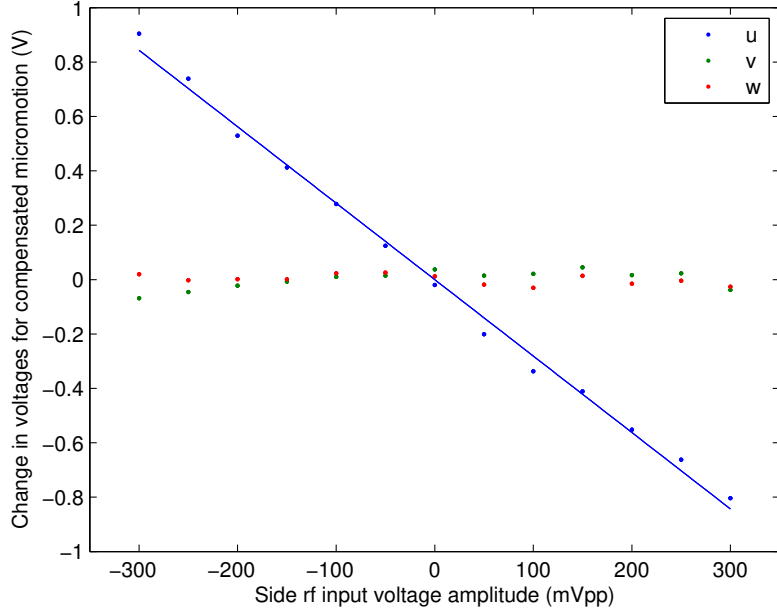


Figure 9.4: The necessary change in the dc compensation electrodes after moving the ion with side rf. The blue data points are the voltages for side electrode 1 ( $u$ ), the green for side electrode 2 ( $v$ ) and the red for the differential voltage on the main dc (inner) electrodes ( $w$ ). Little change is observed in the  $v$  and  $w$  voltages that move the ion respectively in the  $\vec{x}$  and  $\vec{z}$  directions. However,  $u$  changes with a slope of 0.28 V/100 mVpp.

look at the cavity output with an SPCM.

As shown in Figure 7.2, the cavity output is split into two branches: one branch of 894 nm for locking the cavity and a second branch of the 866 nm signal. Because this last branch has some residual 894 nm component, the 866 nm signal is further filtered out by bandpass filters. In addition, a neutral density filter<sup>9</sup> is used to attenuate the 866 nm signal. This is to prevent the SPCM from saturating. This SPCM reading is used for ensuring the 866 nm power in the cavity is the same.

### Fluorescence Detection

Ideally, the fluorescence would be detected using the free space PMT. However, due to the pinhole<sup>10</sup> the PMT only detects signal from a region at the trap centre with a radius of  $5 \mu\text{m}$  whilst we wish to move the ion by more than  $10 \mu\text{m}$ . Moving the PMT manually to follow the ion is impractical. For this reason, the fluorescence detection is done from the EMCCD image which offers a much larger coverage space albeit its poorer SNR. A region of interest (ROI) of  $6 \times 6 \text{ pix}^2$  is set around the ion and the count rate is gathered from the pixels in that area. As the ion moves, we programmatically move the region of

<sup>9</sup>Attenuation by a factor 1000.

<sup>10</sup>Necessary for a good SNR.

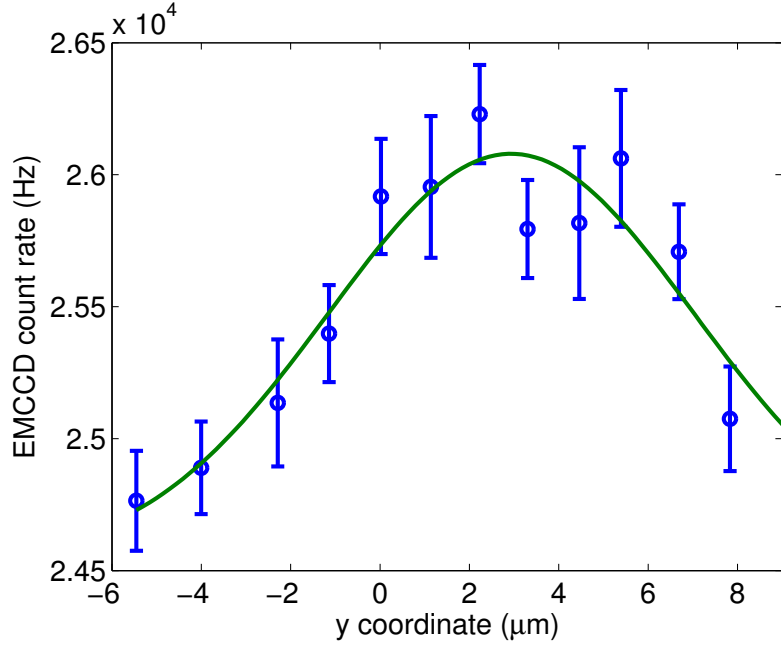


Figure 9.5: The ion’s fluorescence rate vs  $y$  coordinate when the ion is being repumped by a small power in the cavity field. A Gauss curve (green) is fitted to the data (blue). A wait of  $8.2 \pm 2.0 \mu\text{m}$  is deduced.

interest with it. With this method, we have measured the mode profile in the  $y$  direction. The result is presented in Figure 9.5. We see that the ion is trapped  $2.9 \mu\text{m}$  away from the cavity centre in the  $y$  direction. A Gaussian fit reveals the mode waist to be  $8.2 \pm 2.0 \mu\text{m}$  which is close to the waist of  $8.5 \mu\text{m}$  predicted in Section 3.2. This procedure is readily achievable in the  $x$  direction.

### 9.3 Purcell Effect - decay rates and suppression of fluorescence

The following is carried out without moving the ion with the side rf electrodes.

#### Decay rates

Through the Purcell effect we expect the ion’s spontaneous decay rate to the  $3^2D_{3/2}$ ,  $\gamma_D$ , to be enhanced when the cavity is locked. Here, we observe the Purcell effect by measuring the change in the decay rate,  $\gamma$ , in the  $4^2P_{1/2} \leftrightarrow 4^2S_{1/2}$  transition first when the cavity is unlocked, and then when the cavity is locked. For this, the cavity is locked using the same setup as in Figure 7.2 and the 866 nm laser is subsequently blocked. We repump the ion with the free space 850 nm and 854 nm beams. The cooling beam, beam 4, is used to pump the ion. For measuring  $\gamma$  we block the repumpers and record the arrival time of 397 nm photons at the free space PMT as the ion decays from the  $4^2P_{1/2}$

state to  $4^2S_{1/2}$  state before it gets *shelved* on the  $3^2D_{3/2}$  level. An rf-switch<sup>11</sup> is used to pulse the 850 and 854 repumpers between on and off<sup>12</sup> states at a rate of 50 kHz with a duty cycle of 50%. Beam 4 is kept on at all times. A multiple-event time digitiser<sup>13</sup> is used to time-bin the arrival of the 397 nm photons<sup>14</sup> immediately after the repumpers are switched off. We collect some few hundred thousands of photon arrival times to build up the statistics to allow us to determine the decay rate of the  $P_{1/2}$  state. This is presented in Figure 9.6, showing the fluorescence decay rate with and without the cavity locked. The parameters used are as follows: Beam 4 is horizontally polarised and has a detuning of -14 MHz. The stray B field is compensated and a field of -1.96 G is applied along the  $z$  direction. The cavity is locked with a detuning of -22 MHz. Exponential fits are used to find the decay-time constants. We find a decay time-constant of  $\tau_u = 730.1 \pm 20.7$  ns and  $\tau_l = 260.2 \pm 6.0$  ns when the cavity is unlocked and locked respectively. There are only two unknown parameters: The pump Rabi frequency<sup>15</sup>,  $\Omega_p$ , and the ion-cavity coupling,  $g_0$ . We use the rate equation of an 8-level model to find these parameters. See Figure 9.7. First we set  $g_0 = 0$  to simulate the case for the unlocked cavity. We sweep  $\Omega_p$  until the simulated decay constant matches  $\tau_u$ . We find  $\Omega_p = 2\pi \cdot 29.6$  MHz. Having found  $\Omega_p$  we then sweep the  $g_0$  parameter until the fitted decay-time constant matches  $\tau_l$ . We find  $g_0 = 2\pi \cdot 4.60 \pm 0.11$  MHz. This is the largest coupling strength reported to date for a single ion coupled to a cavity at an infrared transition. The cooperativity  $C = g_0^2/(2\kappa\gamma) = 0.20$  is the second largest reported for a single ion<sup>16</sup>.

---

<sup>11</sup>Mini-Circuits ZASWA2-50PR-FT+.

<sup>12</sup>The rf switch suppresses the signal to about -80 dBm.

<sup>13</sup>Fast ComTec MCS6A

<sup>14</sup>The delay of the time bin is marked by the difference in the arrival time of a photon (Start time) and the next edge in the rf-switch pulsing gate (Stop time).

<sup>15</sup>Unknown because the beam waist at the the ion is not known precisely.

<sup>16</sup> $C = 1.8$  is found in [71] (see [72] for computation) on the  $S \leftrightarrow D$  (effective two-level system) of  $^{40}\text{Ca}^+$  where magnetic field fluctuations and laser instabilities will obscure the ion-cavity coherence. Indeed, the authors state  $P \leftrightarrow D$  transitions are most attractive for an ion-photon interface. This comparatively large cooperativity can be predominantly attributed to the reported small cavity decay rate,  $\kappa = 2\pi \cdot 0.05$  MHz.

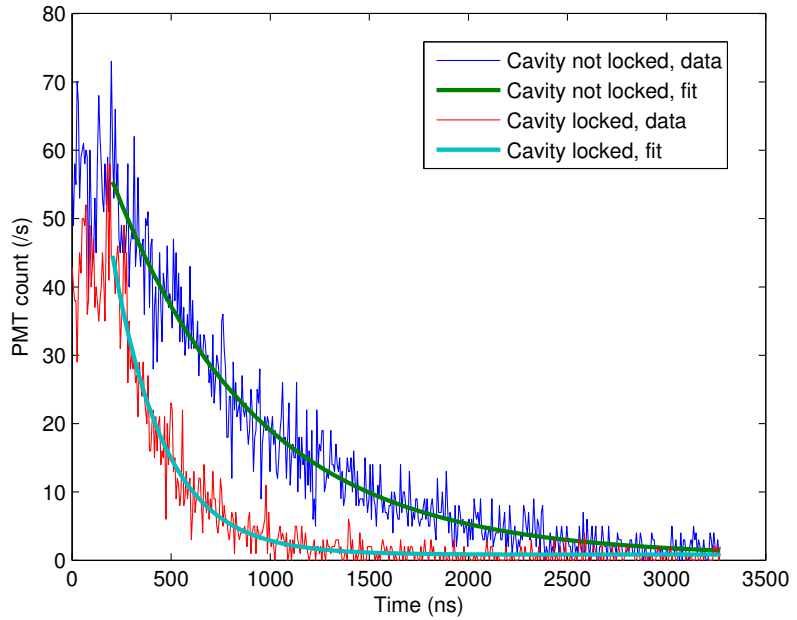


Figure 9.6: The decay rate of the uv fluorescence when the cavity is not locked (blue) and when the cavity is locked (red). The green line is an exponential fit to the data for the unlocked cavity and gives a time-constant  $\tau_u = 730.1 \pm 20.7$  ns. The cyan line is an exponential fit to the data for the locked cavity and gives a time-constant  $\tau_u = 260.2 \pm 6.0$  ns. The *flat* data in the first  $\sim 200$  ns is due to a delay in the AOM used to switch on and off the repumpers. A modified 866 nm decay rate means a different starting  $4^2P_{1/2}$  population at equilibrium hence the different starting levels in the blue and green traces.

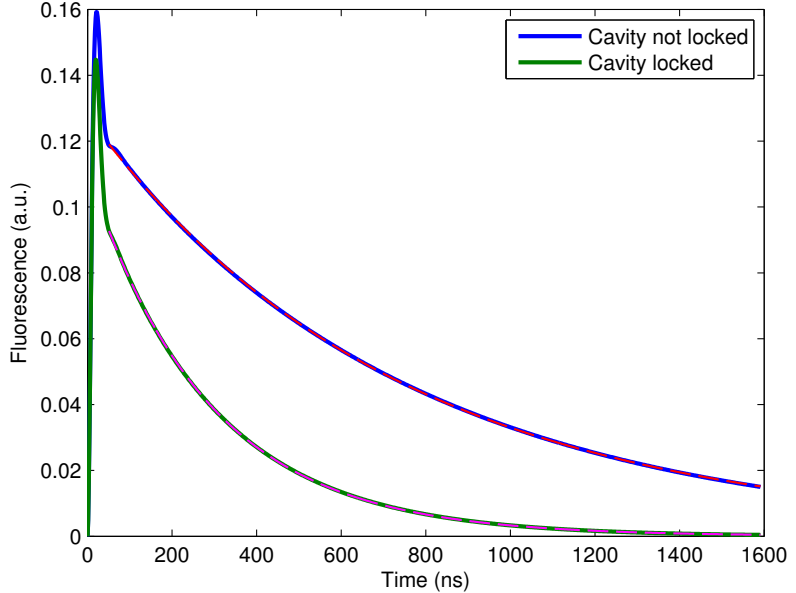


Figure 9.7: Numerical simulation of the fluorescence rate of the  $4^2P_{1/2} \leftrightarrow 4^2S_{1/2}$  transition using an 8-level model. In blue is the simulation for the unlocked cavity where  $g_0$  has been set to 0. The pump Rabi frequency  $\Omega_p$  is swept until the decay constant of the fitted curve (dashed red line) matches that of the experimentally data. Following this, the green curve is simulated using the found  $\Omega_p$  value. In this case,  $g_0$  is swept such that the decay rate of the fitted exponential curve (dashed magenta line) matches that of the experimental data. The large signals at  $t < 50$  ns are the onset of Rabi oscillations with the state initialised at  $4^2S_{1/2}$ . The decay constants are independent of the initial conditions and the region  $t < 50$  ns is omitted from the fits.

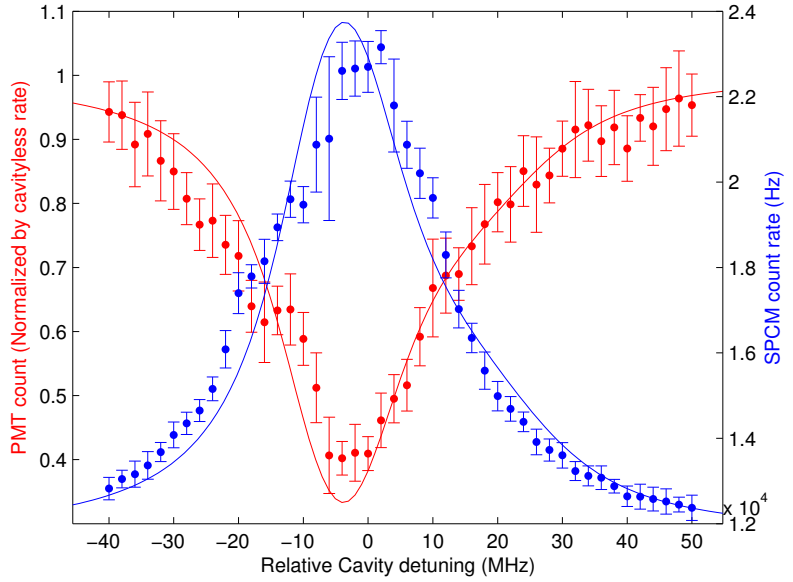


Figure 9.8: Anti-correlation in the fluorescence rate and the cavity emission rate as the cavity length is scanned. The data points in red are the uv fluorescence detected by the PMT. This rate is normalised to the fluorescence rate when the cavity is not locked. The data points in blue are the cavity emission rate detected by the SPCM. The error bars are statistical errors. The lines (respectively coloured) are theoretical curves from the eight-level atom model.

### Anticorrelation of fluorescence and cavity emission rates

As the decay rate in the  $4^2P_{1/2} \leftrightarrow 3^2D_{3/2}$  transition is enhanced by the cavity, the Purcell effect will also be manifested as an effective suppression of the fluorescence rate in the  $4^2P_{1/2} \leftrightarrow 4^2S_{1/2}$  transition. To see this anti-correlation, the cavity length was scanned with the method described in Section 7.5. The 866 nm beam going to the cavity is blocked and the ion is repumped by the free space repumping beams at 850 and 854 nm. The cavity emission is detected by the SPCM. Simultaneously, the ion fluorescence is collected by the free space PMT. The scan result is illustrated in Figure 9.8. We find that the fluorescence rate in the  $4^2P_{1/2} \leftrightarrow 4^2S_{1/2}$  transition is suppressed by up to 60%.

We compare this to the theoretical model discussed in Chapter 2.4. Having already got  $g$  from the preceding decay rate measurements, the missing parameters are the pump and repumper Rabi frequencies. To find the pump Rabi frequency, we repeat the procedure used in the decay rates measurement extending it to also measuring the de-shelving rate of the  $3^2D_{3/2}$  population. That is, we now additionally measure the 397 nm photon arrival time from the time the repumpers are switched on. Here, the rf-switch is used to pulse the 850 nm and 854 nm repumper beams between being on and off at a rate of 100 kHz with

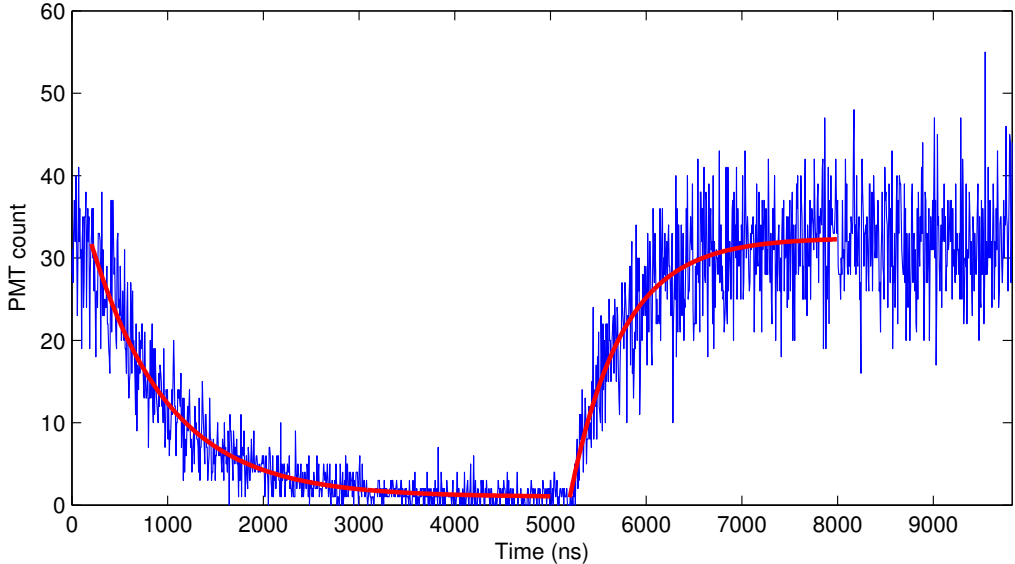


Figure 9.9: Shelving and de-shelving of the  $4^2D_{3/2}$  state. At  $t = 0$  the repumpers are blocked and the 397 nm photon arrival time collected until the ion is shelved in the  $4^2D_{3/2}$  manifold. The repumpers are switched on at  $t = 5\mu\text{s}$  and the 397 nm photon collected as the  $D$  state is depopulated. The data (blue) is fitted with exponential functions (red). Shelving rate  $\tau_s = 800$  ns and de-shelving rate  $\tau_d = 544$  ns are computed.

a duty cycle of 50%. For multiple repetitions (few hundred thousands) of these shelving and de-shelving events, we record the arrival times of UV photons at the PMT from the beginning of each cycle using the multiple-event time digitiser. By compiling the recorded arrival times, we can get a picture of the transient change of the ion's fluorescence rate as it is being shelved to and de-shelved from the  $3^2D_{3/2}$  state as presented in Figure 9.9. From the shelving part of the data (which is independent of the repumping dynamics) we extract the pump Rabi frequency. We find a lifetime of 800 ns. With numerical simulations, we find the Rabi frequency that gives this lifetime to be  $\Omega_p = 2\pi \cdot 32.2$  MHz.

We then use the pump Rabi frequency in the de-shelving part of the data to deduce the repumping efficiency. The repumping efficiency is found to  $\gamma_r = 2\pi \cdot 0.015$  MHz, giving the last of the unknown parameters.

With these, we simulate the scan of the cavity over a Raman resonance with an eight-level atom model as done in Chapter 2.4. Note that in the experiment, 393 nm photons of the  $4^2P_{3/2} \leftrightarrow 4^2S_{1/2}$  transition are also collected. These are modelled as a direct  $D \leftrightarrow S$  decays and are taken into account in the numerical simulation. The comparison to the data is also illustrated in Figure 9.8. Both the ion's UV fluorescence and the cavity emission are in good agreement with the theoretical model. However, the measured maximum

suppression of fluorescence rate falls short of the theoretical prediction. A Lorentzian<sup>17</sup> fit to the PMT count data gives a peak suppression of  $61 \pm 2\%$  of the cavity-less rate. We find agreement to within three error bars with the theoretical prediction of 66%. We attribute the reduction in the contrast to the ion's temperature and micromotion. This is notably because the cooling efficiency in the axial direction (also the cavity axis) is limited due to geometrical constraints. Some broadening of the Lorentzian-like data sets compared to the theory is also seen. This can be caused by high ion temperatures and/or poor cavity locking. The clear limitation in cooling in the axial direction point to the ion's temperature as the dominant cause for the broadening. Future work should aim to minimise the ion's temperature and incorporate the ion's wavefunction spread into the model.

---

<sup>17</sup>A good approximation to the dynamics. Note the asymmetry in the simulations of Chapter 2.4.

## Chapter 10

# Conclusion and Outlook

The main motivation of this work was to build an integrated ion-cavity system capable of reaching the strong coupling regime. This comprises the basic building block of a high-fidelity quantum network. To this goal a fibre cavity with finesse of  $F = 40,000$  and decay rate  $\kappa = 2\pi \cdot 4.7$  MHz has been tightly confined in the trapping electrodes of a Paul trap. The cavity length was set to  $380 \mu\text{m}$ .

The historical challenge in the integration of cavities and ion traps has been that the presence of dielectric mirror coatings distorts the rf potential and dramatically degrades trapping capabilities. By integrating and recessing the fibre cavities in the trapping electrodes, the detrimental effect of their presence has been diminished. With this design,  $^{40}\text{Ca}^+$  ions have been stably trapped for many hours. The excess micromotion and the stray B field in the system have been fully compensated.

With the aid of electrical filters to compensate resonances, the cavity has been stably locked with a standard deviation of 1.71 MHz. Using the system we have been able to demonstrate coupling between a high finesse FFPC and an ion. We report the highest finesse of a FFPC that has been coupled to an ion. The coupling has been observed immediately without the need to translate the ion owing to the great care that was taken to make the cavity concentric with the trapping electrodes during assembly.

To infer the coupling strength, a pulsed scheme was employed to measure the decay rate of the  $P_{1/2}$  state. The ion was prepared in the  $P_{1/2}$  state and the 397 nm photon arrival times recorded as the ion decayed. When there is coupling, the decay rate is expected to rise due to the Purcell effect. Comparison to numerical simulations gave a coupling strength of  $g = 2\pi \cdot 4.6$  MHz, the largest reported for an ion's infra-red transition. The ion-cavity coupling of  $g = 2\pi \cdot 67$  MHz reported in [39] is the only one exceeding the coupling strength reported here; however the fibre cavity in [39] operates on an UV

transition. Whilst this came with the benefit of using the large electric dipole strength,  $d$ , of the principal optical dipole transition of the trapped ionic species here (which lead to larger coupling strength since  $g \propto d$ ), the finesse of the fibre cavity is low and has been found to degrade dramatically in an ultra high vacuum condition by an unknown process.

Further, the Purcell effect was observed in the enhancement of cavity photon emissions by detecting the 866 nm photons whilst scanning the cavity length. In such a lambda system, anti-correlation in the emission rate of the two possible decay channels (here, the 397 nm and 866 nm photons) is expected but had not been shown to date. By simultaneously detecting the 397 nm photons, we have demonstrated an effective suppression in the emission rate of the  $P_{1/2} \leftrightarrow S_{1/2}$  transition by 60%. Suppression on a UV transition has been shown with Ytterbium ions in [39] with a cavity operating also on the UV transition. However, because the energy level scheme used is an effective two-level system, it is inherently not possible to demonstrate the anti-correlation of emission rates as shown in this work. In an earlier work [38] a cavity has been coupled to the IR branch of a lambda system. However the Doppler cooling was carried out on a UV transition outside of the lambda system; anti-correlation between emission rates has not been shown.

As it stands, the measured coupling strength is not yet in the strong coupling regime. The coupling strength,  $g$ , depends on the ion position in the cavity mode. It is optimal when the ion is at the centre of the mode and at an anti-node of the standing wave. With the current set-up the expected maximum coupling rate is  $g_0 = 2\pi \cdot 17.2$  MHz. After a correction by the Clebsch-Gordan coefficients for the Zeeman sub-levels, we expect  $g_0 = 2\pi \cdot 12.2$  MHz for the  $D_{3/2,\pm 3/2} \leftrightarrow P_{1/2,\pm 1/2}$  transitions. This places us in the strong coupling regime. Efforts to reach the strong coupling regime with ions coupled to a fibre cavity in [38, 39, 73] have been impeded by large cavity decay rates in contrast to the work presented here.

What remains to accomplish the strong coupling regime in this experiment is to position the ion optimally in the cavity mode. The trap has been equipped for this task. Additional *side*-electrodes have been added on which rf can be applied to shift the trapping potential minimum. With these, the ion can be moved radially. This operation was tested in one radial direction. We probed the cavity mode profile in said direction and measured a waist of  $8.2 \pm 2.0 \mu\text{m}$  in agreement with the expectations. For this measurement, the ion was repumped by a small power of 866 nm light injected into the locked cavity. We detected the 397 nm fluorescence as the ion's position was shifted by the additional electrode. Because of the small repumping laser power in the cavity, the detected fluorescence follows

the intensity profile of the cavity mode. We found we were  $2.9 \mu\text{m}$  away from the mode centre in this direction.

Time constraints have made the measurement of the optimal  $g_0$  beyond the scope of this thesis. However, there is confidence that the current system is capable of establishing strong coupling between a single ion and the cavity. Ions will be moved radially using the side rf electrodes to optimise the radial ion-cavity coupling. This time, for smaller systematical errors, to gauge the mode profile, the cavity emission will instead be detected as the ion is translated. To place the ion at an anti-node of the cavity standing-wave, the balance of the rf voltages on the main trapping electrodes will be scanned by using a capacitive potential dividers. Following this, Rabi splitting measurement will be carried out. We anticipate a Rabi splitting of  $2g = 2\pi \cdot 24.4 \text{ MHz}$ .

The experiment goes on...

*Publications related to this thesis*

- **Novel ion trap design with an integrated fibre cavity and a tunable ion-cavity coupling**, E. Kassa, H. Takahashi, C. Christoforou, M. Keller.  
Manuscript in preparation, June 2017
- **Cavity-induced anti-correlated photon emission rates of a single ion**, H. Takahashi, E. Kassa, C. Christoforou and M. Keller. Accepted and to be published by *Physical Review A*, June 2017. <https://arxiv.org/abs/1705.07923>
- **Novel laser machining of optical fibers for long cavities with low birefringence**, H. Takahashi, J. Morphew, F. Orucević, A. Noguchi, E. Kassa and M. Keller.  
*Optics Express*, **22**(25):31317-31328, December 2014. <http://www.opticsexpress.org/abstract.cfm?URI=oe-22-25-31317>

## Appendix A

### Calcium 40 ions

#### A.1 First ionisation of Calcium 40

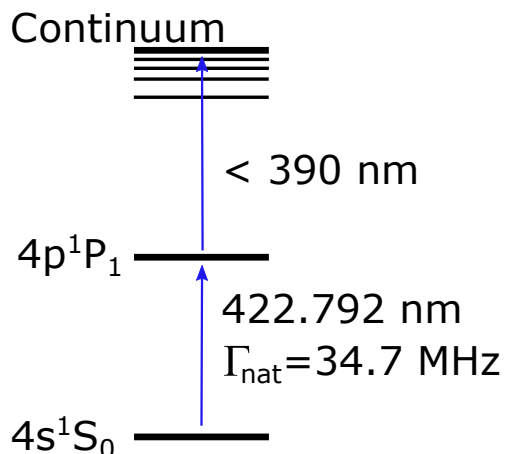


Figure A.1: Calcium 40 atom energy level diagram of relevant transitions used in the resonant two-photon ionisation process. The quoted wavelengths are as measured in vacuum.  $\Gamma_{\text{nat}}$  is the natural linewidth of the  $P_1$  state.

We employ an isotope selective two-step photoionisation process [63, 64] to ionise a flux of calcium 40 atoms to  ${}^{40}\text{Ca}^+$  ions. This method is five orders of magnitude more efficient than the conventional electron bombardment method [63]. This method results in less charging effects in the trapping region (due to the absence of electron bombardment) as well as a reduction of sputtered material from the atomic oven around the trapping region (owing to the higher ionisation efficiency). The resonant wavelength of the first ionisation laser is measured to be 422.792 nm in vacuum when the ionisation beam is perpendicular to the atomic flux (i.e. when the ionisation beam is not Doppler shifted in

Transition	Wavelength in vacuum (nm)	Linewidth ( $2\pi$ )	Branching ratio	Saturation intensity ( $\text{W/m}^2$ )
$4^2\text{S}_{1/2} \leftrightarrow 4^2\text{P}_{1/2}$	396.959	21.0 MHz	0.93565(7)	439
$3^2\text{D}_{3/2} \leftrightarrow 4^2\text{P}_{1/2}$	866.452	1.44 MHz	0.06435(7)	2.89
$4^2\text{S}_{1/2} \leftrightarrow 4^2\text{P}_{3/2}$	393.477	1.35 MHz	0.9347(3)	461
$3^2\text{D}_{3/2} \leftrightarrow 4^2\text{P}_{3/2}$	850.035	152 kHz	0.00661(4)	0.32
$3^2\text{D}_{5/2} \leftrightarrow 4^2\text{P}_{3/2}$	854.444	1.35 MHz	0.0587(2)	3.83
$4^2\text{S}_{1/2} \leftrightarrow 3^2\text{D}_{3/2}$	732.591	135 mHz	–	$2.25 \times 10^{-7}$
$4^2\text{S}_{1/2} \leftrightarrow 3^2\text{D}_{5/2}$	729.348	136 mHz	–	$2.30 \times 10^{-7}$

Table A.1: Relevant  ${}^{40}\text{Ca}^+$  transitions with natural linewidths, branching ratios and saturation intensities. See main text for more.

the atomic frame). It is sourced from a diode laser (Moglabs CEL002). The wavelength of the second ionisation beam we use is 375 nm and is also sourced from a diode laser (Nichia NDU1113E).

## A.2 ${}^{40}\text{Ca}^+$ Transitions

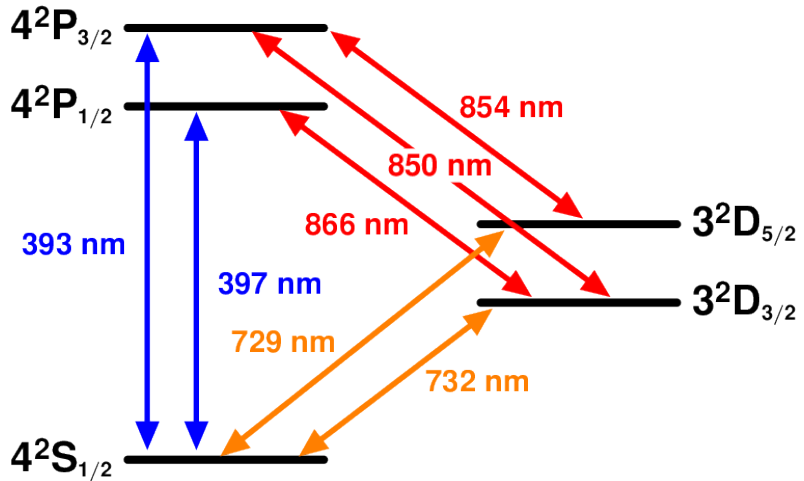


Figure A.2: Relevant  ${}^{40}\text{Ca}^+$  energy levels.

Jin and Church measured the lifetimes of the  $P_{1/2}$  and  $P_{3/2}$  states to be  $7.098 \pm 0.02$  ns and  $6.924 \pm 0.019$  ns respectively [74]. These figures are more precise than those reported previously in [75]. Later the branching fractions for the decays from the  $P_{1/2}$  and  $P_{3/2}$

	$^2S_{1/2}$	$^2P_{1/2}$	$^2P_{3/2}$	$^2D_{3/2}$	$^2D_{5/2}$
$g_J$	2	2/3	4/3	4/5	6/5

Table A.2: The Landé g-factor of relevant transitions

states were measured with great precision using trapped single ions in [76] and [77] respectively as quoted in Table A.1. Combined with the aforementioned lifetimes, the linewidth of each transition can be deduced as listed in the table. On the other hand, in his paper [78], James quoted different values for the decay rates. He uses the lifetime measurements in [75] and branching fractions based on [79]. The latter is in turn based on the measurements in [80] and theoretical calculations at the time, which are less accurate than the values measured later in [74, 76, 77]. For example, in [80] the ratio between the branching ratio between of  $P_{3/2} \rightarrow S_{1/2}$  and the sum of branching ratios  $P_{3/2} \rightarrow D_J$  ( $J = 5/2$  and  $3/2$ ) was reported to be  $17.6 \pm 2$ . However it was later refined to be  $14.31(5)$  in [77]. Hence the numbers quoted in James's paper should no longer be used. The  $D_{3/2} \rightarrow S_{1/2}$  and  $D_{5/2} \rightarrow S_{1/2}$  linewidth are deduced from experiments in [81] and [82] respectively.

The saturation intensity for a two-level atom is defined as

$$I_s = \frac{\pi h c \Gamma}{3 \lambda^3} \quad (\text{A.1})$$

where  $\hbar = h/(2\pi)$  is the reduced Planck's constant,  $c$  is the speed of light in vacuum,  $\Gamma$  and  $\lambda$  are the linewidth and wavelength of the transition, respectively.

The Landé g-factor is given by

$$g_J = 1 + \frac{J(J+1) - L(L+1) + S(S+1)}{2J(J+1)} \quad (\text{A.2})$$

where we have used the conventional spectroscopic notation as defined in Chapter 2. The g-factors are given in table A.2. The Clebsch-Gordan coefficients for dipole allowed transition from the  $P_{1/2}$  state are given in Figure 2.4.

## Appendix B

# Solving the Mathieu Equation

I solve here the Mathieu equation (B.1) with the aid of [83, 84]. It takes some 6 theorems and a few corollaries to find the general solutions. Physical limitations are later imposed to extract the stable solutions. An expression for the ion's equation of motion in terms of the  $a$  and  $q$  parameters is derived.

### B.1 General solutions

$$\frac{d^2r}{dt^2} + (a - 2q \cos(2t))r = 0 \quad (\text{B.1})$$

**Theorem 1.** If  $r_1(t)$  is a solution, then so is  $r_1(n\pi + t)$  for integer  $n$ .

*Proof.* Let  $t' = n\pi + t$ .

Then  $dt'^2 = dt^2$  and  $\cos(2t') = \cos(2(n\pi + t)) = \cos(2n\pi)\cos(2t) - \sin(2n\pi)\sin(2t) = \cos(2t)$ . And thus we find that the Mathieu equation is invariant under the transformation  $t \rightarrow t + n\pi$ .  $\square$

**Theorem 2.**  $\exists$  one odd and one even solution

This follows from classical theory of differential equations.

**Theorem 3.**

- i)  $r_1(t)$  is even and  $r_2(t)$  is odd
- ii)  $r_1(0) = \dot{r}_2(0) = 1; \dot{r}_1(0) = r_2(0) = 0$
- iii)  $r_1(t \pm \pi) = r_1(\pi)r_1(t) \pm \dot{r}_1(\pi)r_2(t)$
- iv)  $r_2(t \pm \pi) = \pm r_2(\pi)r_1(t) + \dot{r}_2(\pi)r_2(t)$

$$v) \quad r_1(t)\dot{r}_2(t) - \dot{r}_1(t)r_2(t) = 1$$

$$vi) \quad r_1(\pi) = \dot{r}_2(\pi)$$

*Proof.* i) This is equivalent to theorem 2.

- ii) By an appropriate choice of the arbitrary constants  $r_1(0)$  and  $r_2(0)$  in agreement with i), the values of the derivatives also follow from the even/odd properties of the solutions.
- iii) By theorem 1, if  $r_1(t)$  is a solution, so is  $r_1(t+\pi)$ . Thus, this new solution is expressible in terms of the even and odd solutions. Taking the additive solution, we have

$r_1(t+\pi) = \alpha r_1(t) + \beta r_2(t)$  and  $\dot{r}_1(t+\pi) = \alpha \dot{r}_1(t) + \beta \dot{r}_2(t)$ . By setting  $t = 0$ , we find  $\alpha = r_1(\pi)$  and  $\beta = \dot{r}_1(\pi)$ .

iv) Same principle of iii) apply.

v) Since the Mathieu equation has no terms in the first derivative,  $\dot{r}$ , it follows from the Abel identity that

$$r_1(t)\dot{r}_2(t) - r_2(t)\dot{r}_1(t) = Constant. \quad (B.2)$$

And since  $r_1(0)\dot{r}_2(0) - r_2(0)\dot{r}_1(0) = 1$ , by the choice of initial conditions it follows that

$$r_1(t)\dot{r}_2(t) - r_2(t)\dot{r}_1(t) = 1. \quad (B.3)$$

vi) By setting  $t = \pi$  in the subtractive equations of iii) and iv) and using the periodicity given by theorem 1 with the results in ii), we find

$$r_1(0) = 1 = [r_1(\pi)]^2 - \dot{r}_1(\pi)r_2(\pi) \quad (B.4)$$

$$r_2(0) = 0 = r_2(\pi)r_1(\pi) - \dot{r}_2(\pi)r_1(\pi) \quad (B.5)$$

$$= r_2(\pi)[r_1(\pi) - \dot{r}_2(\pi)] \quad (B.6)$$

Then, either  $r_1(\pi) - \dot{r}_2(\pi) = 0$  which is the result of interest, or  $r_2(\pi) = 0$ . For the latter, we find  $[r_1(\pi)]^2 = 1$  and the expression in v) becomes  $r_1(\pi)\dot{r}_2(\pi) = 1$ . Equating the last two equations we find  $r_1(\pi) = \dot{r}_2(\pi)$ .  $\square$

**Theorem 4. Floquet Theorem:** *The Mathieu equation has at least one solution  $y(t)$  such that  $y(t + \pi) = \sigma y(t)$  where  $\sigma$  is a constant.*

*Proof.* :  $y(t)$  can be expressed as a linear combination of the even and odd solution  $r_1(t)$  and  $r_2(t)$ .

Let  $y(t) = c \cdot r(t)$  where  $c$  is the row vector with arbitrary constant entries  $\begin{pmatrix} c_1 & c_2 \end{pmatrix}$  and  $r(t) = \begin{pmatrix} r_1(t) \\ r_2(t) \end{pmatrix}$ . Then, from theorem 3 iii) and iv), we find,

$$y(t + \pi) = c \cdot r(t + \pi) = c \cdot Ar(t) \quad (\text{B.7})$$

where

$$A = \begin{pmatrix} r_1(\pi) & \dot{r}_1(\pi) \\ r_2(\pi) & \dot{r}_2(\pi) \end{pmatrix} \quad (\text{B.8})$$

Thus to get solutions of the form  $y(t + \pi) = \sigma y(t)$ , we need

$$c \cdot A = \sigma c. \quad (\text{B.9})$$

The solutions satisfy  $|c \cdot (A - \sigma \cdot \mathbb{I}) \cdot c^{-1}| = 0$  or equivalently  $|A - \sigma \cdot \mathbb{I}| = 0$ . Expanding the last expression yields

$$0 = (r_1(\pi) - \sigma)(\dot{r}_2(\pi) - \sigma) - \dot{r}_1(\pi)r_2(\pi) \quad (\text{B.10})$$

$$= \sigma^2 - \sigma(r_1(\pi) + \dot{r}_2(\pi)) + r_1(\pi)\dot{r}_2(\pi) - \dot{r}_1(\pi)r_2(\pi) \quad (\text{B.11})$$

The second term becomes  $2\sigma r_1(\pi)$  by theorem 3 vi) and the last two terms equate to 1 by theorem 3 v). The periodicity equation becomes

$$\sigma^2 - 2\sigma r_1(\pi) + 1 = 0. \quad (\text{B.12})$$

□

**Theorem 5.** *The product of the roots of the periodicity  $\sigma$  is unity.*

*Proof.* If we define  $\sigma_1$  and  $\sigma_2$  the roots of the periodicity equation obtained in the last theorem such that  $(\sigma - \sigma_1)(\sigma - \sigma_2) = 0$ . Thus,  $\sigma_1\sigma_2 = 1$ . □

**Corollary 1.** *The Mathieu equation has at least one pseudo-periodic solution  $y(t) = e^{\mu t}\phi(t)$  where we have defined  $\sigma = e^{\mu t}$  with constant  $\mu$  and  $\phi(t)$  has period  $\pi$ .*

*Proof.*

$$\begin{aligned} y(t + \pi) &= \sigma y(t) \\ \phi(t + \pi) &= e^{-\mu(t+\pi)}y(t + \pi) \\ &= e^{-\mu\pi}e^{-\mu t}\sigma y(t) \\ &= \sigma^{-1}e^{-\mu t}\sigma y(t) \\ &= e^{-\mu t}y(t) = \phi(t) \end{aligned}$$

□

**Corollary 2.** *If the Mathieu equation has a solution with periodicity factor  $\sigma (\neq \pm 1)$  then  $\exists$  an independent solution with periodicity factor  $\sigma^{-1}$ .*

*Proof.* Let  $y_1(t) = e^{\mu t} \phi(t)$  be a solution with periodicity  $\sigma$  such that  $y_1(t + \pi) = \sigma y_1(t)$  and  $\phi(t)$  has period  $\pi$ . By theorem 1,  $y_2(t) \equiv y_1(-t) = e^{-\mu t} \phi(-t)$  is also a solution. We have

$$y_2(t + \pi) = y_1(-t - \pi) = e^{-\mu(-t-\pi)} \phi(-t - \pi) \quad (\text{B.13})$$

$$= e^{-\mu\pi} e^{-\mu t} \phi(-t) \quad (\text{B.14})$$

$$y_1(t + \pi) = e^{\mu(t+\pi)} \phi(t + \pi) \quad (\text{B.15})$$

$$= e^{\mu t} e^{\mu\pi} \phi(t) \quad (\text{B.16})$$

Taking their ratio, we find

$$\frac{y_2(t + \pi)}{y_1(t + \pi)} = e^{-2\mu\pi} \frac{e^{-\mu t} \phi(-t)}{e^{\mu t} \phi(t)} \quad (\text{B.17})$$

$$= \sigma^{-2} \frac{y_2(t)}{y_1(t)} \quad (\text{B.18})$$

$$\neq \frac{y_2(t)}{y_1(t)} \quad \text{for } \sigma \neq \pm 1 \quad (\text{B.19})$$

□

**Corollary 3.**  $\sigma_1 = \sigma_2$  iff  $\sigma_1 = \sigma_2 = \pm 1$ .

This follows from  $\sigma_1 \sigma_2 = 1$  in theorem 5.

**Corollary 4.** *The Mathieu equation has a basically periodic solution, that is, periodic in  $\pi$ , iff the roots of the periodicity are equal.*

This follows from the expression  $y(t + \pi) = \sigma y(t)$  and corollary 3.

**Corollary 5.** *If  $y_1(t)$  is a solution with periodicity factor  $\sigma$ , periodicity exponent  $\mu$ , then  $y_1(-t)$  is a solution with periodicity  $\sigma^{-1}$ , periodicity exponent  $-\mu$ .*

This follows immediately from the proof of corollary 2.

### Theorem 6.

i) If  $r_1(t)$  has period  $\pi$ , then the second solution has the form

$$r_2(t) = \pm \pi^{-1} r_2(\pi) \cdot t \cdot r_1(t) + u(t), \text{ where } u(t) \text{ has period } \pi.$$

ii) If  $r_2(z)$  has period  $\pi$ , then the second solution has the form

$$r_1(t) = \pm \pi^{-1} \dot{r}_1(\pi) \cdot t \cdot r_2(t) + u(t), \text{ where } u(t) \text{ has period } \pi.$$

[This is closely related to Ince's theorem, that the Mathieu equation never possesses 2 basically periodic solutions for the same values of  $a$  and  $q$ , except for the trivial case of  $q = 0$ .]

*Proof.* For the first case i), we have from theorem 3 vi) combined with the periodicity of  $r_1$

$$\dot{r}_2(\pi) = r_1(\pi) = r_1(0) = 1 \quad (\text{B.20})$$

Then from theorem 3 iv), we have  $r_2(t + \pi) = r_2(\pi)r_1(t) + r_2(t)$  which can be rearranged to

$$r_2(\pi)r_1(t) = r_2(t + \pi) - r_2(t) \quad (\text{B.21})$$

Now let us define

$$u(t) = r_2(t) - \pi^{-1}r_2(\pi) \cdot t \cdot r_1(t). \quad (\text{B.22})$$

Then

$$u(t + \pi) = r_2(t + \pi) - \pi^{-1}r_2(\pi) \cdot (t + \pi) \cdot r_1(t + \pi) \quad (\text{B.23})$$

$$= r_2(t + \pi) - \pi^{-1}r_2(\pi) \cdot (t + \pi) \cdot r_1(t) \quad (\text{B.24})$$

Thus

$$\begin{aligned} u(t + \pi) - u(t) &= r_2(t + \pi) - r_2(t) - \pi\pi^{-1}r_2(\pi)r_1(t) \\ &= r_2(\pi)r_1(t) - r_2(\pi)r_1(t) \quad \text{by equation B.21} \\ &= 0 \end{aligned}$$

Likewise, in case ii) where  $r_2(t + \pi) = r_2(t)$ , we find  $r_1(\pi) = \dot{r}_2(\pi) = \dot{r}_2(0) = 1$ . Using theorem 3 iii),  $r_1(t + \pi) = r_1(t) + \dot{r}_1(\pi)r_2(t)$ . We then define

$$u(t) = r_1(t) - \pi^{-1}\dot{r}_1(\pi) \cdot t \cdot r_2(t). \quad (\text{B.25})$$

Then

$$u(t + \pi) = r_1(t + \pi) - \pi^{-1}\dot{r}_1(\pi)(t + \pi)r_2(t) \quad (\text{B.26})$$

which can be used to show the required relation  $u(t + \pi) = u(t)$   $\square$

## Summary

The nature of the general solutions depends on the nature of the roots of the periodicity equation with two main cases to distinguish.

**Case 1:** The periodicity roots are different.  $\sigma \neq \sigma^{-1}$ . The periodicity roots have different periodicity exponents  $\mu$  and  $-\mu$ . This results in two pseudo-periodic solutions:

$$y_1(t) = e^{\mu t} \phi(t) \quad (\text{B.27})$$

$$y_2(t) = e^{-\mu t} \phi(-t) \quad (\text{B.28})$$

**Case 2:** The periodicity roots are identical.  $\sigma_1 = \sigma_2 = \pm 1$ . The periodicity roots have the same periodicity exponents,  $\mu_1 = \mu_2$ . This results in one basically periodic solution and one non-periodic, non-pseudo-periodic solution. for example:

$$y_1(t) = \phi(t) \quad (\text{B.29})$$

$$y_2(t) = \pi y_2(\pi) \cdot t \cdot y_1(t) + u(t) \quad (\text{B.30})$$

[Recall from theorem 5 that the product of the roots of the periodicity factor is unity. And in corollary 1 we have made the definition  $\sigma = e^{\mu t}$ . Thus

$$\sigma_1 \sigma_2 = e^{(\mu_1 + \mu_2)\pi} = 1 \quad (\text{B.31})$$

Hence  $\mu_1 + \mu_2 = 2ni$  with integer  $n$ . It follows that in case 2,  $\mu_1 = \mu_2 = \text{integer.}$ ]

## B.2 Stable solutions

Stability means that the position of the particle being trapped is bounded at all times, i.e. we do not lose the particle. We can straightforwardly see that *case 2* is unstable. Even though one of its solutions is periodic, the second solution has a term proportional to  $t$ . Therefore as  $t \rightarrow \infty$ ,  $r \rightarrow \infty$ . We get this type of solution when  $\mu_1 = \mu_2$ . But since  $\mu_1 + \mu_2 = 2ni$ , the condition to get this type of solution becomes to have integer  $\beta$  where  $\mu = i\beta$ . Hence to avoid unstable solutions one condition is  $\mu \neq ni$ .

For *case 1* where  $\mu_1 = -\mu_2$ , the relation  $\mu_1 + \mu_2 = 2ni$  is satisfied by any real entries  $\alpha$  and  $\beta$  in  $\mu = \alpha + i\beta$ . However consideration of stability solutions means that  $\mu$  must not have a real component as otherwise, both solutions will have terms which will grow exponentially in time. Thus our second condition for stability is to have  $\mu$  as purely imaginary.

Altogether, the condition for stability is to have  $\mu = i\beta$  where  $\beta$  is real and a non-integer.

### B.3 Equation of motion

We have so far seen the stable solutions to the Mathieu equations in terms of  $\beta$  and  $\phi$ . But how are these related to the  $a$  and  $q$  parameters? I cover that here.

Using the stability criteria  $\mu = i\beta$  where  $\beta$  is a non-integer but more importantly here, real, we can rewrite the stable solutions (B.27) and (B.28) as

$$y_1(t) = e^{\beta t} \phi(t) \quad (\text{B.32})$$

$$y_2(t) = e^{-\beta t} \phi(-t). \quad (\text{B.33})$$

The general solution to the Mathieu equation is some superposition of these solutions:

$$y(t) = A'y_1(t) + B'y_2(t) \quad (\text{B.34})$$

where  $A'$  and  $B'$  are arbitrary constants deduced from initial conditions.

Recall that  $\phi(t)$  is a basically periodic function. As such, we make a suitable exponential series expansion:

$$\phi(t) = \sum_{n=-\infty}^{+\infty} c_{2n} e^{2nit} \quad (\text{B.35})$$

This makes

$$\phi(-t) = \sum_{n=-\infty}^{+\infty} c_{2n} e^{-2nit} \quad (\text{B.36})$$

(B.32) and (B.33) become

$$y_1(t) = \sum_{n=-\infty}^{+\infty} c_{2n} e^{i(2n+\beta)t} \quad (\text{B.37})$$

$$y_2(t) = \sum_{n=-\infty}^{+\infty} c_{2n} e^{-i(2n+\beta)t}. \quad (\text{B.38})$$

Expanding to a trigonometric series, we rewrite the general expression (B.34) as

$$y(t) = A' \sum_{-\infty}^{\infty} c_{2n} [\cos((2n+\beta)t) + i \sin((2n+\beta)t)] \quad (\text{B.39})$$

$$+ B' \sum_{-\infty}^{\infty} c_{2n} [\cos((2n+\beta)t) - i \sin((2n+\beta)t)] \quad (\text{B.40})$$

$$= A \sum_{-\infty}^{\infty} c_{2n} \cos((2n+\beta)t) + i B \sum_{-\infty}^{\infty} c_{2n} \sin((2n+\beta)t) \quad (\text{B.41})$$

where  $A = A' + B'$  and  $B = A' - B'$ .

We substitute this back in into the Mathieu equation B.1. We find

$$\begin{aligned}
& -A \sum_{-\infty}^{\infty} c_{2n} (2n + \beta)^2 \cos((2n + \beta)t) - iB \sum_{-\infty}^{\infty} c_{2n} (2n + \beta)^2 \sin((2n + \beta)t) + a \cdot y(t) \\
&= 2qA \sum_{-\infty}^{\infty} c_{2n} \cos(2t) \cos((2n + \beta)t) + iB \sum_{-\infty}^{\infty} c_{2n} \cos(2t) \sin((2n + \beta)t) \\
&= 2qA \sum_{-\infty}^{\infty} c_{2n} \{ \cos((2n + 2 + \beta)t) + \cos((2n - 2 + \beta)t) \} \\
&\quad + iB \sum_{-\infty}^{\infty} c_{2n} \{ \sin((2 + 2n + \beta)t) + \sin((2 - 2n + \beta)t) \} \\
&= 2qA \sum_{-\infty}^{\infty} \left( \frac{c_{2n-2}}{2} + \frac{c_{2n+2}}{2} \right) \cos((2n + \beta)t) \\
&\quad + iB \sum_{-\infty}^{\infty} \left( \frac{c_{2n-2}}{2} - \frac{c_{2n+2}}{2} \right) \sin((2n + \beta)t).
\end{aligned}$$

Solving for time  $t = 0$ , we have

$$\sum_{-\infty}^{\infty} \left[ \frac{a - (2n + \beta)^2}{q} c_{2n} - c_{22-2} - c_{2n+2} \right] = 0. \quad (\text{B.42})$$

To satisfy this for all  $a$  and  $q$ , we have to satisfy the recursion relation

$$d_{2n} c_{2n} - c_{2n-2} - c_{2n+2} = 0 \quad (\text{B.43})$$

where

$$d_n = \frac{a - (2n + \beta)^2}{q}. \quad (\text{B.44})$$

For  $n = 0$ , we thus have

$$\beta^2 = a - q \left( \frac{c_2}{c_0} + \frac{c_{-2}}{c_0} \right). \quad (\text{B.45})$$

To find the fractions  $c_2/c_0$ , we derive from B.43 the following

$$\frac{c_{2n}}{c_{2n-2}} = \frac{1}{d_{2n} - \frac{c_{2n+2}}{c_{2n}}}. \quad (\text{B.46})$$

Note that this equation can be recursively be plugged into itself.

$$\frac{c_{2n}}{c_{2n-2}} = \frac{1}{d_{2n} - \frac{1}{d_{2n+2} - \dots}}. \quad (\text{B.47})$$

Likewise, to find an expression  $c_{-2}/c_0$ , we find from B.43

$$\frac{c_{2n}}{c_{2n+2}} = \frac{1}{d_{2n} - \frac{c_{2n-2}}{c_{2n}}} \quad (\text{B.48})$$

$$= \frac{1}{d_{2n} - \frac{1}{d_{2n-2} - \dots}}. \quad (\text{B.49})$$

We note that typically  $(|a_i|, |q_i|) \ll 1$  in ion traps. Plugging in B.47 and B.49 into B.45 and substituting for  $d_{2n}$  yields to first order in  $q$

$$\beta^2 = a - q \left( \frac{1}{d_2} + \frac{1}{d_{-2}} \right) \quad (\text{B.50})$$

$$= a - q \left( \frac{q}{a - (2 + \beta)^2} + \frac{q}{a - (-2 + \beta)^2} \right) \quad (\text{B.51})$$

$$\approx a + q \left( \frac{q}{(2 + \beta)^2} + \frac{q}{(-2 + \beta)^2} \right) \quad (\text{B.52})$$

$$\approx a + \frac{q^2}{2} \quad (\text{B.53})$$

where we have inferred that  $\beta \ll 1$  for B.52 to hold.

## Appendix C

# The electrode assembly and its integration with a fibre cavity

### C.1 The electrode-assembly making method

To ensure good concentricity between the IE (inner electrode) and the OE (outer electrode) the following procedure is employed. OEs are cut to the correct length and polished. Ceramic spacers are also cut/polished down to the required length (~3mm) using diamond needle files. A long IE tube (~5 cm) is cut and its face polished. This tube is then mounted on a microstage. The ceramic spacer is slotted in the OE and the pair are held in a mount (preferably a Gognio<sup>1</sup> stage) ready for the IE to be inserted. One camera is used to monitor the concentricity after insertion. The IE is inserted and the concentricity set using the stages. The protrusion length is set accurately later by polishing the IE face further. Optionally a second camera from the side can be used to monitor and set the protrusion distance precisely. Degassed<sup>2</sup> fibre epoxy glue<sup>3</sup> is used after the insertion and concentricity setting process. This glue takes the least time<sup>4</sup> to cure but others can work too as long as they are UHV compatible. A small home made oven (using high wattage resistor) was used to cure the glue in situ.

---

<sup>1</sup>A Gonio stage or a goniometer is a device used for rotating an object with precision.

<sup>2</sup>Placed in vacuum ( $\sim 10^{-2}$  mbar for 2 runs lasting  $\sim 5$  minutes to rid the adhesive of any air bubbles)

<sup>3</sup>EPO-TEK 353ND A/B, amber/red

<sup>4</sup>Amongst all the glues mentioned in this thesis.

## C.2 Insertion setup

This subsection describes the fibre insertion process. The procedure is arguably the most delicate part of the experiment. The fibre is bare and is susceptible to many dangers: its coated facet can get damaged by deposition of dirt or through collisions with walls, a sudden movement can snap the fibre, unevenness in the fibre coating diameter can result in the fibre getting stuck midway through insertion, etc... Extra care is taken to ensure the safety of the procedure.

The insertion is performed in a flow box to work in a dust-free environment. The air flow is temporarily interrupted during the insertion as it causes vibrations. The set up used is shown in Figure C.1 and the components described in the caption.

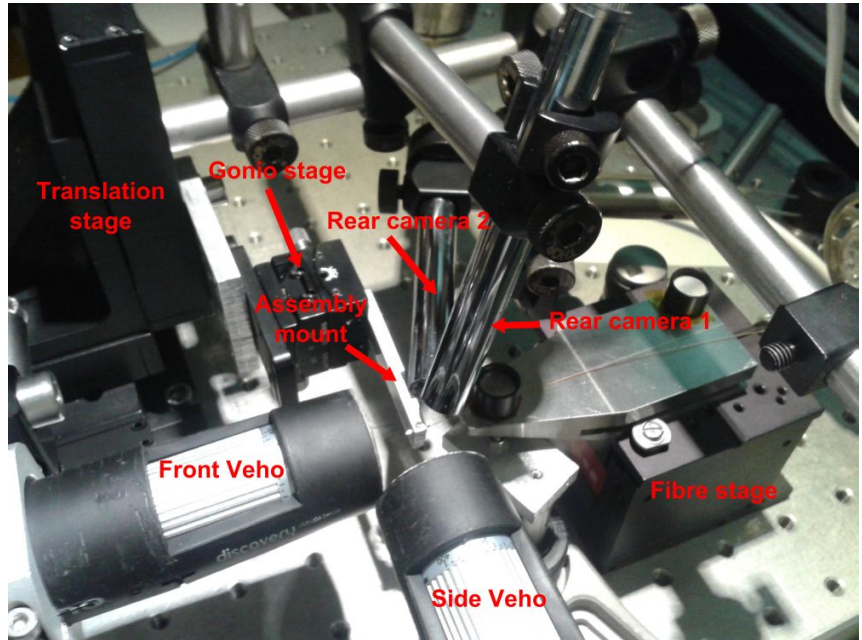


Figure C.1: The fibre insertion set up. The fibre is mounted on a microstage (*fibre stage*); it is held in a v-groove by a magnetic soft clamp. The electrode assembly can be seen at the end of the *assembly mount* to which it is attached by a grub screw. The assembly mount is attached to a *Gonio stage* which in turn is attached to a *translational stage*. The Gonio stage has two rotational degrees of freedom. *Rear cameras 1* and *2* are used to monitor the fibre at the tail of the electrode assembly. The *front Veho* camera monitors the concentricity of the fibre with the IE as it enters it. The *side Veho* is used to signal when the fibre becomes flush with the IE. To complete the insertion process, the fibre is recessed by the required amount using the fibre stage. A digital micrometer at the rear of the fibre stage (not shown in the image) is added for a precise reading of the fibre recess as the fibre is pulled back.

In the fibre insertion process, there are three spatial axes that must be considered:

- the fibre's axis of cylindrical symmetry. (This is empirically found to be almost always different to that of the translational axis of the stage it is mounted on. This is because of subtle bends along the fibre length),
- the translational axis of the translational stage and
- the electrode assembly's axis of cylindrical symmetry.

If these three axes were parallel, the insertion process would be straight forward. However, this is not the case. As such we resorted to an insertion procedure which uses an iterative sequence to ensure good concentricity between the fibres and their electrodes.

Using the setup shown in Figure C.1, the fibre is first mounted on the fibre stage and clamped in the v-groove. An initial approach to the electrode assembly is made using the fibre stage until the fibre is in the field of view of the rear cameras. After this, only the translational stage and the Gonio stage are used in the insertion process while the fibre is kept still. The rear cameras and the front Veho<sup>5</sup> camera are used to monitor the alignment of the electrode as it moved over the fibre. The rear cameras are attached to the translational stage and so move together with the electrode assembly. The rear cameras are used to ensure the fibre does not make contact with the electrode wall (see Figure C.2). The front camera looks through the electrode assembly and is focused on the fibre facet. Though blurred, the inner electrode's perimeter can be made out enough to judge the concentricity with the fibre. Shining white light through the fibre helps in identifying the fibre core in the image as shown in Figure C.3.

The insertion process is as follows:

1. Optimise the concentricity at the tails of the electrode using the translation stage and the rear cameras.
2. Optimise the concentricity at the fibre facet using the Gonio stage to rotate the electrode vertically and horizontally while referring to the Veho camera image.
3. Repeat steps 1 and 2 until the concentricities both at the electrode tail and the fibre face are fine. This would imply that the electrode and fibre are now fairly parallel.
4. Move the electrode forward a small increment. This step will generally degrade the degree of parallelism between the fibre and the electrode.

---

<sup>5</sup>Veho is the brand name of the camera; we employ it to distinguish it from the other cameras.

5. Go back to step 1 and repeat.

At the end of the procedure, the fibre will be visible with the side Veho camera. The fibre facet is set flush with the IE. A digital micrometer is then attached to the fibre stage and initialised. The fibre is then slowly recessed using the fibre stage by the required amount. The digital micrometer is used for the recess reading. The digital micrometer is added because of low confidence in the fibre stage's reading following a malfunction.

Once the recess has been set, a slow drying glue<sup>6</sup> is applied to the fibre-IE interface at the rear of the IE to permanently fix the fibre to the assembly (see Figure C.4). The reasoning behind the choice of glue is mainly to avoid having to heat the adhesive to induce curing. A fast cure time would be ideal but most fast curing UHV compatible adhesives require heating to induce curing. Heating causes low viscosity. As a result the glue may creep the length of the fibre in the IE though capillary effects and get on the coated facet.

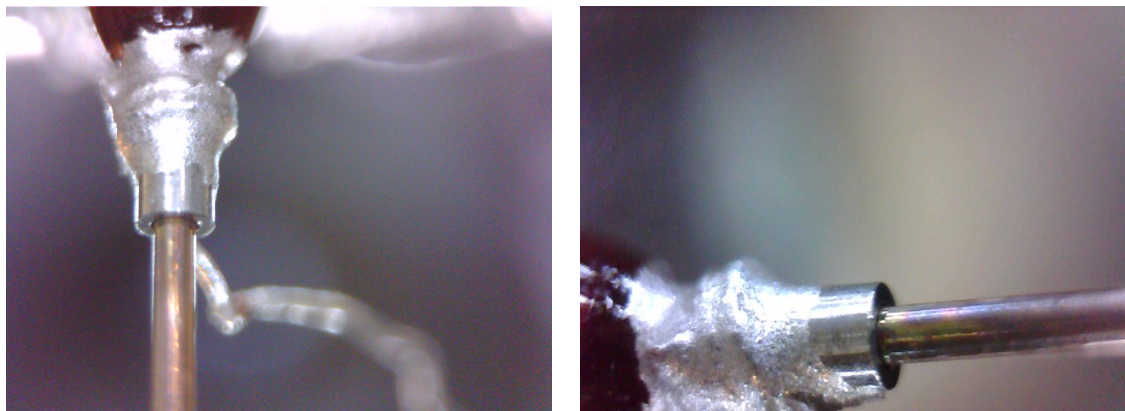


Figure C.2: The views from rear cameras 1 and 2. The cameras are focused on the tail of the inner electrode to ensure the fibre does not make contact with the electrode facet and wall as it is guided through. The amber part on the electrode is the epoxy glue used to hold the electrode assembly together. The silver compound covering the winding near the tail of the electrode is conductive glue<sup>7</sup> used for good electrical contact between the wire and the inner electrode. The wire is a thin flimsy wire used to rf-ground and deliver dc voltages to the inner electrode. That it is thin and flimsy relieves the entire assembly from any tension and thus helps to isolate it from vibrations. This is a crucial consideration for cavity locking.

---

<sup>6</sup>STYCAST 2850-FT

<sup>7</sup>EPO-TEK H21D

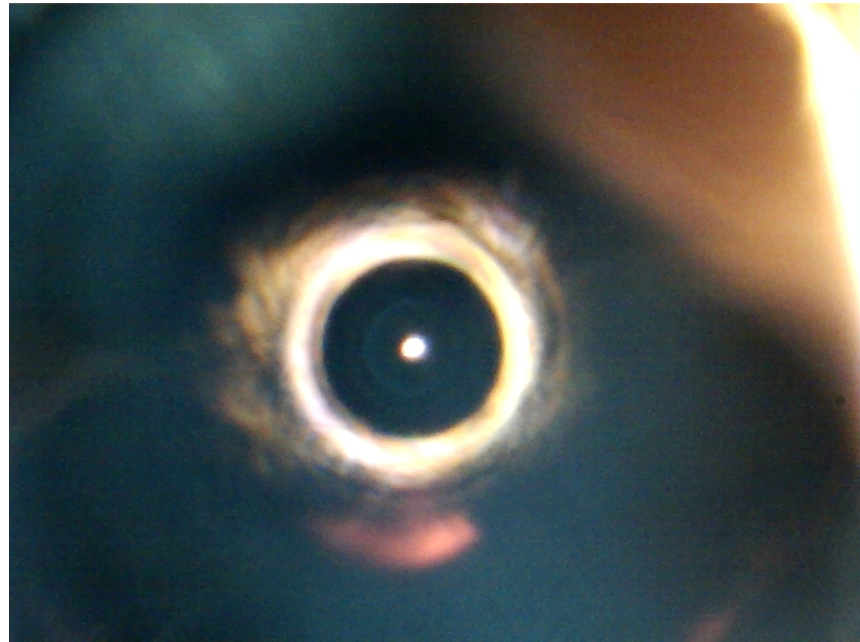


Figure C.3: The view from the front Veho camera looking through the inner electrode of the assembly. The fibre core is illuminated by injecting a white light at its rear end. A closer look reveals te outer edge of the cladding. The inner electrode facet is blurred as is it out of focus. Nonetheless, one can make out its perimeter and infer its centre. Further, as the insertion progresses and the electrode and fibre facets are nearer to one another, the electrode becomes better focused.



Figure C.4: The rear of the assembly after the fibre has been inserted and glue (shiny black substance) has been applied to permanently secure the fibre to the assembly.

### C.3 Brief account of previous designs

Several improvements have led up to the current design of the set-up. Some of the key changes are listed here.

1. One rather optimistic idea was to make the fibre cavities reusable. Instead of gluing them to the inner electrode, we used an intermediate device, a *chuck*, which clamps to the inner electrode on one side and clamps the fibre between two Teflon wedges on the other. This design was not sturdy and caused issues with cavity locking. Slippage of the fibre in the IE was noticed as the chuck moved.
2. In the earlier versions of the design, we used to deliver rf to the inner electrode via the copper coating of the fibre. One problem with this was that the rf signal was being shorted through a weak conduction point where the fibre was connected to another fibre via a mating sleeve. Despite the etching of the copper coating, the graphite layer on the fibres were providing an electrical conduction medium. We have had to set a small gap between the ferrules to mitigate short circuits at the expense of optical transmission losses. Another design issue with delivering rf via the Cu coating is that the length of the two fibres needed to be the same to ensure phase matching. However, the geometry of the trap design was such that one fibre was further from the rf application platform than the other fibre. Limited chamber space added strain to ensuring that neither of the fibres get short circuited.
3. Rf used to be delivered to the IE. But this meant that the side rf electrodes were less effective. By applying rf to the OE, the ion can be moved a further distance with the same voltage on the side electrodes.
4. The IE length has significantly been shortened from 12 mm in the older assembly designs to 6 mm. This shorter length means (i) easier insertion procedure, (ii) better concentricity between the fibre and the IE (long IE length meant that the fibre was immobile inside the IE and thus the concentricity could not be adjusted) and (iii) shorter fibre length dangling in the IE which means small vibrations which lead to better cavity locking.
5. Short flimsy wires are now attached to the IEs for delivering DC. Likewise for delivering rf, a flimsy wire is used close to the assembly. This is to reduce any tension and hence the propagation of vibration to the assembly. This means a more stable cavity.

6. EPO-TEK 353ND A/B and EPO-TEK H21D were trialled to glue to the fibre to the assembly in the past. The former was found to get quite runny in the curing process and could thus end up on the coated fibre facet. The latter was found to not cure properly using local heating system such as small home-made resistively heated ovens. Additionally, it dissolved in common solvents used in the cleaning of the fibre (including isopropanol and acetone). When an assembly using this glue was placed in an ultrasonic bath (in an isopropanol solution) to clean the fibre, the fibre would ironically come out dirtier because of dissolving epoxy.

## Appendix D

### Biquad filters

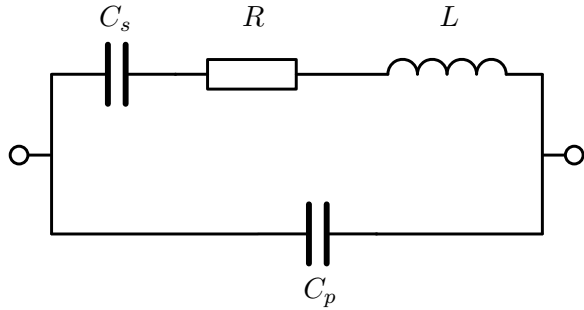


Figure D.1: An equivalent circuit exhibiting the piezo response consisting of an inductor,  $L$ , a resistor  $R$  with a series capacitor  $C_s$  and a parallel capacitor,  $C_p$ .

We have seen that the piezos exhibit a resonance-antiresonance frequency response. This has an equivalent circuit model (Figure D.1) which is described by the following transfer function

$$T(s = i\omega) = \frac{s^2 + s\omega_n/Q + \omega_n^2}{s^2 + s\omega'_n/Q + \omega'^2_n}. \quad (\text{D.1})$$

for frequency  $\omega$  where  $\omega_n$  and  $\omega'_n$  are the resonance and antiresonance frequencies, respectively, with quality  $Q$ .

Therefore if we use a filter whose transfer function is the inverse of  $T$ , that is,

$$\frac{s^2 + s\omega'_n/Q + \omega'^2_n}{s^2 + s\omega_n/Q + \omega_n^2}, \quad (\text{D.2})$$

we can “flatten” the frequency response in the region of interest. This type of filter is called a *bi-quadratic* or *biquad* filer. Figure D.2 shows plots of Equation D.2 for various  $Q$  values and with  $\omega_n = 920$  Hz and  $\omega'_n = 890$  Hz (similar to one of the response features in the experimental set up). The maximum phase advancement depends on the value of  $Q$ . For the implementation of a filter that compensates the piezo response, one should first set the appropriate  $Q$ .

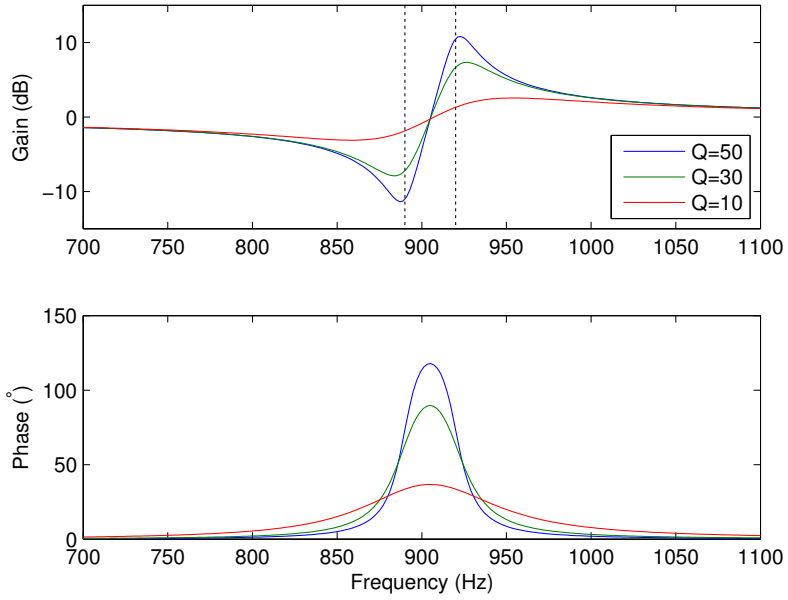


Figure D.2: The gain and phase described by Equation D.2 when  $\omega_n = 920$  Hz and  $\omega'_n = 890$  Hz (represented by dotted lines) for varying  $Q$ .

The filter function ( $1/T$ ) can be implemented by a sum of a low-pass filter,

$$\frac{\omega_n'^2}{s^2 + s\omega_n/Q + \omega_n^2},$$

a band-pass filter,

$$\frac{s\omega_n'/Q}{s^2 + s\omega_n/Q + \omega_n^2},$$

and a high-pass filter,

$$\frac{s^2}{s^2 + s\omega_n/Q + \omega_n^2}.$$

We have implemented all these quadratic filters in a single chip (UAF42, Texas Instruments) based on a state-variable architecture which allows the independent configuration of low-pass, band-pass and high-pass filters.

# Bibliography

- [1] Freedman, S. J. and Clauser, J. F. Experimental test of local hidden-variable theories. *Phys. Rev. Lett.*, **28**:938–941, Apr 1972. <http://link.aps.org/doi/10.1103/PhysRevLett.28.938>. (Cited on 1)
- [2] Shor, P. W. Polynomial-time algorithms for prime factorization and discrete logarithms on a quantum computer. *SIAM Journal on Computing*, **26**(5):1484–1509, 1997. <http://dx.doi.org/10.1137/S0097539795293172>. (Cited on 1)
- [3] Bennett, C. H., Bessette, F., Brassard, G., Salvail, L., and Smolin, J. Experimental quantum cryptography. *Journal of Cryptology*, **5**(1):3–28, 1992. ISSN 1432-1378. <http://dx.doi.org/10.1007/BF00191318>. (Cited on 2)
- [4] Bouwmeester, D., Pan, J.-W., Mattle, K., Eibl, M., Weinfurter, H., and Zeilinger, A. Experimental quantum teleportation. *Nature*, **390**(6660):575–579, Dec 1997. ISSN 0028-0836. <http://dx.doi.org/10.1038/37539>.
- [5] Vandersypen, L. M. K., Steffen, M., Breyta, G., Yannoni, C. S., Sherwood, M. H., and Chuang, I. L. Experimental realization of Shor’s quantum factoring algorithm using nuclear magnetic resonance. *Nature*, **414**(6866):883–887, Dec 2001. ISSN 0028-0836. <http://dx.doi.org/10.1038/414883a>. (Cited on 2)
- [6] Martin-Lopez, E., Laing, A., Lawson, T., Alvarez, R., Zhou, X.-Q., and O’Brien, J. L. Experimental realization of Shor’s quantum factoring algorithm using qubit recycling. *Nat Photon*, **6**(11):773–776, Nov 2012. ISSN 1749-4885. <http://dx.doi.org/10.1038/nphoton.2012.259>. (Cited on 2)
- [7] Xu, N., Zhu, J., Lu, D., Zhou, X., Peng, X., and Du, J. Quantum factorization of 143 on a dipolar-coupling nuclear magnetic resonance system. *Phys. Rev. Lett.*, **108**:130501, Mar 2012. <http://link.aps.org/doi/10.1103/PhysRevLett.108.130501>. (Cited on 2)

- [8] DiVincenzo, D. P. The physical implementation of quantum computation. *Fortschritte der Physik*, **48**(9-11):771–783, 2000. ISSN 1521-3978. [http://dx.doi.org/10.1002/1521-3978\(200009\)48:9/11<771::AID-PROP771>3.0.CO;2-E](http://dx.doi.org/10.1002/1521-3978(200009)48:9/11<771::AID-PROP771>3.0.CO;2-E). (Cited on 2)
- [9] Paul, W. Electromagnetic traps for charged and neutral particles. *Rev. Mod. Phys.*, **62**:531–540, Jul 1990. <http://link.aps.org/doi/10.1103/RevModPhys.62.531>. (Cited on 2, 29)
- [10] Häffner, H., Roos, C., and Blatt, R. Quantum computing with trapped ions. *Physics Reports*, **469**(4):155 – 203, 2008. ISSN 0370-1573. <http://www.sciencedirect.com/science/article/pii/S0370157308003463>. (Cited on 2)
- [11] Harty, T. P., Allcock, D. T. C., Ballance, C. J., Guidoni, L., Janacek, H. A., Linke, N. M., Stacey, D. N., and Lucas, D. M. High-fidelity preparation, gates, memory, and readout of a trapped-ion quantum bit. *Phys. Rev. Lett.*, **113**:220501, Nov 2014. <http://link.aps.org/doi/10.1103/PhysRevLett.113.220501>. (Cited on 2)
- [12] Knill, E. Quantum computing with realistically noisy devices. *Nature*, **434**(7029):39–44, Mar 2005. ISSN 0028-0836. <http://dx.doi.org/10.1038/nature03350>. (Cited on 2)
- [13] Harty, T. P., Sepiol, M. A., Allcock, D. T. C., Ballance, C. J., Tarlton, J. E., and Lucas, D. M. High-fidelity trapped-ion quantum logic using near-field microwaves. *Phys. Rev. Lett.*, **117**:140501, Sep 2016. <http://link.aps.org/doi/10.1103/PhysRevLett.117.140501>. (Cited on 2)
- [14] Cirac, J. I. and Zoller, P. Quantum computations with cold trapped ions. *Phys. Rev. Lett.*, **74**:4091–4094, May 1995. <http://link.aps.org/doi/10.1103/PhysRevLett.74.4091>. (Cited on 2)
- [15] Martinis, J. M. Qubit metrology for building a fault-tolerant quantum computer. *Npj Quantum Information*, **1**:15005, Oct 2015. <http://dx.doi.org/10.1038/npjqi.2015.5>. Editorial. (Cited on 3)
- [16] Fowler, A. G., Mariantoni, M., Martinis, J. M., and Cleland, A. N. Surface codes: Towards practical large-scale quantum computation. *Phys. Rev. A*, **86**:032324, Sep 2012. <http://link.aps.org/doi/10.1103/PhysRevA.86.032324>. (Cited on 3)
- [17] Monz, T., Schindler, P., Barreiro, J. T., Chwalla, M., Nigg, D., Coish, W. A., Harlander, M., Hänsel, W., Hennrich, M., and Blatt, R. 14-qubit entanglement: Creation

- and coherence. *Phys. Rev. Lett.*, **106**:130506, Mar 2011. <http://link.aps.org/doi/10.1103/PhysRevLett.106.130506>. (Cited on 3, 5)
- [18] Dicke, R. H. Coherence in spontaneous radiation processes. *Phys. Rev.*, **93**:99–110, Jan 1954. <https://link.aps.org/doi/10.1103/PhysRev.93.99>. (Cited on 3)
- [19] Palma, G. M., Suominen, K.-A., and Ekert, A. K. Quantum computers and dissipation. *Proceedings of the Royal Society of London A: Mathematical, Physical and Engineering Sciences*, **452**(1946):567–584, 1996. ISSN 1364-5021. <http://rspa.royalsocietypublishing.org/content/452/1946/567>. (Cited on 3)
- [20] Kimble, H. J. The quantum internet. *Nature*, **453**:1023–1030, Jun 2008. <http://dx.doi.org/10.1038/nature07127>. (Cited on 3)
- [21] Kielpinski, D., Monroe, C., and Wineland, D. J. Architecture for a large-scale ion-trap quantum computer. *Nature*, **417**(6890):709–711, Jun 2002. ISSN 0028-0836. <http://dx.doi.org/10.1038/nature00784>. (Cited on 3)
- [22] Rowe, M. A., Ben-Kish, A., Demarco, B., Leibfried, D., Meyer, V., Beall, J., Britton, J., Hughes, J., Itano, W. M., Jelenković, B., Langer, C., Rosenband, T., and Wineland, D. J. Transport of quantum states and separation of ions in a dual rf ion trap. *Quantum Information and Computation*, **2**(4):257–271, 2002. [www.scopus.com](http://www.scopus.com). (Cited on 3)
- [23] Hensinger, W. K., Olmschenk, S., Stick, D., Hucul, D., Yeo, M., Acton, M., Deslauriers, L., Monroe, C., and Rabchuk, J. T-junction ion trap array for two-dimensional ion shuttling, storage, and manipulation. *Applied Physics Letters*, **88**(3):034101, 2006. <http://dx.doi.org/10.1063/1.2164910>. (Cited on 3)
- [24] Keller, M., Lange, B., Hayasaka, K., Lange, W., and Walther, H. Continuous generation of single photons with controlled waveform in an ion-trap cavity system. *Nature*, **431**:1075–1078, Oct 2004. <http://dx.doi.org/10.1038/nature02961>. (Cited on 3, 4, 5)
- [25] Duan, L.-M., Lukin, M. D., Cirac, J. I., and Zoller, P. Long-distance quantum communication with atomic ensembles and linear optics. *Nature*, **414**(6862):413–418, Nov 2001. ISSN 0028-0836. <http://dx.doi.org/10.1038/35106500>. (Cited on 3)
- [26] Imamoglu, A., Schmidt, H., Woods, G., and Deutsch, M. Strongly interacting photons

- in a nonlinear cavity. *Phys. Rev. Lett.*, **79**:1467–1470, Aug 1997. <https://link.aps.org/doi/10.1103/PhysRevLett.79.1467>. (Cited on 3)
- [27] Yamamoto, Y. Photonics: A photon in solitary confinement. *Nature*, **390**(6655): 17–18, Nov 1997. ISSN 0028-0836. <http://dx.doi.org/10.1038/36206>. (Cited on 3)
- [28] Gheri, K. M., Alge, W., and Grangier, P. Quantum analysis of the photonic blockade mechanism. *Phys. Rev. A*, **60**:R2673–R2676, Oct 1999. <https://link.aps.org/doi/10.1103/PhysRevA.60.R2673>. (Cited on 3)
- [29] Hunger, D., Steinmetz, T., Colombe, Y., Deutsch, C., Hänsch, T. W., and Reichel, J. A fiber Fabry-Pérot cavity with high finesse. *New Journal of Physics*, **12**(6):065038, 2010. <http://stacks.iop.org/1367-2630/12/i=6/a=065038>. (Cited on 4, 20)
- [30] Takahashi, H., Morphew, J., Orucević, F., Noguchi, A., Kassa, E., and Keller, M. Novel laser machining of optical fibers for long cavities with low birefringence. *Opt. Express*, **22**(25):31317–31328, Dec 2014. <http://www.opticsexpress.org/abstract.cfm?URI=oe-22-25-31317>. (Cited on 4, 20, 24)
- [31] Colombe, Y., Steinmetz, T., Dubois, G., Linke, F., Hunger, D., and Reichel, J. Strong atom-field coupling for bose-einstein condensates in an optical cavity on a chip. *Nature*, **450**(7167):272–276, Nov 2007. <http://dx.doi.org/10.1038/nature06331>. (Cited on 4)
- [32] Guthohrlein, G. R., Keller, M., Hayasaka, K., Lange, W., and Walther, H. A single ion as a nanoscopic probe of an optical field. *Nature*, **414**:49–51, Nov 2001. <http://dx.doi.org/10.1038/35102129>. (Cited on 4)
- [33] Mundt, A. B., Kreuter, A., Becher, C., Leibfried, D., Eschner, J., Schmidt-Kaler, F., and Blatt, R. Coupling a single atomic quantum bit to a high finesse optical cavity. *Phys. Rev. Lett.*, **89**:103001, Aug 2002. <https://link.aps.org/doi/10.1103/PhysRevLett.89.103001>.
- [34] Leibrandt, D. R., Labaziewicz, J., Vuletić, V., and Chuang, I. L. Cavity sideband cooling of a single trapped ion. *Phys. Rev. Lett.*, **103**:103001, Aug 2009. <https://link.aps.org/doi/10.1103/PhysRevLett.103.103001>.
- [35] Herskind, P. F., Dantan, A., Marler, J. P., Albert, M., and Drewsen, M. Realization

- of collective strong coupling with ion coulomb crystals in an optical cavity. *Nature Physics*, **5**:494–498, Jul 2009. <http://dx.doi.org/10.1038/nphys1302>.
- [36] Sterk, J. D., Luo, L., Manning, T. A., Maunz, P., and Monroe, C. Photon collection from a trapped ion-cavity system. *Phys. Rev. A*, **85**:062308, Jun 2012. <http://link.aps.org/doi/10.1103/PhysRevA.85.062308>.
- [37] Stute, A., Casabone, B., Schindler, P., Monz, T., Schmidt, P. O., Brandstatter, B., Northup, T. E., and Blatt, R. Tunable ion-photon entanglement in an optical cavity. *Nature*, **485**(7399):482–485, May 2012. ISSN 0028-0836. <http://dx.doi.org/10.1038/nature11120>.
- [38] Steiner, M., Meyer, H. M., Deutsch, C., Reichel, J., and Köhl, M. Single ion coupled to an optical fiber cavity. *Phys. Rev. Lett.*, **110**:043003, Jan 2013. <http://link.aps.org/doi/10.1103/PhysRevLett.110.043003>. (Cited on 4, 20, 94)
- [39] Ballance, T. G., Meyer, H. M., Kobel, P., Ott, K., Reichel, J., and Köhl, M. Cavity-induced backaction in Purcell-enhanced photon emission of a single ion in an ultraviolet fiber cavity. *Phys. Rev. A*, **95**:033812, Mar 2017. <https://link.aps.org/doi/10.1103/PhysRevA.95.033812>. (Cited on 4, 93, 94)
- [40] Harlander, M., Brownnutt, M., Hänsel, W., and Blatt, R. Trapped-ion probing of light-induced charging effects on dielectrics. *New Journal of Physics*, **12**(9):093035, 2010. <http://stacks.iop.org/1367-2630/12/i=9/a=093035>. (Cited on 4, 20)
- [41] Takahashi, H., Wilson, A., Riley-Watson, A., Orucević, F., Seymour-Smith, N., Keller, M., and Lange, W. An integrated fiber trap for single-ion photonics. *New Journal of Physics*, **15**(5):053011, 2013. <http://stacks.iop.org/1367-2630/15/i=5/a=053011>. (Cited on 4, 20, 32)
- [42] Benhelm, J., Kirchmair, G., Roos, C. F., and Blatt, R. Towards fault-tolerant quantum computing with trapped ions. *Nat. Phys.*, **4**:463–466, Apr 2008. <http://dx.doi.org/10.1038/nphys961>. (Cited on 5)
- [43] Raussendorf, R. and Harrington, J. Fault-tolerant quantum computation with high threshold in two dimensions. *Phys. Rev. Lett.*, **98**:190504, May 2007. <http://link.aps.org/doi/10.1103/PhysRevLett.98.190504>. (Cited on 5)
- [44] Casabone, B., Stute, A., Friebel, K., Brandstätter, B., Schüppert, K., Blatt, R., and Northup, T. E. Heralded entanglement of two ions in an optical cavity. *Phys. Rev.*

- Lett.*, **111**:100505, Sep 2013. <http://link.aps.org/doi/10.1103/PhysRevLett.111.100505>. (Cited on 5)
- [45] Begley, S., Vogt, M., Gulati, G. K., Takahashi, H., and Keller, M. Optimized multi-ion cavity coupling. *Phys. Rev. Lett.*, **116**:223001, May 2016. <http://link.aps.org/doi/10.1103/PhysRevLett.116.223001>. (Cited on 5)
- [46] Matsubara, K., Hachisu, H., Li, Y., Nagano, S., Locke, C., Nogami, A., Kajita, M., Hayasaka, K., Ido, T., and Hosokawa, M. Direct comparison of a Ca<sup>+</sup> single-ion clock against a Sr lattice clock to verify the absolute frequency measurement. *Opt. Express*, **20**(20):22034–22041, Sep 2012. <http://www.opticsexpress.org/abstract.cfm?URI=oe-20-20-22034>. (Cited on 6)
- [47] Leibfried, D., Roos, C., Barton, P., Rohde, H., Guide, S., Mundt, A. B., Schmidt-Kaler, F., Eschner, J., and Blatt, R. *Quantum Communication, Computing, and Measurement 3: Towards Quantum Computation with Trapped Calcium Ions*. Springer, New York City, NY, United States of America, 2002. ISBN 978-0-306-47114-8. [http://dx.doi.org/10.1007/0-306-47114-0\\_29](http://dx.doi.org/10.1007/0-306-47114-0_29). (Cited on 6)
- [48] Sheridan, K. *Experimental techniques for cold chemistry and molecular spectroscopy in an ion trap*. PhD thesis, University of Sussex, 2012. (Cited on 6)
- [49] Pierre, M. and Sargent III, M. *Elements of Quantum Optics*. Springer, third edition, New York City, NY, United States of America, 1999. ISBN 3-540-64220-X. (Cited on 7)
- [50] Russo, C. *Photon statistics of a single ion coupled to a high-finesse cavity*. PhD thesis, University of Innsbruck, 2008. (Cited on 7, 11)
- [51] Pierre, M. and Sargent III, M. *Elements of Quantum Optics, Ch. 14*. Springer, third edition, New York City, NY, United States of America, 1999. ISBN 3-540-64220-X. (Cited on 7)
- [52] Pierre, M. and Sargent III, M. *Elements of Quantum Optics, Ch. 18*. Springer, third edition, New York City, NY, United States of America, 1999. ISBN 3-540-64220-X. (Cited on 9)
- [53] Purcell, E. M. Spontaneous emission probabilities at radio frequencies. *Physical Review*, **69**:681+, 1946. [http://prola.aps.org/pdf/PR/v69/i11-12/p674\\_2](http://prola.aps.org/pdf/PR/v69/i11-12/p674_2). (Cited on 12)

- [54] Pierre, M. and Sargent III, M. *Elements of Quantum Optics, Ch. 3*. Springer, third edition, New York City, NY, United States of America, 1999. ISBN 3-540-64220-X. (Cited on 12)
- [55] Kuhn, A. and Ljunggren, D. Cavity-based single-photon sources. *Contemporary Physics*, **51**(4):289–313, 2010. <http://dx.doi.org/10.1080/00107511003602990>. (Cited on 14)
- [56] Tan, S. M. A computational toolbox for quantum and atomic optics. *Journal of Optics B: Quantum and Semiclassical Optics*, **1**(4):424, 1999. <http://stacks.iop.org/1464-4266/1/i=4/a=312>. (Cited on 17)
- [57] VanDevender, A. P., Colombe, Y., Amini, J., Leibfried, D., and Wineland, D. J. Efficient fiber optic detection of trapped ion fluorescence. *Phys. Rev. Lett.*, **105**: 023001, Jul 2010. <http://link.aps.org/doi/10.1103/PhysRevLett.105.023001>. (Cited on 20)
- [58] Herskind, P. F., Wang, S. X., Shi, M., Ge, Y., Cetina, M., and Chuang, I. L. Microfabricated surface ion trap on a high-finesse optical mirror. *Opt. Lett.*, **36**(16): 3045–3047, Aug 2011. <http://ol.osa.org/abstract.cfm?URI=ol-36-16-3045>.
- [59] Tony Hyun Kim, P. F. H. and Chuang, I. L. Surface-electrode ion trap with integrated light source. *Appl. Phys. Lett.*, **98**:214103, 2011. <http://dx.doi.org/10.1063/1.3593496>. (Cited on 20)
- [60] Earnshaw, S. On the nature of molecular forces which regulate the constitution of the luminiferous ether. *Trans. Camb. Phil. Soc.*, **7**(1):97–112, 1839. <http://www.mit.edu/~kardar/research/seminars/Casimir2010/pdf/EarnshawPaper.pdf>. (Cited on 28)
- [61] Leibfried, D., Blatt, R., Monroe, C., and Wineland, D. Quantum dynamics of single trapped ions. *Rev. Mod. Phys.*, **75**:281–324, Mar 2003. <https://link.aps.org/doi/10.1103/RevModPhys.75.281>. (Cited on 31)
- [62] Sivers, J. D., Simkins, L. R., Weidt, S., and Hensinger, W. K. On the application of radio frequency voltages to ion traps via helical resonators. *Applied Physics B*, **107**(4): 921–934, 2012. ISSN 1432-0649. <http://dx.doi.org/10.1007/s00340-011-4837-0>. (Cited on 53)

- [63] Gulde, S., Rotter, D., Barton, P., Schmidt-Kaler, F., Blatt, R., and Hogervorst, W. Simple and efficient photo-ionization loading of ions for precision ion-trapping experiments. *Applied Physics B*, **73**(8):861–863, 2001. ISSN 1432-0649. <http://dx.doi.org/10.1007/s003400100749>. (Cited on 56, 97)
- [64] Lucas, D. M., Ramos, A., Home, J. P., McDonnell, M. J., Nakayama, S., Stacey, J.-P., Webster, S. C., Stacey, D. N., and Steane, A. M. Isotope-selective photoionization for calcium ion trapping. *Phys. Rev. A*, **69**:012711, Jan 2004. <http://link.aps.org/doi/10.1103/PhysRevA.69.012711>. (Cited on 56, 97)
- [65] Linke, N. M., Allcock, D. T. C., Szwer, D. J., Ballance, C. J., Harty, T. P., Janacek, H. A., Stacey, D. N., Steane, A. M., and Lucas, D. M. Background-free detection of trapped ions. *Applied Physics B*, **107**(4):1175–1180, 2012. ISSN 1432-0649. <http://dx.doi.org/10.1007/s00340-011-4870-z>. (Cited on 59)
- [66] Seymour-Smith, N., Blythe, P., Keller, M., and Lange, W. Fast scanning cavity offset lock for laser frequency drift stabilization. *Review of Scientific Instruments*, **81**(7):075109, 2010. <http://scitation.aip.org/content/aip/journal/rsi/81/7/10.1063/1.3455830>. (Cited on 59)
- [67] Seymour-Smith, N. *Ion-trap cavity QED system for probabilistic entanglement*. PhD thesis, University of Sussex, 2012. (Cited on 59)
- [68] Drever, R. W. P., Hall, J. L., Kowalski, F. V., Hough, J., Ford, G. M., Munley, A. J., and Ward, H. Laser phase and frequency stabilization using an optical resonator. *Applied Physics B*, **31**(2):97–105, 1983. ISSN 1432-0649. <http://dx.doi.org/10.1007/BF00702605>. (Cited on 61)
- [69] D. J. Berkeland J. D. Miller, J. C. Bergquist, W. M. Itano and D. J. Wineland. Minimization of ion micromotion in a Paul trap. *J. Appl. Phys.*, **83**:5025, 1998. <http://dx.doi.org/10.1063/1.367318>. (Cited on 67, 69)
- [70] Novikov, L. N., Skrotskii, G. V., and Solomakho, G. I. The Hanle effect. *Soviet Physics Uspekhi*, **17**(4):542, 1975. <http://stacks.iop.org/0038-5670/17/i=4/a=R05>. (Cited on 76)
- [71] Stute, A., Casabone, B., Brandstätter, B., Habicher, D., Barros, H. G., Schmidt, P. O., Northup, T. E., and Blatt, R. Toward an ion–photon quantum interface in an optical cavity. *Applied Physics B*, **107**(4):1145–1157, 2012. ISSN 1432-0649. <http://dx.doi.org/10.1007/s00340-011-4861-0>. (Cited on 87)

- [72] Brandstätter, B., McClung, A., Schüppert, K., Casabone, B., Fribe, K., Stute, A., Schmidt, P. O., Deutsch, C., Reichel, J., Blatt, R., and Northup, T. E. Integrated fiber-mirror ion trap for strong ion-cavity coupling. *Review of Scientific Instruments*, **84**(12):123104, 2013. <http://dx.doi.org/10.1063/1.4838696>. (Cited on 87)
- [73] Steiner, M., Meyer, H. M., Reichel, J., and Köhl, M. Photon emission and absorption of a single ion coupled to an optical-fiber cavity. *Phys. Rev. Lett.*, **113**:263003, Dec 2014. <https://link.aps.org/doi/10.1103/PhysRevLett.113.263003>. (Cited on 94)
- [74] Jin, J. and Church, D. A. Precision lifetimes for the  $\text{Ca}^+$   $4\text{p}^2\text{P}$  levels: Experiment challenges theory at the 1% level. *Phys. Rev. Lett.*, **70**:3213–3216, May 1993. <https://link.aps.org/doi/10.1103/PhysRevLett.70.3213>. (Cited on 98, 99)
- [75] Gosselin, R. N., Pinnington, E. H., and Ansbacher, W. Measurement of the lifetimes of the 4p levels in Ca II using laser excitation of a fast beam. *Phys. Rev. A*, **38**:4887–4890, Nov 1988. <https://link.aps.org/doi/10.1103/PhysRevA.38.4887>. (Cited on 98, 99)
- [76] Ramm, M., Pruttivarasin, T., Kokish, M., Talukdar, I., and Häffner, H. Precision measurement method for branching fractions of excited  $P_{1/2}$  states applied to  $^{40}\text{Ca}^+$ . *Phys. Rev. Lett.*, **111**:023004, Jul 2013. <https://link.aps.org/doi/10.1103/PhysRevLett.111.023004>. (Cited on 99)
- [77] Gerritsma, R., Kirchmair, G., Zähringer, F., Benhelm, J., Blatt, R., and Roos, C. F. Precision measurement of the branching fractions of the  $4\text{p}^2P_{3/2}$  decay of Ca. *The European Physical Journal D*, **50**(1):13–19, 2008. ISSN 1434-6079. <http://dx.doi.org/10.1140/epjd/e2008-00196-9>. (Cited on 99)
- [78] James, D. Quantum dynamics of cold trapped ions with application to quantum computation. *Applied Physics B*, **66**(2):181–190, 1998. ISSN 1432-0649. <http://dx.doi.org/10.1007/s003400050373>. (Cited on 99)
- [79] Wiese, S. I., Smith, M. W., and Miles, B. M. Atomic transition probabilities. *Institute for Basic Standards, National Bureau of Standards, Washington D.C.*, **2**:251–255, Oct 1969. <http://www.dtic.mil/dtic/tr/fulltext/u2/696884.pdf>. (Cited on 99)
- [80] Gallagher, A. Oscillator strengths of Ca II, Sr II, and Ba II. *Phys. Rev.*, **157**:24–30, May 1967. <https://link.aps.org/doi/10.1103/PhysRev.157.24>. (Cited on 99)

- [81] Barton, P. A., Donald, C. J. S., Lucas, D. M., Stevens, D. A., Steane, A. M., and Stacey, D. N. Measurement of the lifetime of the  $3d^2D_{5/2}$  state in  $^{40}\text{Ca}^+$ . *Phys. Rev. A*, **62**:032503, Aug 2000. <http://link.aps.org/doi/10.1103/PhysRevA.62.032503>. (Cited on 99)
- [82] Kreuter, A., Becher, C., Lancaster, G. P. T., Mundt, A. B., Russo, C., Häffner, H., Roos, C., Hänsel, W., Schmidt-Kaler, F., Blatt, R., and Safronova, M. S. Experimental and theoretical study of the  $3d\ ^2D$ -level lifetimes of  $^{40}\text{Ca}^+$ . *Phys. Rev. A*, **71**:032504, Mar 2005. <https://link.aps.org/doi/10.1103/PhysRevA.71.032504>. (Cited on 99)
- [83] Arscott, F. M. *Periodic differential equations: an introduction to Mathieu, Lamé and allied Functions*. Pergamon Press, Oxford, United Kingdom, 1964. (Cited on 100)
- [84] McLachlan, N. W. *Theory and Application of Mathieu Functions*. Clarendon, Oxford, United Kingdom, 1947. (Cited on 100)